5-2018

Multidimensional Nonlinear Optical Imaging

Fengyuan Deng
Purdue University

MULTIDIMENSIONAL NONLINEAR OPTICAL IMAGING

by

Fengyuan Deng

A Dissertation

Submitted to the Faculty of Purdue University

In Partial Fulfillment of the Requirements for the degree of

Doctor of Philosophy

Department of Chemistry

West Lafayette, Indiana

May 2018

THE PURDUE UNIVERSITY GRADUATE SCHOOL
STATEMENT OF COMMITTEE APPROVAL

Dr. Garth J. Simpson, Chair
Department of Chemistry
Dr. Chengde Mao
Department of Chemistry
Dr. Adam Wasserman
Department of Chemistry
Dr. Chittaranjan Das
Department of Chemistry

Approved by:

Dr. Christine Hrycyna
Head of the Graduate Program

To my parents, for always loving and supporting me.

ACKNOWLEDGMENTS

I would like to thank my parents for their unconditional love and support throughout my life. It is not possible for me to accomplish this work without your helps. I would also like to say special thanks to my girlfriend Xusi Han. You take great care of me since I joined Purdue. A special thanks to Dr. Garth Simpson, you are truly an amazing mentor and scientist.

I would also like to thank all the group members in Simpson lab, especially to Ryan Muir, Shane Sullivan, Justin Newman and Ximeng Dow. You taught me the basics of nonlinear optics and electronics; to Changqin Ding, for working closely with me on most of the research projects and being one of my best friends; to James Ulcickas, for discussing science, food and other random stuffs with me in office and during conferences.

Last but not least, thanks to all my friends at Purdue, Shijie Zhang, Zhengtian Song, Chen Li, Youlin Liu, Yiyang Zhou, Longfei Liu, Aaron Chen, Yun Yang and many others for the helps and encouragements throughout this journey. It’s a remarkable 4 years.

TABLE OF CONTENTS

LIST OF TABLES

LIST OF FIGURES

LIST OF ABBREVIATIONS

1PF	one-photon fluorescence
CARS	coherent anti-stokes Raman scattering
CASSI	coded aperture snapshot spectral imager
CD	circular dichroism
DSC	differential scanning calorimetry
ECD	electronic CD
F-ORD	fluorescence optical rotary dispersion
FoV	field of view
IMS	image mapping spectrometer
NDSSM	non-de-scan spatial/spectral multiplexing
NIR	near IR
NLO	nonlinear optics
PCB	printed circuit board
PD-SHG	polarization dependent SHG
PMT	photo multiplier tube
ppm	parts per million
PXRD	powder X-ray diffraction
ROA	Raman optical activity
RTV	ritonavir
SEM	scanning electron microscopy
SEROA	surface enhanced Raman optical activity
SHG	second harmonic generation
SNR	signal to noise ratio
SRS	stimulated Raman scattering
VCD	vibrational CD

ABSTRACT

Author: Deng, Fengyuan. PhD
Institution: Purdue University
Degree Received: May 2018
Title: Multidimensional Nonlinear Optical Imaging
Committee Chair: Garth Simpson

The work in this dissertation is focused on extending the information content for second harmonic generation (SHG) and two-photon excited fluorescence (TPEF) imaging. Despite the simplicity and symmetry selectivity of nonlinear optical processes, limited information on chemical composition can be recovered solely based on intensity measurements. To further explore the potential for second order nonlinear optical (NLO) measurements, additional dimensions were added to the NLO imaging platforms. By combining NLO microscopy with powder X-ray diffraction, a novel approach was established for accessing percent crystallinity in amorphous solid dispersions (ASDs) with a limit of detection in the ppm range. ASDs are preferable alternative for crystalline forms when formulating poorly soluble active pharmaceutical ingredients (APIs). However, the high detection limit for current available methods limited the study of long term stability for ASDs at early stage. Besides adding additional modalities to NLO microscopy, polarization dependent SHG provides rich information on local structures for collagen fibers in tissues. However, significant loss in polarization purities occurs when light penetrate through the tissue. A new theoretical framework was introduced to extract information with partially or fully depolarized light. In addition, a video-rate hyperspectral TPEF imaging system was demonstrated with over 2,200 fluorescence channels throughput spatial-spectral multiplexing.

CHAPTER 1. INTRODUCTION

1.1 Overview for Second Order Nonlinear Optical Imaging

Nonlinear optics (NLO) describes the optical behaviors where the polarization responds nonlinearly to the electric field. The first nonlinear optical effect was discovered by Peter Franken *et al.* at University of Michigan in 1961 shortly after the invention of the laser.[1] Franken and co-workers focused millisecond pulsed ruby laser at 694.3 nm onto crystalline quartz and observed its optical harmonics at 347.2 nm. This phenomenon was later known as second harmonic generation (SHG).

SHG is classically originated from the interaction between the photon induced electric field and anharmonic potential energy surface of electrons.[2] When driven by a strong electric field at frequency ω, the induced distorted electric field from the anharmonic potential curve is dominated by three Fourier components: a sinusoidal component oscillated at ω, a sinusoidal component at 2ω (SHG) and a DC component (optical rectification). Although the anharmonic oscillation could happen in both centrosymmetric and noncentrosymmetric media, coherent SHG can only be observed in noncentrosymmetric medium. The presence of an inversion center means that for any given anharmonic potential surface, there is a corresponding potential surface with opposite direction. The induced 2ω components are π out of phase. If they are positioned at distances that much less than the wavelength of the light, they will interfere destructively. Therefore, SHG is highly selective for highly ordered noncentrosymmetric media. The presence of SHG from crystalline amino acids was first observed in 1965[3] and biological tissues in 1971.[4] In 1979, first systematic study of SHG in collagen was published by Roth and Freund.[5] Recently, beam-scanning SHG microscopy has been widely used for characterizing highly ordered noncentrosymmetric structures such as collagen[6-9], protein crystals[10-14], crystalline active pharmaceutical ingredients (API).[15-20]

In two-photon excited fluorescence (TPEF) process, fluorescence photons are generated through relaxation of molecules into their ground state. The excitation process for the TPEF is achieved by second order NLO process known as two-photon absorption (TPA). TPEF was first predicted by Maria Goeppert-Mayer in her doctoral dissertation[21] in 1931 and observed experimentally in 1961[22], when Kaiser and Garrett detected the blue shifted fluorescence signal at

around 420.5 nm with an excitation wavelength of 694.3 nm. The first beam-scanning TPEF microscope was demonstrated by Denk, *et al.* in 1990[23]. It has been widely used for deep in tissue biological imaging since then. [24-26]

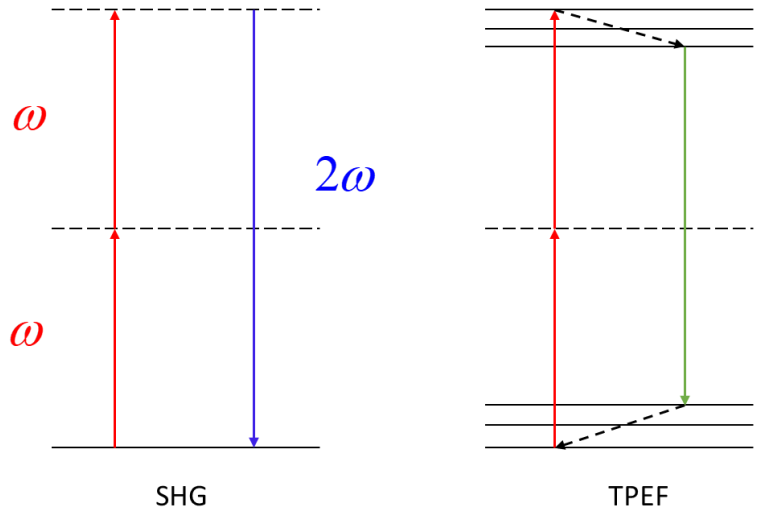

Figure 1-1 Jablonski diagram for second harmonic generation (SHG) and two-photon excited fluorescence (TPEF).

1.2 Extending Information Contents for NLO Microscopy

Compared to traditional linear optical approaches, second order nonlinear optical microscopy provides several unique advantages: i) the symmetry requirement for second order NLO process make (SHG) highly selective to certain structures such as collagen and non-centrosymmetric crystals; ii) the quadratic dependence of the incident light provides better localization ability in z-direction; iii) the use of near IR (NIR) excitation greatly increase the depth of penetrations for deep tissue imaging; and iv) the optical beam path and electronics design are relatively simple compared to higher order NLO imaging such as coherent anti-stokes Raman scattering (CARS) and stimulated Raman scattering (SRS). Despite these unique advantages of SHG and TPEF imaging, little chemical information can be obtained based on intensity contrast from SHG or TPEF along. Orthogonal methods such as IR, Raman and X-ray diffraction could in principle provide complementary information for SHG and TPEF. However, the measurement speeds are typically limited by the integration time required for these measurements, which limits the potential for high

throughput quality control and *in vivo* imaging. Also, significant uncertainties can be introduced during the sample transfer between these measurements. The works described in this dissertation focus on new instrumentation and method development for extending the information content with existing second order NLO imaging platform while maintaining the measurement throughput. In general, two strategies are implemented: i) the integration of on-axis orthogonal imaging contrast with NLO microscope. The NLO contrast is used as a fast selection tool for regions of interest and orthogonal imaging modalities are only measured for a small fraction of the entire probe volume; ii) adding additional dimensions to existing NLO system such as polarization modulation and spectral dispersion.

1.3 Dissertation Overview

The works described in this dissertation focus on new instrumentation and method development for extending the information content with existing second order NLO imaging platform while maintaining the measurement throughput. In general, two strategies are implemented: i) the integration of on-axis orthogonal imaging contrast with NLO microscope. The NLO contrast is used as a fast selection tool for regions of interest and orthogonal imaging modalities are only measured for a small fraction of the entire probe volume; ii) adding additional dimensions to existing NLO system such as polarization modulation and spectral dispersion.

In chapter 2, an integrated SHG-guided powder X-ray diffraction (PXRD) study was demonstrated for high throughput crystallinity screening for amorphous solid dispersion. The detection limit for the PXRD is improved by an order of magnitude by precise guidance with the SHG microscopy measurement. Chapter 3 introduces a theoretical foundation for electric-dipole allowed chiral specific fluorescence measurements for uniaxial assemblies. The proposed mechanism provided a good explanation for experimental observations[27-28]. Chapter 4 builds a theoretical framework to analyze the polarization dependent SHG from partially or fully depolarized fundamental raised from tissue induced scattering. Hyperpolarizability tensors are successfully recovered for z-cut quartz and collagenous tissue with fully depolarized fundamental. This provides a novel strategy to do polarization dependent SHG for deep tissue imaing. In chapter 5, a new strategy was implemented to achieve polarization modulation with a low-cost patterned microretarder array. This approach provides polarization dependent SHG capability with comparable frame rates with electric optical modulator at a fraction of the cost. Chapter 6

introduces a spatial-spectral multiplexing hyperspectral TPEF imaging system with a 16-channel photo multiplier tube (PMT) array. Data throughput is reduced by over 100-fold via multiplexing. Hyperspectral images of fluorescent dye droplets and live *C. elegans* were acquired at video-rate with over 2,000 fluorescence channels.

1.4 Reference

1. Franken, e. P.; Hill, A. E.; Peters, C. e.; Weinreich, G., Generation of optical harmonics. *Physical Review Letters* **1961,** *7* (4), 118.

2. Simpson, G. J., *Nonlinear Optical Polarization Analysis in Chemistry and Biology*. Camgridge Molecular Science: 2017.

3. Rieckhoff, K. E.; Peticolas, W. L., Optical second-harmonic generation in crystalline amino acids. *Science* **1965,** *147* (3658), 610-611.

4. Fine, S.; Hansen, W., Optical second harmonic generation in biological systems. *Applied optics* **1971,** *10* (10), 2350-2353.

5. Roth, S.; Freund, I., Second harmonic generation in collagen. *The Journal of chemical physics* **1979,** *70* (4), 1637-1643.

6. Guo, Y.; Ho, P.; Savage, H.; Harris, D.; Sacks, P.; Schantz, S.; Liu, F.; Zhadin, N.; Alfano, R., Second-harmonic tomography of tissues. *Optics Letters* **1997,** *22* (17), 1323-1325.

7. Williams, R. M.; Zipfel, W. R.; Webb, W. W., Interpreting second-harmonic generation images of collagen I fibrils. *Biophysical journal* **2005,** *88* (2), 1377-1386.

8. Dow, X. Y.; DeWalt, E. L.; Sullivan, S. Z.; Schmitt, P. D.; Ulcickas, J. R. W.; Simpson, G. J., Imaging the Nonlinear Susceptibility Tensor of Collagen by Nonlinear Optical Stokes Ellipsometry. *Biophys J* **2016,** *111* (7), 1361-1374.

9. Ding, C.; Ulcickas, J. R.; Deng, F.; Simpson, G. J., Second Harmonic Generation of Unpolarized Light. *Physical review letters* **2017,** *119* (19), 193901.

10. Gualtieri, E.; Guo, F.; Kissick, D.; Jose, J.; Kuhn, R.; Jiang, W.; Simpson, G., Detection of membrane protein two-dimensional crystals in living cells. *Biophysical journal* **2011,** *100* (1), 207-214.

11. Kissick, D. J.; Wanapun, D.; Simpson, G. J., Second-order nonlinear optical imaging of chiral crystals. *Annual Review of Analytical Chemistry* **2011,** *4*, 419-437.

12. DeWalt, E. L.; Begue, V. J.; Ronau, J. A.; Sullivan, S. Z.; Das, C.; Simpson, G. J., Polarization-resolved second-harmonic generation microscopy as a method to visualize protein-crystal domains. *Acta Crystallographica Section D: Biological Crystallography* **2013,** *69* (1), 74-81.

13. DeWalt, E. L.; Sullivan, S. Z.; Schmitt, P. D.; Muir, R. D.; Simpson, G. J., Polarization-modulated second harmonic generation ellipsometric microscopy at video rate. *Anal Chem* **2014,** *86* (16), 8448-56.

14. Newman, J. A.; Zhang, S.; Sullivan, S. Z.; Dow, X. Y.; Becker, M.; Sheedlo, M. J.; Stepanov, S.; Carlsen, M. S.; Everly, R. M.; Das, C., Guiding synchrotron X-ray diffraction by multimodal video-rate protein crystal imaging. *Journal of synchrotron radiation* **2016,** *23* (4), 959-965.

15. Kestur, U. S.; Wanapun, D.; Toth, S. J.; Wegiel, L. A.; Simpson, G. J.; Taylor, L. S., Nonlinear optical imaging for sensitive detection of crystals in bulk amorphous powders. *Journal of pharmaceutical sciences* **2012,** *101* (11), 4201-4213.

16. Wanapun, D.; Kestur, U.; Taylor, L.; Simpson, G., Single particle nonlinear optical imaging of trace crystallinity in an organic powder. *Analytical chemistry* **2011,** *83* (12), 4745-4751.

17. Wanapun, D.; Kestur, U. S.; Kissick, D. J.; Simpson, G. J.; Taylor, L. S., Selective detection and quantitation of organic molecule crystallization by second harmonic generation microscopy. *Analytical chemistry* **2010,** *82* (13), 5425-5432.

18. Zhu, Q.; Toth, S. J.; Simpson, G. J.; Hsu, H.-Y.; Taylor, L. S.; Harris, M. T., Crystallization and dissolution behavior of naproxen/polyethylene glycol solid dispersions. *The Journal of Physical Chemistry B* **2013,** *117* (5), 1494-1500.

19. Toth, S.; Madden, J.; Taylor, L.; Marsac, P.; Simpson, G., Selective imaging of active pharmaceutical ingredients in powdered blends with common excipients utilizing two-photon excited ultraviolet-fluorescence and ultraviolet-second order nonlinear optical imaging of chiral crystals. *Analytical chemistry* **2012,** *84* (14), 5869-5875.

20. Newman, J. A.; Schmitt, P. D.; Toth, S. J.; Deng, F.; Zhang, S.; Simpson, G. J., Parts per million powder X-ray diffraction. *Analytical chemistry* **2015,** *87* (21), 10950-10955.

21. Göppert-Mayer, M., Über elementarakte mit zwei quantensprüngen. *Annalen der Physik* **1931,** *401* (3), 273-294.

22. Kaiser, W.; Garrett, C. G. B., Two-Photon Excitation in $CaF_2:Eu^{2+}$. *Physical Review Letters* **1961,** *7* (6), 229-231.

23. Denk, W.; Strickler, J. H.; Webb, W. W., Two-photon laser scanning fluorescence microscopy. *Science* **1990,** *248* (4951), 73-76.

24. Helmchen, F.; Denk, W., Deep tissue two-photon microscopy. *Nat Methods* **2005,** *2* (12), 932-40.

25. Larson, D. R.; Zipfel, W. R.; Williams, R. M.; Clark, S. W.; Bruchez, M. P.; Wise, F. W.; Webb, W. W., Water-soluble quantum dots for multiphoton fluorescence imaging in vivo. *Science* **2003,** *300* (5624), 1434-1436.

26. Svoboda, K.; Yasuda, R., Principles of two-photon excitation microscopy and its applications to neuroscience. *Neuron* **2006,** *50* (6), 823-839.

27. Hassey, R.; Swain, E. J.; Hammer, N. I.; Venkataraman, D.; Barnes, M. D., Probing the chiroptical response of a single molecule. *Science* **2006,** *314* (5804), 1437-1439.

28. Tang, Y. Q.; Cook, T. A.; Cohen, A. E., Limits on Fluorescence Detected Circular Dichroism of Single Helicene Molecules. *Journal of Physical Chemistry A* **2009,** *113* (22), 6213-6216.

CHAPTER 2. PARTS PER MILLION POWDER X-RAY DIFFRACTION

2.1 Introduction

As the chemical complexity of the drug molecule increases, more and more drug candidates suffer from poor bioavailability problem. According to recent reports[1-2], 80% of the potential active pharmaceutical ingredients (APIs) are in danger of being abandoned due to their poor systemic exposures. In order to improve the bioavailability, amorphous form is often used to formulate poorly soluble APIs as it has relatively higher free energy compared to crystallin forms.[1, 3-5] Therefore, they have a faster dissolution rate. Depending on the chemical composition, certain amorphous forms have the tendency to spontaneously crystalize overtime. Several strategies have been used to improve the long-term stability of amorphous APIs during drug formulation processes. Polymeric crystallization inhibitors were commonly used to form amorphous solid dispersions (ASD).[4, 6-7] However, it remains challenging to characterize the percent crystallinity in drug formulations.

To access the percent crystallinity from drug formulation, powder X-ray diffraction (PXRD)[7-8], differential scanning calorimetry (DSC)[7], scanning electron microscopy (SEM)[8-10] and Raman spectroscopy[8-12] are typically used. Among these methods, PXRD has the lowest limit of detection at around 0.2 %.[13] This make it challenging to access the percent crystalline for drug formulations with low drug loadings. For example, for a formulation with ~1 % drug loading, crystalline APIs cannot be detected until 20 % of the APIs have crystalized. At the meantime, the integration time required for a single X-ray diffraction or Raman spectroscopy is on the scale of seconds to minutes. In practice, it is also hard to obtain spatial distributions of the crystals with PXRD.

SHG microscopy has several unique advantages for detecting trace crystallinity from ASD and other drug formulations: i) SHG measurement is highly selective to noncentrosymmetric crystals and no background signal will be generated from amorphous materials. ii) SHG microscopy provides spatial distribution of the crystals. iii) Combining the synchronously digitization technique,[14] SHG images can be acquired at video rate. Previous studies have demonstrated the detection of trace crystallinity in ASD at parts per million (ppm) level.[15-19] The fast measurement speed and low limit of detection make SHG microscopy suitable for high-throughput accelerated

stability test for amorphous formulations and kinetic study and modeling the crystallization process.[20]

Despite the selectivity of crystalline materials for SHG, it provides little information on chemical composition. This makes SHG microscopy difficult to determine the crystalline of certain drug formulations that contain other SHG active ingredients. To further expand the capability of trace crystallinity detection for SHG measurements and increase the throughput of ASD stability tests, we combined the SHG microscopy with orthogonal imaging modalities such as Raman spectroscopy[21] and X-ray diffraction[22]. The highly selective SHG measurements rapidly locate the small crystals in a large field of view (FoV) and the X-ray/Raman can be precisely aimed at the point of interests. This method not only provides chemical information of the crystals, significant signal to noise ratio (SNR) improvement and lower limit of detection in the was observed for both Raman and X-ray measurement. In this chapter, a XRD study of detection of trace crystallinity from ASD formulation of ritonavir (RTV) was demonstrated at ppm level with SHG-guided PXRD technique.

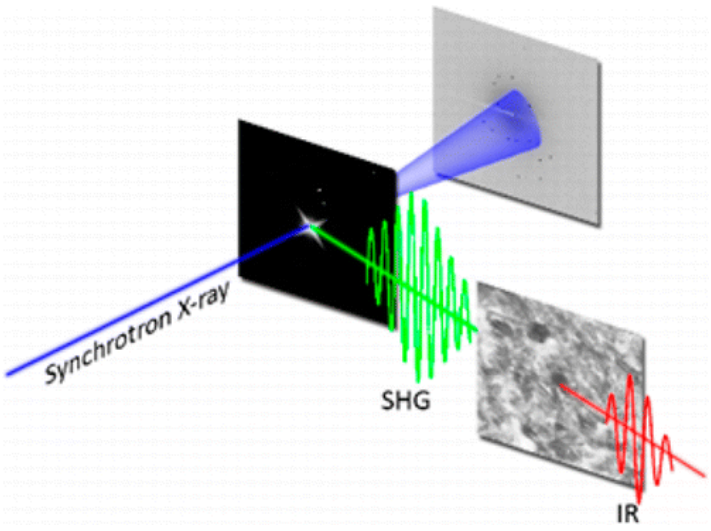

Figure 2-1 Overview of the SHG-guided PXRD

2.2 Methods

The integrated SHG-guided PXRD system was built at GM/CA@APS beamline 23-ID-B at Advanced Photon Source, Argonne National Laboratory and described in detailed in a previous publication.[23] In brief, a 50 MHz femtosecond laser at 1060nm (Fianium, FemtoPower 1060) was scanned across the FoV with a pair of resonant and galvanometer mirrors (Cambridge Technology). A 10× 0.35 NA objective (Optem) was used to focus the beam onto the image plane. The SHG signal was separated by a series of dichroic mirrors (Semrock F555-Di-03, Chroma z1064rdc-sp) and filters (Chroma HQ530/30, and CVI, 03FCT567/KG3) and redirect onto photon multiplier tube (PMT, Hamamatsu, H10722-10). The voltage transient was digitized synchronously with PCI-E based digital oscilloscope card (AlazarTech) and remapped into image with custom software (MATLAB).

The two-dimensional (2D) PXRD powder was fed into software package *Fable* and *Grainspotter*.[24] The locations of the diffraction peaks were first identified with a single intensity threshold and stacked into a three-dimensional (3D; x, y, tilt angles) g-vector file. Theoretical diffraction patterns based on the reported RTV crystal structure among the different crystal orientations were generated by *Grainspotter* and a lookup table was built for indexing. Next, *Grainspotter* automatically indexed the sets of diffraction peaks that matched to specific grains and fitted their corresponding orientations and locations. Once the position and orientation of the grain was determined, theoretical diffraction pattern was generated by *PolyXSim* and compared with the original 2D input. In addition to the 2D diffraction patterns, 1D diffraction pattern was converted from 2D pattern via azimuthal autocorrelation. Details about the 1D pattern conversion can be found in previous publication.[25]

The simulated drug formulation was prepared via serial dilutions of RTV (Astrix Laboratories, India) and hydroxypropyl methylcellulose (HPMC; Shin Etsu, Japan). 100 ppm (w/w) sample was then sandwiched between two number 1 coverslips with a thickness of ~150 μm. The sample was then mounted onto goniometer at GM/CA@APS beamline 23-ID-B for SHG and X-ray measurements.

2.3 Results and Discussion

SHG images of 100 ppm RTV in HPMC was shown in Figure 2.2. The size distribution of the particles was analyzed by particle counting algorithm with a large set of independent measurements and a histogram was shown in the bottom plot in Figure 2.2. An overall crystallinity of 230 ppm (v/v) was calculated from the image analysis. The recovered crystallinity from SHG measurements differs from the expectation by a factor of 2. The increase in crystallinity could potentially be raised from the difference between the volume analysis and weight analysis. The packing density and absolute density for both RTV and HPMC could be sufficiently different to induce such an error. In addition, the total probed volume was on the order of μL, corresponding to ~100 pL of total crystalline material. Consider the exceedingly small probing volume, error within 130 ppm of the anticipated value is encouraging for future quantitative studies.

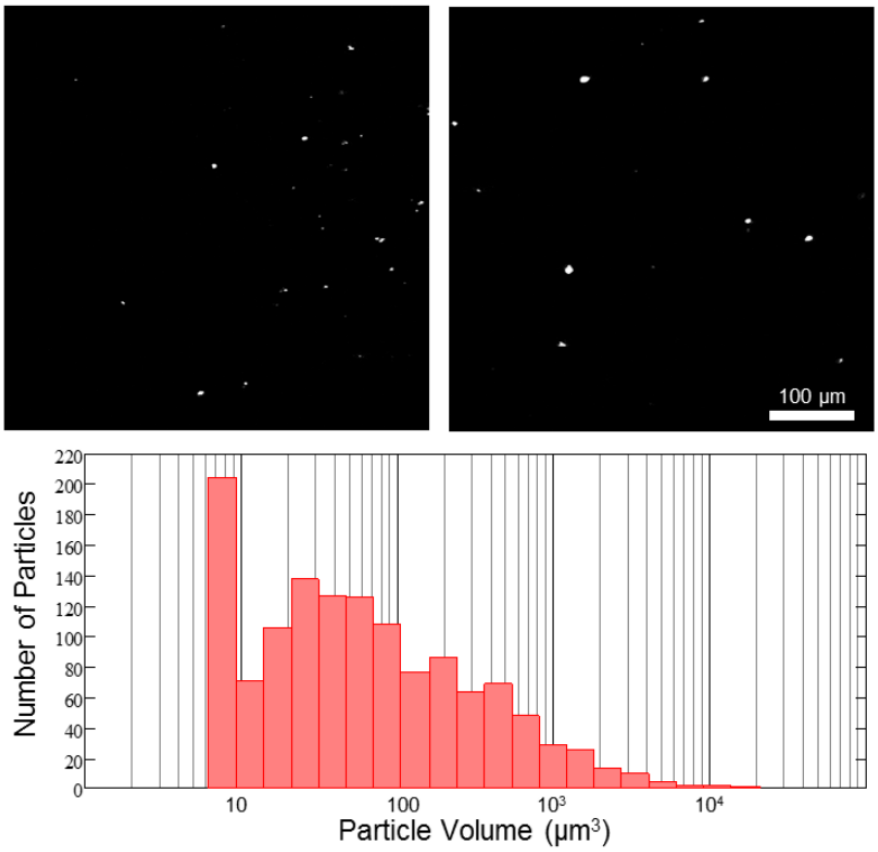

Figure 2-2 Selected SHG images of RTV in HPMC (top) and particle size distribution of the SHG active materials (bottom).

Unlike conventional PXRD study where the diffractions were generated from ensemble average of random orientated small crystals, SHG guided PXRD only probed a single or few crystals for a single measurement. Strong preferred orientation effect was observed. This makes indexing of the diffraction pattern extremely challenging for both single crystal XRD and PXRD software packages. To further demonstrated this effect, single crystal XRD measurement of RTV at 120 different crystal orientations was acquired. Two single XRD pattern at different angles was shown in Figures 2.3 A and B. Figure 2.3 C showed 2D pattern of the sum of all diffraction patterns at these 120 orientations (shown in blue). Despite the small subset of crystal orientations, the shape of the pattern begins to approach the predicted pattern for RTV (shown in red).

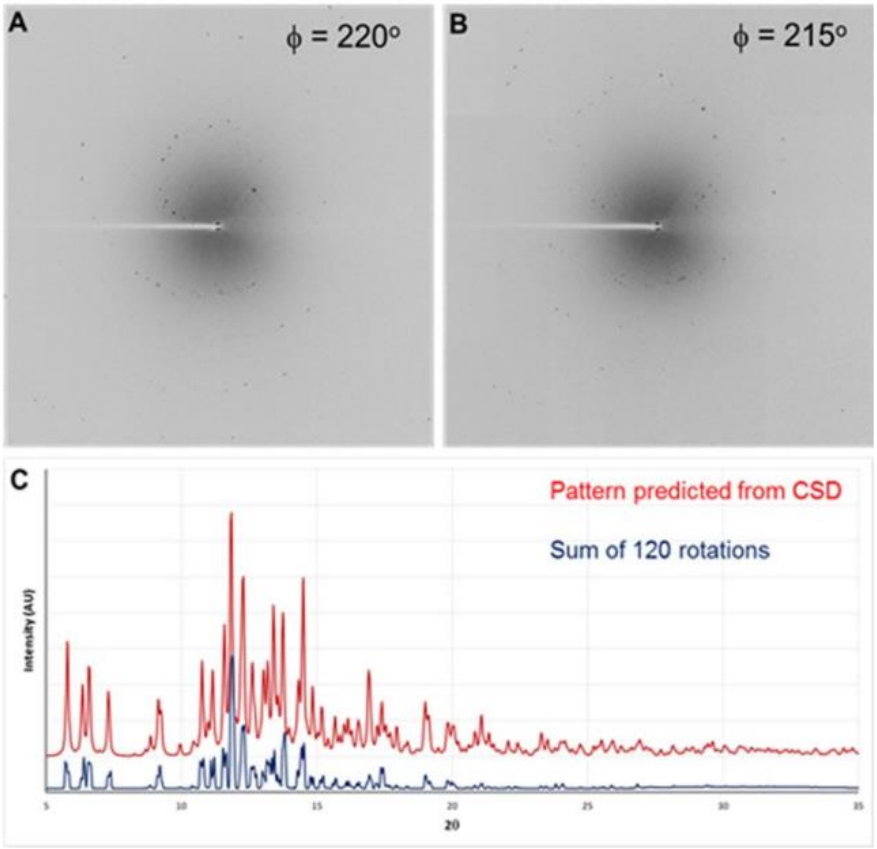

Figure 2-3 (A) and (B) Single crystal XRD of RTV at two different orientations. (C) Summation of 120 rotation angles compared with calculated pattern from CSD.

Fable and *Grainspotter* were originally designed for X-ray diffraction microscopy. Instead of solving the crystal lattice constants from the diffraction pattern (forward problem), *Grainspotter* uses known lattice constants of a crystal structure to determine the number of grains, orientations and positions that generates the input diffraction patterns (inverse problem). This makes the *Fable* and *Grainspotter* suitable for the SHG-guided PXRD measurement. Figure 2.4 A shows a single crystal XRD pattern of RTV at a random orientation. *Grainspotter* successfully indexed the diffraction peaks with lattice constants obtained from Cambridge structure database (YIGPIO03) shown in Figure 2.4 B with red spots.

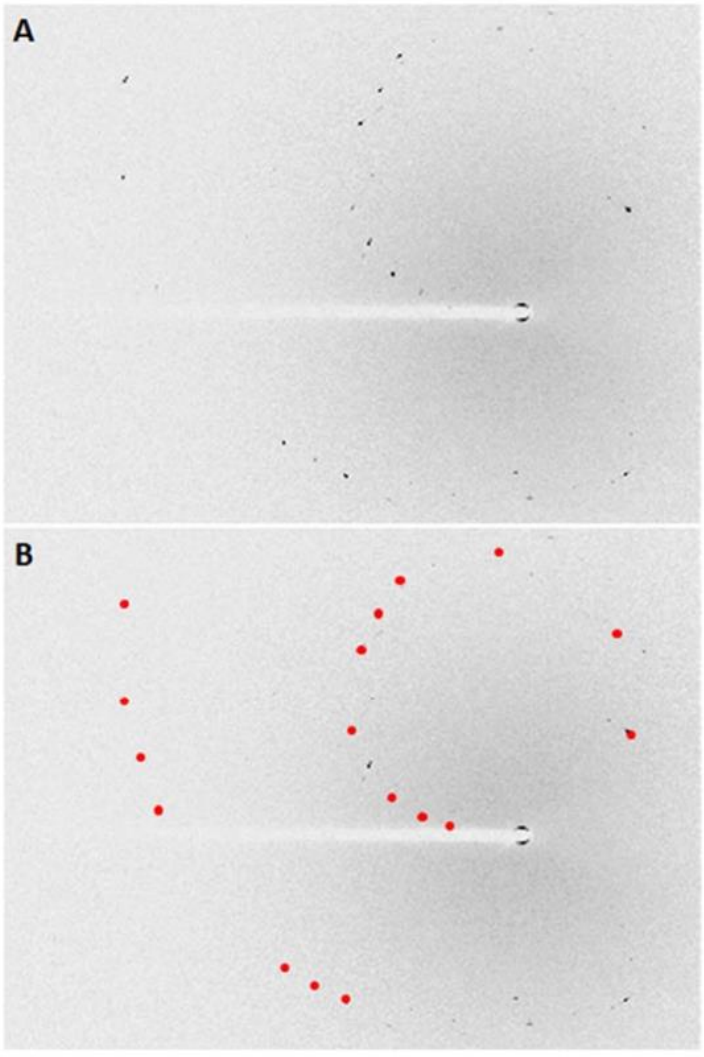

Figure 2-4 (A) A single frame from the crystal rotation series and (B) indexing result from *Grainspotter*.

To illustrate the reduction in limit of detection for SHG-guided PXRD measurements, the X-ray was aimed at an SHG active area (Figure 2.5 A) of the 100 ppm RTV/HPMC mixture and a single shot PXRD pattern was acquired (Figure 2.5 B) along with the indexable peaks with *Grainspotter* circled in red. Conventional PXRD spectrum of the 100 ppm RTV/HPMC is shown in Figure 2.5 C. *Grainspotter* is able to index multiple diffraction peaks with RTV's lattice constant where the conventional PXRD measurement is not indexable. The SNR of the pattern shown in Figure 2.5 C is over 5000 with a 1 s exposure and 5 μm beam. The minimum detection limit for a single crystal is on the order of 2 μm given the sixth power dependence of diffraction on crystal diameter.

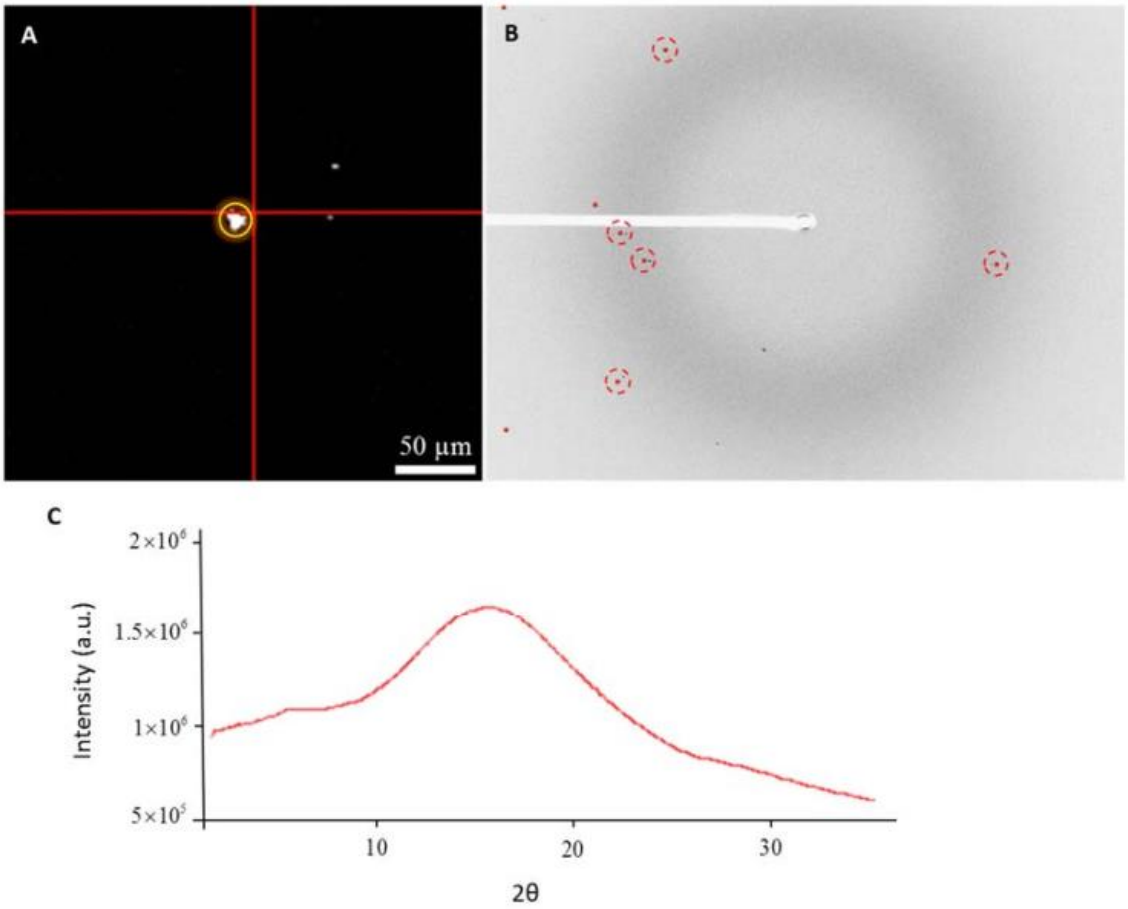

Figure 2-5 (A) A single frame from the crystal rotation series and (B) indexing result from *Grainspotter*.

2.4 Conclusion

The integration of SHG microscopy and PXRD provides unique complimentary information for both modalities. The indexing results from PXRD provides firm evidences on the identities of the crystalline materials and the SHG significant lowers the limit of detection for PXRD measurements. The SHG images can be acquired as fast as 15 frames per second, where the raster scanning of the X-ray for the entire field of view would be time consuming. The lower limit of detection allows the detection of crystalline at early stage. This system provides the potential for high throughput drug formulation analysis and kinetic modeling for crystallization.

2.5 Reference

1. Yu, L., Amorphous pharmaceutical solids: preparation, characterization and stabilization. *Advanced drug delivery reviews* **2001,** *48* (1), 27-42.

2. Liu, R., *Water-insoluble drug formulation*. CRC press: 2008.

3. Alonzo, D. E.; Gao, Y.; Zhou, D.; Mo, H.; Zhang, G. G.; Taylor, L. S., Dissolution and precipitation behavior of amorphous solid dispersions. *Journal of pharmaceutical sciences* **2011,** *100* (8), 3316-3331.

4. Serajuddin, A., Solid dispersion of poorly water-soluble drugs: Early promises, subsequent problems, and recent breakthroughs. *Journal of pharmaceutical sciences* **1999,** *88* (10), 1058-1066.

5. Van den Mooter, G., The use of amorphous solid dispersions: A formulation strategy to overcome poor solubility and dissolution rate. *Drug Discovery Today: Technologies* **2012,** *9* (2), e79-e85.

6. Simonelli, A.; Mehta, S.; Higuchi, W., Dissolution rates of high energy polyvinylpyrrolidone (PVP)-sulfathiazole coprecipitates. *Journal of pharmaceutical sciences* **1969,** *58* (5), 538-549.

7. Yoshioka, M.; Hancock, B. C.; Zografi, G., Inhibition of indomethacin crystallization in poly (vinylpyrrolidone) coprecipitates. *Journal of pharmaceutical sciences* **1995,** *84* (8), 983-986.

8. Newman, A. W.; Byrn, S. R., Solid-state analysis of the active pharmaceutical ingredient in drug products. *Drug discovery today* **2003,** *8* (19), 898-905.

9. Abu Bakar, M. R.; Nagy, Z. K.; Saleemi, A. N.; Rielly, C. D., The impact of direct nucleation control on crystal size distribution in pharmaceutical crystallization processes. *Crystal Growth and Design* **2009,** *9* (3), 1378-1384.

10. Miller, J. M.; Collman, B. M.; Greene, L. R.; Grant, D. J.; Blackburn, A. C., Identifying the stable polymorph early in the drug discovery–development process. *Pharmaceutical development and technology* **2005,** *10* (2), 291-297.

11. Taylor, L. S.; Zografi, G., The quantitative analysis of crystallinity using FT-Raman spectroscopy. *Pharmaceutical research* **1998,** *15* (5), 755-761.

12. Erdemir, D.; Lee, A. Y.; Myerson, A. S., Polymorph selection: the role of nucleation, crystal growth and molecular modeling. *Current opinion in drug discovery & development* **2007,** *10* (6), 746-755.

13. Nunes, C.; Mahendrasingam, A.; Suryanarayanan, R., Quantification of crystallinity in substantially amorphous materials by synchrotron X-ray powder diffractometry. *Pharmaceutical research* **2005,** *22* (11), 1942-1953.

14. Muir, R. D.; Sullivan, S. Z.; Oglesbee, R. A.; Simpson, G. J., Synchronous digitization for high dynamic range lock-in amplification in beam-scanning microscopy. *Rev Sci Instrum* **2014,** *85* (3), 033703.

15. Kestur, U. S.; Wanapun, D.; Toth, S. J.; Wegiel, L. A.; Simpson, G. J.; Taylor, L. S., Nonlinear optical imaging for sensitive detection of crystals in bulk amorphous powders. *Journal of pharmaceutical sciences* **2012,** *101* (11), 4201-4213.

16. Wanapun, D.; Kestur, U.; Taylor, L.; Simpson, G., Single particle nonlinear optical imaging of trace crystallinity in an organic powder. *Analytical chemistry* **2011,** *83* (12), 4745-4751.

17. Wanapun, D.; Kestur, U. S.; Kissick, D. J.; Simpson, G. J.; Taylor, L. S., Selective detection and quantitation of organic molecule crystallization by second harmonic generation microscopy. *Analytical chemistry* **2010,** *82* (13), 5425-5432.

18. Zhu, Q.; Toth, S. J.; Simpson, G. J.; Hsu, H.-Y.; Taylor, L. S.; Harris, M. T., Crystallization and dissolution behavior of naproxen/polyethylene glycol solid dispersions. *The Journal of Physical Chemistry B* **2013,** *117* (5), 1494-1500.

19. Toth, S.; Madden, J.; Taylor, L.; Marsac, P.; Simpson, G., Selective imaging of active pharmaceutical ingredients in powdered blends with common excipients utilizing two-photon excited ultraviolet-fluorescence and ultraviolet-second order nonlinear optical imaging of chiral crystals. *Analytical chemistry* **2012,** *84* (14), 5869-5875.

20. Song, Z.; Sarkar, S.; Vogt, A. D.; Danzer, G. D.; Smith, C. J.; Gualtieri, E. J.; Simpson, G. J., Kinetic Modeling of Accelerated Stability Testing Enabled by Second Harmonic Generation Microscopy. *Analytical Chemistry* **2018**.

21. Chowdhury, A. U.; Ye, D. H.; Song, Z.; Zhang, S.; Hedderich, H. G.; Mallick, B.; Thirunahari, S.; Ramakrishnan, S.; Sengupta, A.; Gualtieri, E. J., Second Harmonic Generation Guided Raman Spectroscopy for Sensitive Detection of Polymorph Transitions. *Analytical chemistry* **2017,** *89* (11), 5958-5965.

22. Newman, J. A.; Schmitt, P. D.; Toth, S. J.; Deng, F.; Zhang, S.; Simpson, G. J., Parts per million powder X-ray diffraction. *Analytical chemistry* **2015,** *87* (21), 10950-10955.

23. Newman, J. A.; Zhang, S.; Sullivan, S. Z.; Dow, X. Y.; Becker, M.; Sheedlo, M. J.; Stepanov, S.; Carlsen, M. S.; Everly, R. M.; Das, C., Guiding synchrotron X-ray diffraction by multimodal video-rate protein crystal imaging. *Journal of synchrotron radiation* **2016,** *23* (4), 959-965.

24. Schmidt, S., GrainSpotter: a fast and robust polycrystalline indexing algorithm. *Journal of Applied Crystallography* **2014,** *47* (1), 276-284.

25. Chowdhury, A. U.; Dettmar, C. M.; Sullivan, S. Z.; Zhang, S.; Jacobs, K. T.; Kissick, D. J.; Maltais, T.; Hedderich, H. G.; Bishop, P. A.; Simpson, G. J., Kinetic trapping of metastable amino acid polymorphs. *Journal of the American Chemical Society* **2014,** *136* (6), 2404-2412.

CHAPTER 3. THEORETICAL FOUNDATION FOR ELECTRIC DIPOLE ALLOWED CHIRAL-SPECIFIC FLUORESCENCE OPTICAL ROTARY DISPERSION (F-ORD) FROM INTERFACIAL ASSEMBLIES

3.1 Introduction

The Absolute chirality plays a critical role in biological interactions, governing enzyme-substrate interactions.[1] To design a functioning pharmaceutical therapeutic agent, target chirality is typically a prerequisite. However, few probes are available to definitively characterize chirality. Vibrational CD (VCD) and Raman optical activity (ROA) are selective techniques commonly utilized for chiral sensing but are limited by low sensitivity.[2-3] Electronic CD (ECD) offers higher sensitivity, but the broad band nature of electronic transitions reduces specificity.[4] Fully electric dipole allowed chiral-specific effects including circular extinction are reasonably well-established in measurements of crystalline materials. In studies of achiral dyes incorporated during crystal growth, Kahr and coworkers have nicely demonstrated the observation of chiral-specificity for achiral dyes incorporated into chiral lattices.[5] In this instance, the circular dichroism observed arose from an interplay between birefringence in the crystal and linear dichroism from preferred crystal orientation and is thus limited to dye-doped crystalline and polycrystalline materials.[6] Alternative methods employing second order nonlinear optical (NLO) spectroscopy have been shown to be highly sensitive to chirality, also through an electric dipole–allowed mechanism.[7-9] Near 100% dichroic ratios have been observed for oriented binapthol monolayer films using second harmonic generation (SHG) CD.[10] In addition, Fourier transform microwave spectroscopy has been employed for electric dipole allowed enantiomer-specific detection methods via triply resonant microwave nonlinear wave mixing.[11-12] However, the accessibility of NLO approaches is reduced by the requirement of a pulsed laser source at optical frequencies and the complexity of the experiments in general. One-photon fluorescence (1PF), in contrast, does not require a coherent or pulsed, and can be easily implemented into existing fluorescence microscopes. Here, we propose a new spectroscopic method based on 1PF that is selective to chirality at interfaces.

3.2 Theory

A simple physical model explaining the prediction of electric dipole allowed chiral-specific fluorescence in uniaxial assemblies is shown in Figure 1 in the limiting case of orthogonally polarized absorption (blue arrow) and fluorescence (red arrow) transition moments. A non-zero net rotation in the primary axis of polarization can be observed between the projections of $\vec{\mu}^a$ and $\vec{\mu}^f$ on the *X*-*Y* plane. Excitation with linearly polarized light will result in fluorescence that, on average, yields a maximum in the polarized emission intensity that is rotated relative to the excitation axis. This rotation is the origin of the chiral-specific signal. From inspection of the graphic, the F-ORD process is non-reciprocal such that flipping the surface through a 180° rotation about the *X*-axis will result in the opposite sense of rotation.

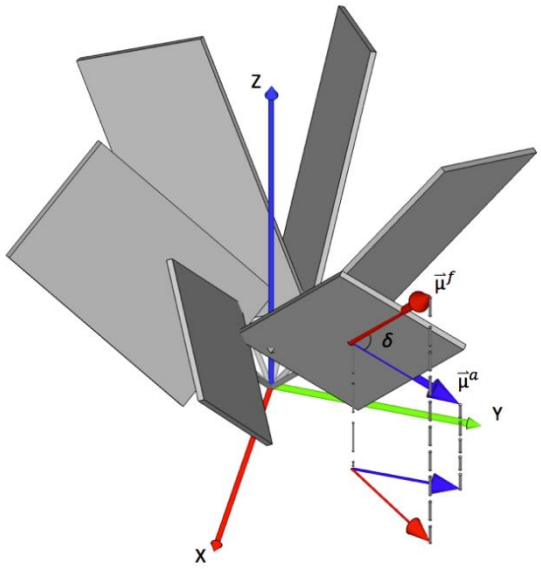

Figure 3-1 A graphic illustration of planar fluorophores (represented by gray plates) with uniaxial symmetry in the laboratory X-Y-Z frame. The Euler angle φ is uniformly sampled for the assembly. Detected signal is defined in the projection onto the laboratory X-Y plane. Y-polarized excitation results in fluorescence detected at an angle rotated clockwise, as shown in the projection.

The mathematical framework for chiral-specific fluorescence builds most directly on the electric dipole-allowed orientational mechanism underpinning chiral-specific four-wave mixing

described by Davis et al.[13] In this mechanism, a chiral-specific nonlinear optical field can be produced even in the absence of intrinsic chirality within the chromophore through chiral orientational arrangement in an ensemble. The macroscopic chirality arises purely through packing effects and does not require any coupling between chromophores or chiral distortion. Furthermore, because both the chiral and achiral responses are fully electric dipole allowed, they are often comparable in magnitude, yielding dichroic ratios approaching unity under favorable conditions. A qualitatively similar mechanism is well-established for describing the high sensitivity of chirality in surface second harmonic and sum frequency generation.

The connection between the experimental observables and the molecular properties can be constructed by starting with fundamental light matter interactions at the molecular level. The process of absorption can be described either by a transition dipole moment μ^i, or more formally by the imaginary component of the polarizability matrix α^{ij}, where *i, j* represent the polarization of the emission and excitation light respectively. The two formalisms are connected by the following equation describing the excitation from state *I* to state *n*. The damping term Γ describes the half width at half max of the lineshape function.

$$\alpha^{ij}(-\omega;\omega) = \frac{1}{\hbar}\sum_n \frac{\mu_{In}^i \mu_{nI}^j}{\omega_n - \omega - i\Gamma_n} + \frac{\mu_{In}^j \mu_{nI}^i}{\omega_n + \omega + i\Gamma_n} \tag{3.1}$$

For a molecule initially in the ground state such that I = 0, the first term in the summation will dominate, since the excited state lies at an energy higher than the initial state. In the case of fluorescence emission, the second term dominates, as the initial state is higher in energy than the state contributing to the resonance enhancement.[14] Only the imaginary contributions to the polarizability impact the overall attenuation or amplification of the optical field, corresponding to absorption or emission, respectively. The polarization-dependence of absorption and emission are dictated by the terms in the numerator. In a molecular coordinate system in which the *z'*-axis parallels the fluorescence emission transition moment and the absorption transition moment lies in the *x'*-z' plane, the fluorescence transition moment only has one nonzero term $\mu_{z'}^f = \left|\vec{\mu}^f\right|$ and the absorption transition moment has two components: $\left(\mu_{nI}^{x'}\right)^a = |(\vec{\mu}_{nI})^a| \sin\delta$ and $\left(\mu_{nI}^{z'}\right)^a = |(\vec{\mu}_{nI})^a| \cos\delta$ where δ defines the angle between the fluorescence and absorption transition moments consistent with Figure 3-1.

Using the relation $\vec{\mu}_{nm} = \vec{\mu}^{*}_{mn}$, the expression for the linear polarizability describing absorption in Equation (3.1) can be rewritten as follows for a molecule initially in the ground state I = 0.

$$\begin{aligned}
\alpha^{x'x'} &\cong S(\omega)\left|\bar{\mu}_{n0}\right|^2 \sin^2\delta \\
\alpha^{z'z'} &\cong S(\omega)\left|\bar{\mu}_{n0}\right|^2 \cos^2\delta \\
\alpha^{x'z'} &= \alpha^{z'x'} \cong S(\omega)\left|\bar{\mu}_{n0}\right|^2 \sin\delta\cos\delta
\end{aligned} \tag{3.2}$$

where the S(ω) describes the resonance line-shape function. If it is assumed that molecular rotation is slow relative to the fluorescence lifetime, the orientational averages connecting the molecular frame to the laboratory frame are performed over the combined coordinates describing absorption and emission.

In a general sense, the intensity of pure linearly polarized fluorescence as a function of the polarization rotation angle γ for linearly polarized excitation light depends on the following three trigonometric polynomial coefficients *A* - *C*.

$$I_n(\gamma) = A_n \cos^2\gamma + B_n \sin\gamma\cos\gamma + C_n \sin^2\gamma \tag{3.3}$$

In the above equation, n may refer to the Stokes frame horizontal polarization (H) or vertical polarization (V). These three coefficients are in turn related back to the molecular orientation distribution and the transition moments within the molecular frame. Furthermore, if the angle between the absorption and emission angles is defined to be δ described above, the expressions for the polynomial coefficients can be rewritten in terms of δ as shown below for H polarized detection.

$$A_H = K\left(\left|\bar{\mu}^f\right|^2\left|\bar{\mu}^a\right|^2\right)\left\{\begin{array}{l}
\cos^2\delta\left\langle\left(R_{Xz'}R_{Xz'}\right)^f\left(R_{Xz'}R_{Xz'}\right)^a\right\rangle \\
+2\sin\delta\cos\delta\left\langle\left(R_{Xz'}R_{Xz'}\right)^f\left(R_{Xx'}R_{Xz'}\right)^a\right\rangle \\
+\sin^2\delta\left\langle\left(R_{Xz'}R_{Xz'}\right)^f\left(R_{Xx'}R_{Xx'}\right)^a\right\rangle
\end{array}\right\} \tag{3.4}$$

$$B_H = K\left(\left|\bar{\mu}^f\right|^2\left|\bar{\mu}^a\right|^2\right)\left\{\begin{array}{l}
\cos^2\delta\left\langle\left(R_{Xz'}R_{Xz'}\right)^f\left(R_{Xz'}R_{Yz'}\right)^a\right\rangle \\
+\sin^2\delta\left\langle\left(R_{Xz'}R_{Xz'}\right)^f\left(R_{Xx'}R_{Yx'}\right)^a\right\rangle
\end{array}\right\} \tag{3.5}$$

$$C_H = K\left(\left|\vec{\mu}^{f}\right|^2\left|\vec{\mu}^{a}\right|^2\right)\begin{Bmatrix}\cos^2\delta\left\langle\left(R_{Xz'}R_{Xz'}\right)^{f}\left(R_{Yz'}R_{Yz'}\right)^{a}\right\rangle\\+2\sin\delta\cos\delta\left\langle\left(R_{Xz'}R_{Xz'}\right)^{f}\left(R_{Yx'}R_{Yz'}\right)^{a}\right\rangle\\+\sin^2\delta\left\langle\left(R_{Xz'}R_{Xz'}\right)^{f}\left(R_{Yx'}R_{Yx'}\right)^{a}\right\rangle\end{Bmatrix} \quad (3.6)$$

The degeneracy of the input photon polarizations ($\alpha^{x'y'} = \alpha^{y'x'}$) produces two orientational averages equal in magnitude but opposite in sign, yielding a net zero sin(δ)cos(δ) term for the B coefficient. Expressions for each of the eight orientational averages in Equations (3.4)-(3.6) for a uniform distribution in φ have been explicitly evaluated previously.[13] The orientational averages for the contribution in B_H are given by the following expressions.

$$\left\langle\left(R_{Xz'}R_{Xz'}\right)^{f}\left(R_{Xz'}R_{Yz'}\right)^{a}\right\rangle = 0 \quad (3.7)$$

$$\left\langle\left(R_{Xz'}R_{Xz'}\right)^{f}\left(R_{Xx'}R_{Yx'}\right)^{a}\right\rangle = \tfrac{1}{4}\left\langle\sin^2\theta\cos\theta\sin\psi\cos\psi\right\rangle \quad (3.8)$$

In the presence of a mirror plane containing the unique axis, the *B* term goes to zero due to the corresponding even symmetry in the distributions in ψ. Thus, only ensembles exhibiting chiral order will display this response; the *B* coefficient contribution to detected signal is hereby referred to as the chiral-specific signal. The origin of the chiral-specific signal can be understood from the nonzero orientational averages in Equations (3.8). Note that a chiral uniaxial assembly alone is thus insufficient to observe F-ORD experimentally; a nonzero orientational average $\left\langle\sin^2(\theta)\cos(\theta)\right\rangle$ is required and implied by the term polar order. Using a lipid monolayer on an air/water interface as an example, the aliphatic moiety for the ensemble is virtually always oriented away from the bulk liquid, giving the whole interface a polar orientation. In contrast, a bilayer of those same lipids can exhibit alignment about a unique axis, but no preferred orientation (i.e., polar order) and no corresponding F-ORD response. The B_H coefficient is given by the following equation as a function of orientational parameters and the transition moments of the fluorophore.

$$B_H \propto \left\langle\sin^2\theta\cos\theta\sin\psi\cos\psi\right\rangle\left(\left|\mu_z^{f}\right|^2\left|\mu_x^{a}\right|^2\right) = \left|\bar{\mu}^{f}\right|^2\left|\bar{\mu}^{a}\right|^2\sin^2\delta\left\langle\sin^2\theta\cos\theta\sin\psi\cos\psi\right\rangle \quad (3.9)$$

From Equation (3.9), three requirements must be met to exhibit chiral-specificity in the fluorescence produced from uniaxial assemblies: i) the assembly exhibits polar order, such that the expectation values over the polar tilt angle θ are nonzero, ii) the arrangement of the plane containing the absorption and fluorescence transition dipoles must exhibit a chiral twist such that the expectation values over ψ are nonzero, and iii) the transition moments for absorption and

fluorescence are nonparallel such that δ is nonzero. In the limit of a uniform distribution in ψ, both orientational averages in Equations (3.8) approach zero.

The magnitude of the F-ORD signal can be interpreted in the context of a linear intensity difference (LID) measurement most analogous to circular intensity difference measurements with circularly polarized excitation. In LID measurements, the polarized fluorescence intensity is measured for $+45°$ and $-45°$ linear polarizations, with the difference in the detected intensity directly connected to the F-ORD rotation angle.

$$LID \equiv \frac{I_H(+45) - I_H(-45)}{I_H(+45) + I_H(-45)} = \frac{B_H}{A_H + C_H} \tag{3.10}$$

There are an infinite set of angles which generate a maximal dissymmetry parameter due to the interplay between the functions of θ and δ. For $\delta = 90°$, LID is maximized at 25% for $\theta = 65.8°$ and $\psi = 22.3°$.The azimuthal distribution in molecular orientation results in a reduction in LID values relative to the theoretical maximum of 1 for an infinitely sharp azimuthal orientation distribution or for single molecules. Note, however, that typically reported electronic CD g values are on the order of 10^{-3}.

Evidence supporting the potential relevance of this proposed mechanism can be found in single molecule fluorescence studies of chiral molecules first reported by Barnes and coworkers, reproduced with permission in Figure 2. In that study, Barnes and coworkers observed dissymmetry parameter *g* related to differences in fluorescence intensity for right versus left circularly polarized excitation.[15] Clear statistically significant differences were observed in the histograms of *g* values produced for the two senses of helicity for the chiral fluorophores used.

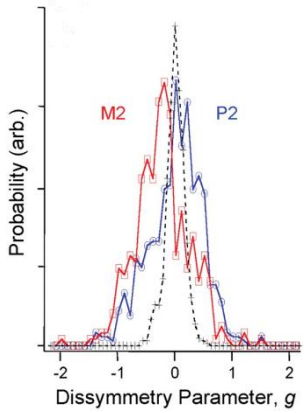

Figure 3-2 Normalized fluorescence-detected circular dichroism (FDCD) histogram published by Barnes and coworkers.[15] The blue and red traces represent the signal from right (*P2*) and left (*M2*) handed helical structures, respectively. Mean *g* values reported were 0.52 and -0.63, respectively; 2 orders of magnitude greater than the bulk response. Reproduced with permission.

In follow-up work by Cohen and coworkers,[16-17] it was suggested that the dichroic mirrors altered polarization incident to the sample. It was demonstrated that the dichroic mirror induced phase shifts and had different reflectivity efficiencies. Furthermore, corrections to ensure pure circular polarizations at the sample resulted in significant decreases in the spread and magnitude of *g*-values obtained. Cohen and coworkers concluded that the observation of nonzero dissymmetry could be attributed to the presence of linear dichroism rather than circular dichroism. In subsequent studies by Barnes and coworkers, a reduction in dissymmetry was confirmed when particular attention was taken to remove potential artifacts from linear dichroism, although the underlying sensitivity to absolute chirality remained.[18]

Interestingly, no subsequent work has to our knowledge appeared to address what are arguably the most exciting observations in the original study; namely the observed chiral specificity in the single molecule linear dichroism contributions to the Barnes' and coworkers' measurements. The results shown in Figure 2 demonstrate clear differences in the mean values of the dissymmetry factors for the two diastereomers at the interface. These observations can potentially be explained through the F-ORD mechanism proposed herein.

The presence of unanticipated F-ORD contributions in the prior experimental design can be understood by considering the influence of the Jones matrices for the optical path in the original study, as subsequently detailed by Cohen and coworkers. In brief, the Jones matrix describing the

polarization state of the incident circularly polarized light upon reflection from a dichroic mirror can be broken up into a complex component describing elliptically polarized light along the eigenpolarizations of the mirror and a purely real component corresponding to $\pm 45°$ linear polarization.

$$\begin{aligned}\vec{e}^{\,a} &= \begin{bmatrix} r_H^a & 0 \\ 0 & r_V^a \end{bmatrix} \tfrac{1}{\sqrt{2}} \begin{bmatrix} 1 \\ \pm i \end{bmatrix} = \begin{bmatrix} |r_H| & 0 \\ 0 & |r_V| e^{i\Delta} \end{bmatrix} \tfrac{1}{\sqrt{2}} \begin{bmatrix} 1 \\ \pm i \end{bmatrix} \\ &= \tfrac{1}{\sqrt{2}} \begin{bmatrix} |r_H^a / r_V^a| - \sin\Delta \\ \pm i \cos\Delta \end{bmatrix} + \tfrac{\sin\Delta}{\sqrt{2}} \begin{bmatrix} 1 \\ \pm 1 \end{bmatrix}\end{aligned} \tag{3.11}$$

In Equation (3.11), r_H^a and r_V^a refer to the complex-valued amplitude reflection coefficients for the dichroic mirror (assuming the *p* and *s* eigenpolarizations coincide with the *H* and *V* reference frames of the image), and Δ is the phase shift in the polarization state induced by the mirror, given by $\Delta = \arg(r_H^a / r_V^a)$. From Equation (3.11), the difference in detected intensity for $\pm 45°$ is directly connected to the chiral-specific coefficients B_H and B_V. For detection of horizontally polarized light the following equality emerges.

$$I_H\left(+45^0\right) - I_H\left(-45^0\right) = 2\left(\tfrac{1}{2} B_H\right)\left|t_H^f\right|^2 \tag{3.12}$$

Taking advantage of the identity $B_H = -B_V$, the integrated fluorescence intensity difference arising from residual linear dichroism can be connected to the transmission coefficients of the dichroic mirror along the return path at the fluorescence wavelength through the following relationship.

$$I_{tot}\left(+45^0\right) - I_{tot}\left(-45^0\right) = B_H\left|t_H^f\right|^2 + B_V\left|t_V^f\right|^2 = B_H\left(\left|t_H^f\right|^2 - \left|t_V^f\right|^2\right) \tag{3.13}$$

From previous measurements of dichroic mirrors performed by the Cohen group,[16] reasonable values of $\Delta = 0.79$ were recorded for one dichroic mirror, corresponding to as much as ~1/2 the incident light potentially contributing to linear dichroism. From Equation (3.13), the presence of a significant difference in transmissivity for the eigenpolarizations of the dichroic mirror prior to detection could provide one possible explanation for the observations of large dissymmetry factors directly tied to the sense of chirality. Conversely, unpolarized detection of the total fluorescence should yield no selectivity for chirality, consistent with the two transmissivity terms in Equation (3.13) being equal. It would also explain the reductions in this sensitivity when using pure circular polarizations, corresponding to the case of $\Delta \cong 0$. Note that the reduction in signal observed with circularly polarized light is entirely consistent with the Cohen response in 2009, where it was noted

that careful treatment of polarization purity to ensure pure CPL at the sample resulted in sharp collapse of the distribution of g about zero. Finally, it suggests that the overall sensitivity to chirality could be significantly improved yet further through optimization of the experiment to explicitly target F-ORD measurements.

It is interesting to compare and contrast the proposed mechanism with previous work by Cohen and coworkers, describing "superchiral" light arises in the region in the vicinity of nodes present at highly reflective interfaces.[16, 19-20] In brief, the electric dipole contributions approach zero at a node, while the same effect does not arise for magnetic dipole contributions. As such, suppression of the electric dipole induced fluorescence results in a relative enhancement in the chiral-specific magnetic dipole contributions and a correspondingly large dissymmetry factor. This mechanism produces a greater g value with a maximum signal detected for pure circularly polarized light and zero signal for linearly polarized light. In contrast, the F-ORD mechanism, as detailed above, yields a minimum g value for circularly polarized light as evidenced by the 2009 response to the original Barnes manuscript.[16] In a follow-up manuscript by Barnes and coworkers in 2012, it was shown that careful treatment to reduce linear polarization contamination resulted in a reduction in dissymmetry parameters g, consistent with the predictions of F-ORD and contrary to those of the "superchiral" light mechanism.[21]

It is worthwhile to compare and contrast the chiral-specific response predicted for fluorescence with the fully electric dipole allowed chiral-specific Raman from oriented assemblies first considered several years ago by Efrima and subsequently refined by Hecht and Barron.[22-23] In brief, symmetry arguments indicated the possibility of electric dipole-allowed chiral-specific Raman optical activity (ROA) in chiral assemblies exhibiting polar order. In that work, electric dipole-allowed ROA was predicted to be possible from macroscopic symmetry arguments, with the ROA scaling with the anti-symmetric component of the Raman tensor. Since anti-symmetry is enhanced near electronic resonance, ROA was predicted to be enhanced in resonance Raman measurements. These predictions were subsequently confirmed experimentally and put to great advantage in surface-enhanced Raman measurements.[24] This confirmation has led to a recent growth in SEROA arising from molecules assembled at the surfaces of metal nanoparticles. Despite the successes of SEROA, few detailed molecular level interpretations have emerged for the origins of the chiral specificity in terms of the molecular orientation distribution at the interface, such that ab initio interpretations of SEROA measurements for absolute chirality determination remain challenging.

More recent independent studies of coherent four-wave mixing of uniaxial assemblies[13] may potentially help clarify the origin of the chiral specificity of spontaneous Raman in SEROA measurements and their possible connection to chiral-specific fluorescence. In that work, explicit expressions were derived for the orientational averages connecting the molecular frame to the interfacial frame for all coherent four-wave mixing measurements. Fortunately, both fluorescence and the spontaneous Raman processes can be treated mathematically with the same framework as four wave mixing, although with two of the four fields produced by the sample rather than one as in CARS. These general expressions are equally valid for spontaneous Raman and fluorescence, providing a route for clarifying the molecular-level requirements for both electric dipole allowed chiral-specific Raman and F-ORD.

3.3 Conclusion

In summary, a framework for the theoretical description of chiral-specific fluorescence was described. The proposed model imposes the following molecular constraints: i) the presence of a significant difference between the absorption and emission transition moment orientations within the molecular frame, ii) polar order of a uniaxial interface, and iii) ensemble chirality. The F-ORD chiral-specific signal was mathematically connected to the *B* polynomial coefficient in polarization rotation measurements and to linear intensity difference measurements of chiral assemblies. The model provides a novel electric-dipole allowed mechanism for chiral-specific fluorescence, which may explain the remarkable linear dissymmetry parameters reported by Barnes and Cohen previously. Furthermore, the described framework lends itself to future extension into the theoretical treatment of SEROA measurements, providing increased generality over previous treatments.

3.4 References

1. Kohls, H.; Steffen-Munsberg, F.; Höhne, M., Recent achievements in developing the biocatalytic toolbox for chiral amine synthesis. *Current opinion in chemical biology* **2014,** *19*, 180-192.

2. Syme, C. D.; Blanch, E. W.; Holt, C.; Jakes, R., A Raman optical activity study of rheomorphism in caseins, synucleins and tau. *European Journal of Biochemistrty* **2002,** *269*, 148-156.

3. Barron*, L. D.; Hecht, L.; McColl, I. H.; Blanch, E. W., Raman optical activity comes of age. *Molecular Physics* **2004**.

4. Sreerama, N.; Woody, R. W., Estimation of protein secondary structure from circular dichroism spectra: comparison of CONTIN, SELCON, and CDSSTR methods with an expanded reference set. *Analytical biochemistry* **2000,** *287* (2), 252-260.

5. Kahr, B.; Freudenthal, J.; Gunn, E., Crystals in Light. *Accounts Chem. Res.* **2010,** *43* (5), 684-692.

6. Claborn, K.; Chu, A. S.; Jang, S. H.; Su, F. Y.; Kaminsky, W.; Kahr, B., Circular extinction imaging: Determination of the absolute orientation of embedded chromophores in enantiomorphously twinned LiKSO4 crystals. *Crystal Growth & Design* **2005,** *5* (6), 2117-2123.

7. Rodrigues, S. P.; Lan, S.; Kang, L.; Cui, Y.; Cai, W., Nonlinear Imaging and Spectroscopy of Chiral Metamaterials. *Advanced Materials* **2014,** *26* (35), 6157-6162.

8. Lee, H.; Huttunen, M. J.; Hsu, K. J.; Partanen, M.; Zhuo, G. Y.; Kauranen, M.; Chu, S. W., Chiral imaging of collagen by second-harmonic generation circular dichroism. *Biomedical Optics Express* **2013,** *4* (6), 909.

9. Haupert, L. M.; Simpson, G. J., Chirality in Nonlinear Optics. In *Annual Review of Physical Chemistry*, Annual Reviews: Palo Alto, 2009; Vol. 60, pp 345-365.

10. Petralli-Mallow, T.; Wong, T. M.; Byers, J. D.; Yee, H. I.; Hicks, J. M., Circular dichroism spectroscopy at interfaces: a surface second harmonic generation study. *The Journal of Physical Chemistry* **1993,** *97* (7), 1383-1388.

11. Patterson, D.; Schnell, M.; Doyle, J. M., Enantiomer-specific detection of chiral molecules via microwave spectroscopy. *Nature* **2013,** *497* (7450), 475-+.

12. Lobsiger, S.; Perez, C.; Evangelisti, L.; Lehmann, K. K.; Pate, B. H., Molecular Structure and Chirality Detection by Fourier Transform Microwave Spectroscopy. *Journal of Physical Chemistry Letters* **2015,** *6* (1), 196-200.

13. Davis, R. P.; Moad, A. J.; Goeken, G. S.; Wampler, R. D.; Simpson, G., J., Selection Rules and Symmetry Relations for Four-Wave Mixing measurements of Uniaxial Assemblies. *J. Phys. Chem. B* **2008,** *112*, 5834-5848.

14. Moad, A. J.; Simpson, G. J., Self-consistent approach for simplifying the interpretation of nonlinear optical and multiphoton phenomena. *J. Phys. Chem. A* **2005,** *109*, 1316-1323.

15. Hassey, R.; Swain, E. J.; Hammer, N. I.; Venkataraman, D.; Barnes, M. D., Probing the chiroptical response of a single molecule. *Science* **2006,** *314* (5804), 1437-1439.

16. Tang, Y. Q.; Cook, T. A.; Cohen, A. E., Limits on Fluorescence Detected Circular Dichroism of Single Helicene Molecules. *Journal of Physical Chemistry A* **2009,** *113* (22), 6213-6216.

17. Cohen, A.; Tang, Y. Q., Reply to "Comment on 'Limits on Fluorescence Detected Circular Dichroism of Single Helicene Molecules'". *Journal of Physical Chemistry A* **2009,** *113* (35), 9759-9759.

18. Hassey-Paradise, R.; Cyphersmith, A.; Tilley, A. M.; Mortsolf, T.; Basak, D.; Venkataraman, D.; Barnes, M. D., Dissymmetries in Fluorescence Excitation and Emission from Single Chiral Molecules. *Chirality* **2009,** *21* (1E), E265-E276.

19. Tang, Y. Q.; Cohen, A. E., Optical Chirality and Its Interaction with Matter. *Phys Rev Lett* **2010,** *104* (16).

20. Tang, Y. Q.; Cohen, A. E., Enhanced Enantioselectivity in Excitation of Chiral Molecules by Superchiral Light. *Science* **2011,** *332* (6027), 333-336.

21. Cyphersmith, A.; Surampudi, S.; Casey, M. J.; Jankowski, K.; Venkataraman, D.; Barnes, M. D., Chiroptical Dissymmetries in Fluorescence Excitation from Single Molecules of (M-2) Helicene Dimers. *J Phys Chem A* **2012,** *116* (22), 5349-5352.

22. Hecht, L.; Barron, L. D., RAYLEIGH AND RAMAN OPTICAL-ACTIVITY FROM CHIRAL SURFACES. *Chemical Physics Letters* **1994,** *225* (4-6), 525-530.

23. Efrima, S., RAMAN OPTICAL-ACTIVITY OF MOLECULES ADSORBED ON METAL-SURFACES - THEORY. *Journal of Chemical Physics* **1985,** *83* (3), 1356-1362.

24. Vargek, M.; Freedman, T. B.; Lee, E.; Nafie, L. A., Experimental observation of resonance Raman optical activity. *Chem Phys Lett* **1998,** *287* (3-4), 359-364.

CHAPTER 4. SECOND HARMONIC GENERATION OF UNPOLARIZED LIGHT

4.1 Introduction

The symmetry requirements for second order nonlinear optical processes make polarization dependent SHG (PD-SHG) a highly selective image modality for biostructures[1-4], protein crystals[5] and active pharmaceutical ingredients[5-6]. One major advantage of NLO microscopy is the increase of the penetration depth[7-9], where the incident light is within the near infrared (NIR) transparent window for biological tissues. The quadratic dependence of the incident power for NLO process generates significant less out of plane signal. However, the scattering and birefringence effects of tissues significantly degrades the purity of polarization, making polarization dependent SHG measurement difficult for thick samples. Several efforts have been implemented that considered the effects of partial depolarization including optical clearing[10], careful booking keeping of the polarization states[3-4, 11]. However, methods based on Jones calculus do not consider the SHG raised from the depolarized light. Despite the simplicity of Jones framework, the two-element vector representation of Jones framework cannot describe a polarization state with mixed linear and circular polarization components.

Recently, polarization dependent studies based on Mueller calculus have been demonstrated. A "super-Mueller" theory based Stokes-Mueller framework was introduced by Barzda and co-workers.[12-14] Unlike the Jones calculus, a four-element Stokes vector of sums and differences in intensity at different polarization states is used to describe the total polarization state. A comparison between Jones and Mueller framework is summarized in Table 1. However, the increase of vector length for the Mueller calculus introduces 36 unique elements.[12, 15] A large number of observables are required to populate the super-Mueller matrix.

Table 4.1 Comparison between Jones and Mueller framework in linear optics

	Jones Calculus	**Mueller Calculus**
General Forms	$\begin{pmatrix} E_x(t) \\ E_y(t) \end{pmatrix} = \begin{pmatrix} E_{0x}e^{i\phi_x} \\ E_{0y}e^{i\phi_y} \end{pmatrix} e^{i(kz-\omega t)}$	$\vec{s} = \begin{pmatrix} s_0 \\ s_1 \\ s_2 \\ s_3 \end{pmatrix} = \begin{pmatrix} I_H + I_V \\ I_H - I_V \\ I_{+45^\circ} - I_{-45^\circ} \\ I_{RCP} - I_{LCP} \end{pmatrix}$
Graphical Representations	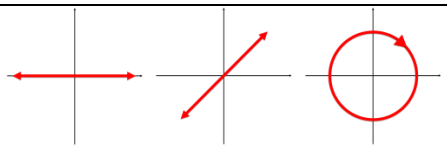	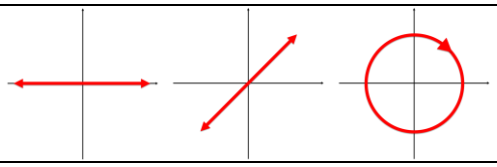
Mathematical Representations	$\begin{bmatrix} 1 \\ 0 \end{bmatrix}$ $\frac{1}{\sqrt{2}}\begin{bmatrix} 1 \\ 1 \end{bmatrix}$ $\frac{1}{\sqrt{2}}\begin{bmatrix} 1 \\ i \end{bmatrix}$	$I_0\begin{bmatrix} 1 \\ 1 \\ 0 \\ 0 \end{bmatrix}$ $I_0\begin{bmatrix} 1 \\ 0 \\ 1 \\ 0 \end{bmatrix}$ $I_0\begin{bmatrix} 1 \\ 0 \\ 0 \\ 1 \end{bmatrix}$
Polarization Out with Polarizability Tensor	$\vec{e}^{\,out} = \vec{\chi}_J \cdot \vec{e}^{\,in}$	$\vec{s}^{\,out} = M \cdot \vec{s}^{\,in}$
Connection	$M = A \cdot \left(\chi_J^* \otimes \chi_J \right) \cdot A^{-1}$	

More recently, a theoretical framework has been developed to bridge the Mueller and Jones calculus.[16] The contribution of depolarization can be implemented with a single adjustable parameter α. This framework reduces the number of unique nonzero Mueller tensor elements that is required to describe the observables by integration of local-frame symmetry. More importantly, the use of Jones tensor provides direct comparison with the existing references. In this chapter, we study the polarization dependent measurements of SHG with the Jones-Mueller framework at one extreme case: completely depolarized incident light.

4.2 Theory

4.2.1 Connecting Jones and Mueller Frameworks for Polarization Dependent SHG Measurement

To describe the polarization dependent SHG with Mueller framework, the Stokes vector of the detected second harmonic signal can be written with rank three Mueller tensor $M^{(2)}$ in the following form as Eq. (4.1) and its vectorized form as Eq. (4.2).

$$\vec{s}_{det}^{2\omega} = \boldsymbol{M}_{det}^{(2)} : \vec{s}^{\omega}\vec{s}^{\omega} \tag{4.1}$$

$$\vec{s}_{det}^{2\omega} = \left[I_4 \otimes \left(\vec{s}^{\omega}\right)^T \otimes \left(\vec{s}^{\omega}\right)^T \right] \cdot \vec{\boldsymbol{M}}_{det} \tag{4.2}$$

I_4 is a 4 by 4 identity matrix and $\vec{M}$ is the 64-element ascending vectorized form of the Mueller tensor. For completely depolarized light, s_1, s_2, and s_3 equal to 0. Under the assumption that s_0 is the only nonzero entry in the Stokes vector for the unpolarized fundamental, only a subset of 4 elements within the Mueller tensor (M_{000}, M_{100}, M_{200}, and M_{300}, corresponding to the decimal positions of 0, 16, 32 and 48 in the vectorized form) contributes to the Stokes vector as shown in Eq. (4.3).

$$\begin{bmatrix} s_0 \\ s_1 \\ s_2 \\ s_3 \end{bmatrix}^{2\omega} = \begin{bmatrix} M_{000} \\ M_{100} \\ M_{200} \\ M_{300} \end{bmatrix} : \vec{s}_{in}^{\omega}\vec{s}_{in}^{\omega} \tag{4.3}$$

To introduce the Jones hyperpolarizability tensor $\chi^{(2)}$ into the Mueller framework, $\vec{\boldsymbol{M}}_{det}$ in Eq. (4.2) was replaced with the expression bridging the Mueller and Jones frameworks that derived in earlier work as shown in Eq. (4.4).

$$\vec{M} = \left[A \otimes \left(A^{-1}\right)^T \otimes \left(A^{-1}\right)^T \right] \cdot \overline{\left(\chi_J^{(2)*} \otimes \chi_J^{(2)}\right)} \tag{4.4}$$

$$A = \begin{bmatrix} 1 & 0 & 0 & 1 \\ 1 & 0 & 0 & -1 \\ 0 & 1 & 1 & 0 \\ 0 & i & -i & 0 \end{bmatrix}$$

The full vectorized form of Eq. (4.2) can be rewritten as the following form, which allows identification of the nonzero combinations of Jones tensor elements that contributes to the SHG produced with unpolarized fundamental.

$$\vec{s}^{\,2\omega} = \left[I_4 \otimes \left(\vec{s}^{\,\omega}\right)^T \otimes \left(\vec{s}^{\,\omega}\right)^T \right] \cdot \left[A \otimes \left(A^{-1}\right)^T \otimes \left(A^{-1}\right)^T \right] \cdot \overline{\left(\chi_J^{(2)*} \otimes \chi_J^{(2)}\right)} \tag{4.5}$$

Taking advantage of the identity relationship $(A \otimes B) \cdot (C \otimes D) = (A \cdot B) \otimes (C \cdot D)$ and equality $B^T \cdot C^T = (\mathrm{C} \cdot B)^T$, Eq. (4.5) can be rearranged into Eq. (4.6).

$$\vec{s}^{\,2\omega} = A \cdot \left\{ I_4 \otimes \left(A^{-1} \cdot \vec{s}^{\,\omega}\right) \otimes \left(A^{-1} \cdot \vec{s}^{\,\omega}\right) \right\}^T \cdot \overline{\left(\chi_J^{(2)*} \otimes \chi_J^{(2)}\right)} \tag{4.6}$$

Only two nonzero entries for fully depolarized light remains in the vector $A^{-1} \cdot \vec{s}^{\,\omega}$.

$$A^{-1} \cdot \vec{s}^{\,\omega} = \tfrac{1}{2} \begin{bmatrix} 1 \\ 0 \\ 0 \\ 1 \end{bmatrix} \tag{4.7}$$

The Kronecker product of $\left(A^{-1} \cdot \vec{s}^{\,\omega}\right) \otimes \left(A^{-1} \cdot \vec{s}^{\,\omega}\right)$ generates a 16-element vector with 4 nonzero entries: 0, 3, 12, and 15. After Kronecker product with an identity matrix, additional 4 nonzero entries are generated with the indices 16, 19, 28, and 31. The first 4 entries exclusively contributes to $s_0^{2\omega}$ and the second 4 entries exclusively contribute to $s_1^{2\omega}$. After identifying all contributing laboratory frame $\chi^{(2)}$ tensor elements for each element in the Stokes vector, the product of the term in curly brackets in Eq. (4.6) can be written as Eq. (4.8), where the 0 indicates the laboratory horizonal axis and 1 indicates the laboratory vertical axis.

$$\begin{bmatrix} s_0 \\ s_1 \\ s_2 \\ s_3 \end{bmatrix}^{2\omega} = \frac{1}{4}\begin{bmatrix} 1 & 0 & 0 & 1 \\ 1 & 0 & 0 & -1 \\ 0 & 1 & 1 & 0 \\ 0 & i & -i & 0 \end{bmatrix}\begin{bmatrix} \chi^*_{000}\chi_{000} + \chi^*_{001}\chi_{001} + \chi^*_{010}\chi_{010} + \chi^*_{011}\chi_{011} \\ \chi^*_{000}\chi_{100} + \chi^*_{001}\chi_{101} + \chi^*_{010}\chi_{110} + \chi^*_{011}\chi_{111} \\ \chi^*_{100}\chi_{000} + \chi^*_{101}\chi_{001} + \chi^*_{110}\chi_{010} + \chi^*_{111}\chi_{011} \\ \chi^*_{100}\chi_{100} + \chi^*_{101}\chi_{101} + \chi^*_{110}\chi_{110} + \chi^*_{111}\chi_{111} \end{bmatrix} \tag{4.8}$$

4.2.2 Connecting Local and Laboratory Frames

For polarization dependent SHG measurements of collagen, the number of nonzero Jones tensor element can be significantly reduced due to its symmetry. When the primary axis of the collagen fiber (z′) aligns along the horizontal laboratory-frame axis (H), only four sets of the Jones tensor elements $\chi_{z'z'z'}$, $\chi_{z'x'x'}$, $\chi_{x'x'z'} = \chi_{x'z'x'}$, and $\chi_{x'y'z'} = \chi_{x'z'y'} = -\chi_{y'x'z'} = -\chi_{y'z'x'}$ are nonzero. The chiral terms are relatively weak and can be neglected when the fibers aligned within the field of view. The number of nonzero elements can be further reduced to $\chi_{000} = \chi_{z'z'z'}$, $\chi_{011} = \chi_{z'x'x'}$, and $\chi_{110} = \chi_{101} = \chi_{x'x'z'}$. The Stokes vector can be expressed as following form.

$$\begin{bmatrix} s_0 \\ s_1 \\ s_2 \\ s_3 \end{bmatrix}^{2\omega} = \frac{1}{4}\begin{bmatrix} \left|\chi_{z'z'z'}\right|^2 + \left|\chi_{z'x'x'}\right|^2 + 2\left|\chi_{x'x'z'}\right|^2 \\ \left|\chi_{z'z'z'}\right|^2 + \left|\chi_{z'x'x'}\right|^2 - 2\left|\chi_{x'x'z'}\right|^2 \\ 0 \\ 0 \end{bmatrix}_{\phi=0} \tag{4.9}$$

For collagen within principle axis oriented at an arbitrary angle ϕ, the vectorized Mueller tensor can be calculated through rotation operation described in Eq. (4.10).

$$\begin{aligned} \bar{M}_L &= \left(\boldsymbol{\mathcal{R}}_\phi \otimes \boldsymbol{\mathcal{R}}_\phi \otimes \boldsymbol{\mathcal{R}}_\phi\right)\cdot \bar{M}_l' \\ \boldsymbol{\mathcal{R}}_\phi &= A\cdot\left(R_\phi \otimes R_\phi\right)\cdot A^{-1} \\ R_\phi &= \begin{bmatrix} \cos\phi & \sin\phi \\ -\sin\phi & \cos\phi \end{bmatrix} \end{aligned} \tag{4.10}$$

Applying the rotation operation to Eq. (4.2) yields the following expression.

$$\vec{s}^{\,2\omega} = \left[I_4 \otimes \left(\vec{s}^{\,\omega}\right)^T \otimes \left(\vec{s}^{\,\omega}\right)^T\right]\cdot\left(\boldsymbol{\mathcal{R}}_\phi \otimes \boldsymbol{\mathcal{R}}_\phi \otimes \boldsymbol{\mathcal{R}}_\phi\right)\cdot \bar{M}_l' \tag{4.11}$$

Taking a similar approach for deriving Eq. (4.11), the rotation operation can be implemented for the vectorized form of Eq. (4.5) as Eq. (4.12).

$$\vec{s}^{\,2\omega} = \tfrac{1}{4}\left[I_4 \otimes \left(\vec{s}^{\,\omega}\right)^T \otimes \left(\vec{s}^{\,\omega}\right)^T \right] \cdot \left[A \otimes \left(A^{-1}\right)^T \otimes \left(A^{-1}\right)^T \right] \cdot \left[R_\phi \otimes R_\phi \otimes R_\phi \otimes R_\phi \otimes R_\phi \otimes R_\phi \right] \cdot \overline{\left(\chi_l^{(2)*} \otimes \chi_l^{(2)} \right)} \tag{4.12}$$

After explicitly evaluate the rotation operations, the measured Stokes vector can be described with the projections of 4 Jones tensor elements with Eq. (4.13).

$$\begin{bmatrix} s_0 \\ s_1 \\ s_2 \\ s_3 \end{bmatrix}^{2\omega} = \tfrac{1}{4} \begin{bmatrix} 1 & 1 & 1 & 1 \\ \cos^2\phi - \sin^2\phi & \cos^2\phi - \sin^2\phi & \sin^2\phi - \cos^2\phi & \sin^2\phi - \cos^2\phi \\ 2\sin\phi\cos\phi & 2\sin\phi\cos\phi & 2\sin\phi\cos\phi & 2\sin\phi\cos\phi \\ 0 & 0 & 0 & 0 \end{bmatrix} \cdot \begin{bmatrix} \left|\chi_{z'z'z'}\right|^2 \\ \left|\chi_{z'x'x'}\right|^2 \\ \left|\chi_{x'z'x'}\right|^2 \\ \left|\chi_{x'x'z'}\right|^2 \end{bmatrix} \tag{4.13}$$

Combining trigonometric identities and the equality of $\left|\chi_{x'x'z'}\right|^2 = \left|\chi_{x'z'x'}\right|^2$ for SHG measurement, this expression can be further simplified into the following form.

$$\begin{bmatrix} s_0 \\ s_1 \\ s_2 \\ s_3 \end{bmatrix}^{2\omega} = \tfrac{1}{4} \begin{bmatrix} 1 & 1 & 1 \\ \cos(2\phi) & \cos(2\phi) & -\cos(2\phi) \\ -\sin(2\phi) & -\sin(2\phi) & \sin(2\phi) \\ 0 & 0 & 0 \end{bmatrix} \begin{bmatrix} \left|\chi_{z'z'z'}\right|^2 \\ \left|\chi_{z'x'x'}\right|^2 \\ 2\left|\chi_{x'x'z'}\right|^2 \end{bmatrix} \tag{4.14}$$

For z-cut quartz and collagen[3-5, 18], the magnitude of $\chi_{z'x'x'}$ is approximately equal to the magnitude of $\chi_{x'x'z'}$. In the limit of $\beta_{zxx} \cong \beta_{xxz}$, Eq. (4.14) can be expressed with a 2-parameter ($\rho \equiv \chi_{z'z'z'} / \chi_{z'x'x'}$, ϕ) expression as Eq. (4.15).

$$\begin{bmatrix} s_0 \\ s_1 \\ s_2 \\ s_3 \end{bmatrix}^{2\omega} = \frac{\left|\chi_{z'x'x'}\right|^2}{4} \begin{bmatrix} 1 & 1 & 1 \\ \cos(2\phi) & \cos(2\phi) & -\cos(2\phi) \\ -\sin(2\phi) & -\sin(2\phi) & \sin(2\phi) \\ 0 & 0 & 0 \end{bmatrix} \begin{bmatrix} \left|\rho\right|^2 \\ 1 \\ 2 \end{bmatrix} \tag{4.15}$$

Both Eqs. (4.14) and (4.15) are derived under the assumption of a polar tilt angle $\theta = \pi/2$, corresponding to a fiber axis within the FoV. For samples with a polar tilt angle other than $\pi/2$, the measured ρ equals the ratio of projection of $\chi_{z'z'z'}$ and $\chi_{z'x'x'}$ onto the laboratory *X*-*Z* plane, denoted as χ_{XXX} / χ_{XYY}. To avoid confusion in the later discussion, the ratio of local frame tensor $\chi_{z'z'z'} / \chi_{z'x'x'}$ is denoted as ρ_l and the measured laboratory frame ratio is denoted as $\chi_{z'z'z'} / \chi_{z'x'x'}$.

4.3 Instrumentation, Sample Preparation and Data Analysis

To experimentally validate the prediction of SHG from unpolarized fundamental, a depolarizer (DPP-25B, Thorlabs) was inserted into the Fourier plane of a beam-scanning SHG microscope described in details previously.[5] The SHG images were acquired with 800 nm incident light with either a 10×, 0.3 NA or 20×, 0.4 NA objective. A polarizer was placed in front of the detector in an automatic rotation stage. The polarization of the SHG signal was analyzed by mechanical rotation of the polarizer from 0 to 180 degrees with 3-degree intervals.

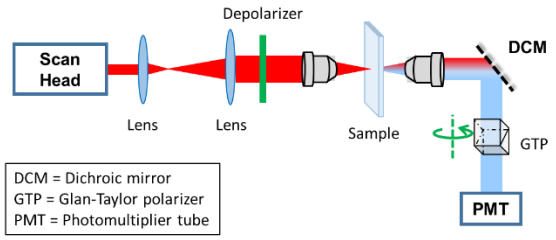

Figure 4-1 System schematic for depolarized SHG measurement

Mouse tails were decalcified in the solution of 23% formic acid, 4% formalin, and 1% methanol for 2 hours and then sectioned longitudinally with a microtome into 4 μm thick slide.

To recover ρ, a pixel by pixel nonlinear fit was performed with the acquired image set with Eq. (4.16).

$$I^{2\omega}\left(\phi_{pol}\right)=\frac{C}{8}\left[\left(\left|\rho\right|^{2}+3\right)+\left(\left|\rho\right|^{2}-1\right)\cos\left(2\phi_{pol}-2\phi\right)\right] \tag{4.16}$$

where the ϕ_{pol} is denoted for the angle of polarizer. Eq. (4.16) was derived from Eq. (4.15) by adding the first two elements of the Stokes vector.

4.4 Results and Discussion

To validate the theory, polarization dependent SHG of z-cut quartz was first measured as z-cut quartz has well-defined nonlinear optical properties (ρ = -1) and induces no birefringence when light propagates along its z-axis. Figure 4-2 shows the normalized measured SHG intensity from

z-cut quartz with linearly polarized and fully depolarized light as a function of angle of detection polarizer ϕ_{pol} and azimuthal rotation angle of z-cut quartz ϕ, respectively. Theoretical fitting was performed for the linearly polarized fundamental with Eq.(4.17).

$$I^{2\omega}\left(\phi,\phi_{pol}\right)=C\cdot\sin^2\left(3\phi-\phi_{pol}\right) \tag{4.17}$$

Excellent agreement between the experimental observations and theoretical predictions was observed.

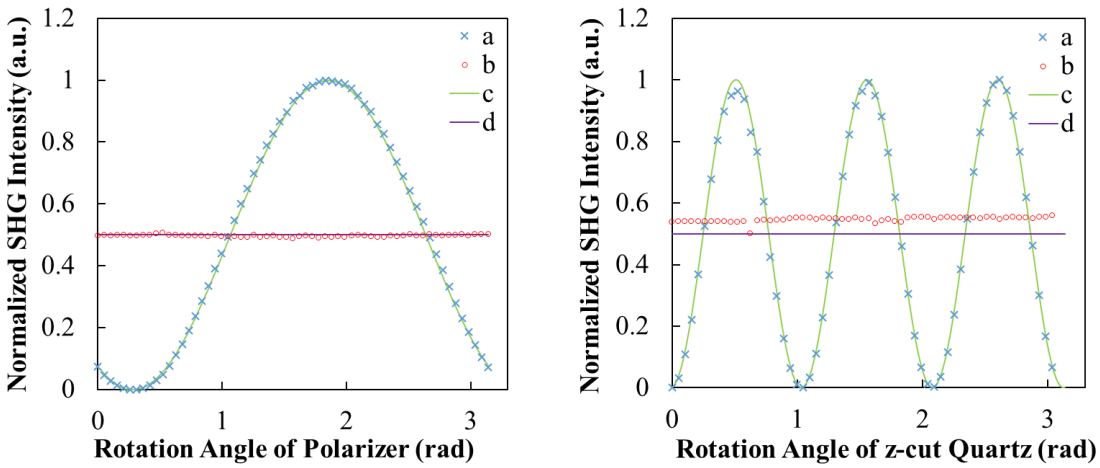

Figure 4-2 Left: polarization dependent SHG from z-cut quartz as a function of polarizer rotation with (a) vertically polarized and (b) depolarized fundamental overlaid with theoretical fitting (c) and prediction (d). Right: polarization dependent SHG from z-cut quartz as a function of sample rotation angle with (a) vertically polarized and (b) depolarized fundamental overlaid with theoretical fitting (c) and prediction (d).

Polarization dependent SHG measurements from collagen within a sectioned mouse tail were performed and analyzed with the method described in section 4.3. A map of fiber orientation (ϕ) was generated and overlaid in Figure 4-3 (A). The fiber orientation was also analyzed by *OrientationJ*, a plugin for *ImageJ*[19-20] and plotted in Figure 4-3 (B). The orientation distribution recovered from both methods was overlaid in Figure 4-3 (C) along with the detected SHG intensity for a selected pixel as a function of detection polarizer angle (D). Overall, good agreement was observed between the orientation recovered from image analysis and nonlinear fitting.

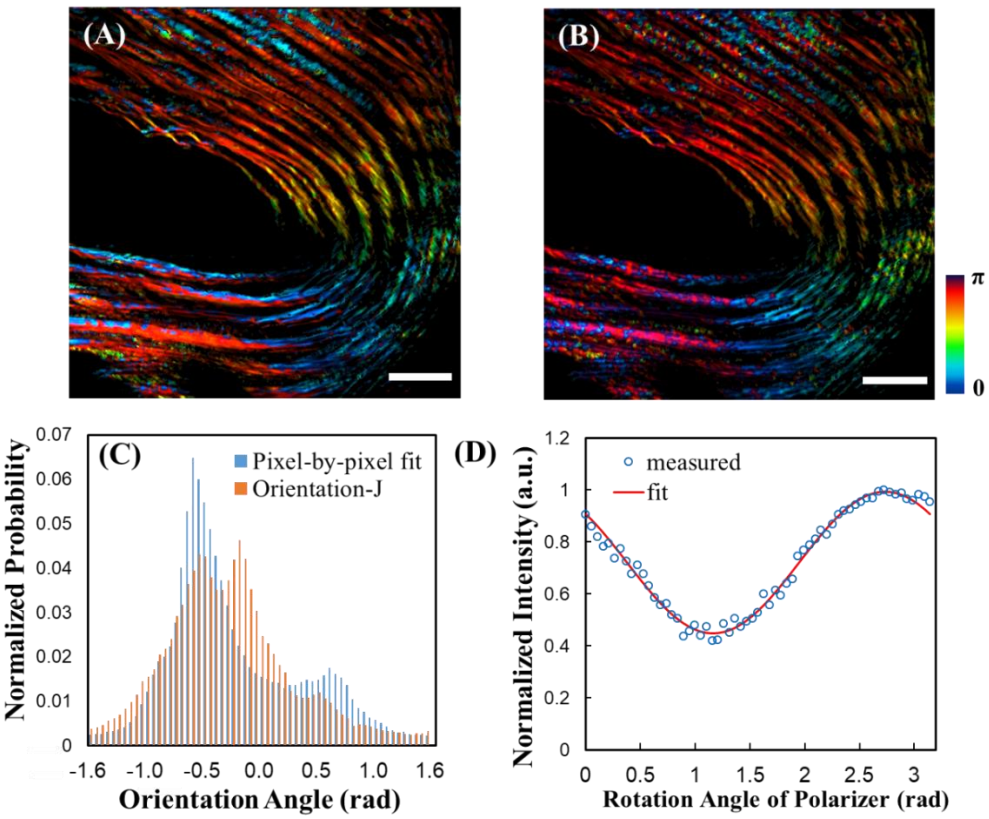

Figure 4-3 Polarization dependent SHG measurement of sectioned mouse tail.

The recovered laboratory-frame ratio ρ had a modal value of 1.69, which is consistent with previous reports.[4, 21] The map and histogram of ρ are shown in Figure 4-4 (A) and (B), respectively. The deviation for the recovered ρ is attributed to inaccuracies the assumption of the polar tilt angles equaling to π/2. To study the effect of out of plane tilt, a constant literature values for the local-frame $\rho_l = 1.7$ was used to recover the polar tilt angle with Eq. (4.18). The mathematical relation was derived by projecting local frame onto the lab frame. Detailed derivation can be found in a previous publication. [22]

$$\theta = \arcsin\left(\sqrt{\frac{\rho - 3}{\rho_l - 3}}\right) \tag{4.18}$$

Figure 4-4 (C) shows a map of recovered polar tilt angle for the mouse tail. A considerable amount of the collagen fibers had a polar tilt angle other than π/2. This phenomenon is more pronounced in the bending region in the field of view.

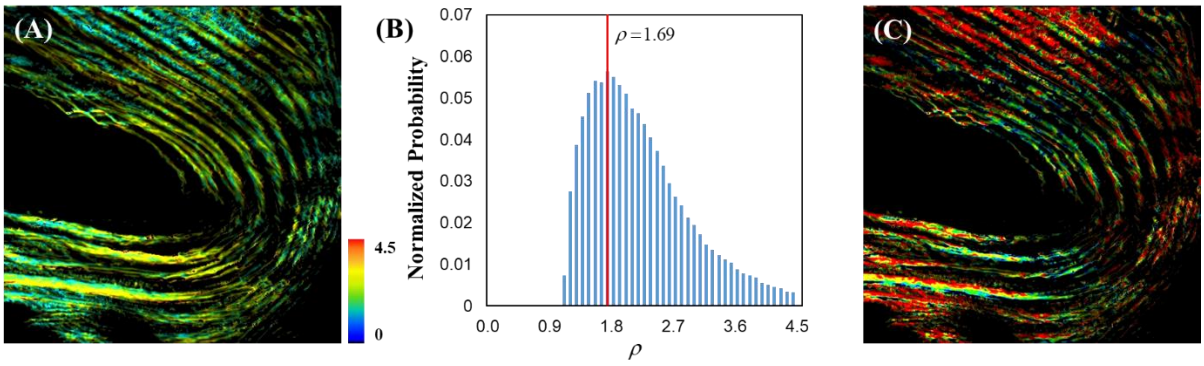

Figure 4-4 Tensor ratio map and polar tilt angle analysis of sectioned mouse tail.

4.5 Conclusion

Second harmonic generation (SHG) from unpolarized fundamental was demonstrated. A theoretical framework bridging Jones and Mueller calculus was developed to describe the polarization dependence SHG with partially or fully depolarized fundamental. Experimental validation was performed with z-cut quartz with fully depolarized incident light. Excellent agreement was observed between the experimental results and theoretical predictions. Despite the use of depolarized fundamental, azimuthal orientation map and local tensor ratio $\chi_{z'z'z'} / \chi_{z'x'x'}$ were successfully recovered for the collagen fibers.

4.6 References

1. Campagnola, P. J.; Loew, L. M., Second-harmonic imaging microscopy for visualizing biomolecular arrays in cells, tissues and organisms. *Nature Biotechnology* **2003,** *21* (11), 1356-1360.

2. Stoller, P.; Reiser, K. M.; Celliers, P. M.; Rubenchik, A. M., Polarization-modulated second harmonic generation in collagen. *Biophys J* **2002,** *82* (6), 3330-42.

3. Gusachenko, I.; Tran, V.; Goulam Houssen, Y.; Allain, J. M.; Schanne-Klein, M. C., Polarization-resolved second-harmonic generation in tendon upon mechanical stretching. *Biophys J* **2012,** *102* (9), 2220-9.

4. Dow, X. Y.; DeWalt, E. L.; Sullivan, S. Z.; Schmitt, P. D.; Ulcickas, J. R.; Simpson, G. J., Imaging the Nonlinear Susceptibility Tensor of Collagen by Nonlinear Optical Stokes Ellipsometry. *Biophys J* **2016,** *111* (7), 1361-1374.

5. DeWalt, E. L.; Sullivan, S. Z.; Schmitt, P. D.; Muir, R. D.; Simpson, G. J., Polarization-modulated second harmonic generation ellipsometric microscopy at video rate. *Anal Chem* **2014,** *86* (16), 8448-56.

6. Schmitt, P. D.; DeWalt, E. L.; Dow, X. Y.; Simpson, G. J., Rapid Discrimination of Polymorphic Crystal Forms by Nonlinear Optical Stokes Ellipsometric Microscopy. *Anal Chem* **2016,** *88* (11), 5760-5768.

7. Petralli-Mallow, T.; Wong, T. M.; Byers, J. D.; Yee, H. I., Circular dichroism spectroscopy at interfaces: a surface second harmonic generation study. *Journal of physical …* **1993**.

8. Tiaho, F.; Recher, G.; Rouede, D., Estimation of helical angles of myosin and collagen by second harmonic generation imaging microscopy. *Optics express* **2007**.

9. Amat-Roldan, I.; Psilodimitrakopoulos, S., Fast image analysis in polarization SHG microscopy. *Optics …* **2010**.

10. Nadiarnykh, O.; Campagnola, P. J., Retention of polarization signatures in SHG microscopy of scattering tissues through optical clearing. *Optics express* **2009**.

11. Gusachenko, I.; Latour, G.; Schanne-Klein, M. C., Polarization-resolved Second Harmonic microscopy in anisotropic thick tissues. *Opt Express* **2010,** *18* (18), 19339-52.

12. Samim, M.; Krouglov, S.; Barzda, V., Nonlinear Stokes-Mueller polarimetry. *Physical Review A* **2016**.

13. Shi, Y. M.; Mcclain, W. M.; Harris, R. A., An Extension of the Mueller Scattering Matrix to Nonlinear Light-Scattering. *Chem Phys Lett* **1993,** *205* (1), 91-95.

14. Shi, Y. M.; Mcclain, W. M.; Harris, R. A., Generalized Stokes-Mueller Formalism for 2-Photon Absorption, Frequency-Doubling, and Hyper-Raman Scattering. *Phys Rev A* **1994,** *49* (3), 1999-2015.

15. Kontenis, L.; Samim, M.; Karunendiran, A.; Krouglov, S.; Stewart, B.; Barzda, V., Second harmonic generation double Stokes Mueller polarimetric microscopy of myofilaments. *Biomedical optics express* **2016,** *7* (2), 559-569.

16. Simpson, G. J., Connection of Jones and Mueller Tensors in Second Harmonic Generation and Multi-Photon Fluorescence Measurements. *J Phys Chem B* **2016,** *120* (13), 3281-302.

17. Azzam, R. M. A.; Bashara, N. M., *Ellipsometry and Polarized Light*. Elsevier: Amsterdam, 1987.

18. Burke, M.; Golaraei, A.; Atkins, A.; Akens, M.; Barzda, V.; Whyne, C., Collagen fibril organization within rat vertebral bone modified with metastatic involvement. *J Struct Biol* **2017,** *199* (2), 153-164.

19. Schneider, C. A.; Rasband, W. S.; Eliceiri, K. W., NIH Image to ImageJ: 25 years of image analysis. *Nat Methods* **2012,** *9* (7), 671-5.

20. Puspoki, Z.; Storath, M.; Sage, D.; Unser, M., Transforms and Operators for Directional Bioimage Analysis: A Survey. *Adv Anat Embryol Cell Biol* **2016,** *219*, 69-93.

21. Chen, W.; Li, T.; Su, P.; Chou, C.; Fwu, P. T.; Lin, S.; Kim, D.; So, P. T. C.; Dong, C., Second harmonic generation χ tensor microscopy for tissue imaging. *Applied Physics Letters* **2009,** *94* (18), 183902.

22. Moad, A. J.; Simpson, G. J., A Unified Treatment of Selection Rules and Symmetry Relations for Sum-Frequency and Second Harmonic Spectroscopies. *The Journal of Physical Chemistry B* **2004,** *108* (11), 3548-3562.

CHAPTER 5. SPATIOTEMPORAL POLARIZATION MODULATION MICROSCOPY WITH A MICRORETARDER ARRAY

5.1 Introduction

As mentioned in the previous chapters, polarization dependent SHG (PD-SHG) microscopy provides rich information on biological tissues and crystalline materials. Currently, the most common approaches for PD-SHG are based on mechanical rotation of waveplates and polarizers, which significantly limits the images acquisition rate. This not only limits the PD-SHG microscopy for high throughput API screening and *in vivo* imaging, but also introduces 1/f noise into the measurements. In order to overcome these limitations, several groups have implemented electro-optic modulator (EOM) for fast polarization modulation. In our previous research,[1] we have described an EOM based PD-SHG microscope with 8 MHz polarization modulation and acquired PD-SHG images at 17 frames per second. Despite of the speed advantages of EOM based PD-SHG, several additional electronics may be required such as RF amplifiers and arbitrary wave generator. Placing a high frequency EOM into an existing SHG microscope can be challenging for compact systems such as a commercial beam-scanning systems for automated SHG and two-photon excited ultraviolet fluorescence (TPE-UVF) imaging of 96-well plates (Formulatrix), or a custom system integrating SHG and TPE-UVF microscopy into a synchrotron XRD beamline (Argonne National Laboratory).[2] Inspired by the design of the microretarder array based depolarizer described in Chapter 4, we developed a fast, simple strategy to acquire PD-SHG images with an addition of a single thin 1-inch optic for a commercial beam-scanning system. The state of polarization was modulated passively by a polarization dependent mask in the rear conjugate plane. Proof-of-concept images were acquired with z-cut quartz and sectioned mouse tail. Good agreement was observed between experimental measurements and theoretical predictions.

5.2 Methods

A patterned micro retarder array was placed in the rear conjugate plane of a beam-scanning microscope described in the previous chapter. The microretarder elements are designed to have half wave retardance for 800 nm fundamental. The angle of the fast axis varies sinusoidally in one

dimension and remains constant in the orthogonal dimension. The spatially varying microretarder elements generated a spatially varying polarization state while beam scanning and the wave front is duplicated in the sample plane (demonstrated in Figure 5-1 and Figure 5-2). The transmittance of the fundamental and SHG signals were collected with an objective and separated by a dichroic mirror. Precise polarization state of the incident light at every pixel in the FoV was fitted based on the laser transmittance image with a detection polarizer. Therefore, PD-SHG information for a single particle in the FoV can be recovered based on the intensity modulation across the sample.

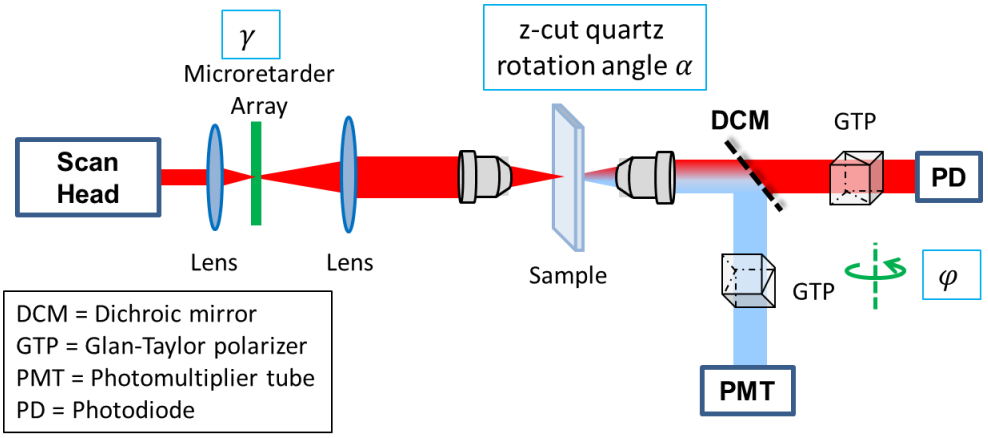

Figure 5-1 Instrument schematic of spatiotemporal polarization modulation microscopy.

5.3 Results and Discussion

To evaluate the performance of the instrument, z-cut quartz placed at an arbitrary angle was first imaged, as it has well-defined PD-SHG properties. A series of PD-SHG images were acquired as a function of sample's azimuthal rotation (α). To demonstrate the effect of polarization rotation, the intensities of the laser transmittance (Figure 5-2, top) and SHG signal (Figure 5-2, bottom) were integrated along the resonant mirror axis and rearranged as a function of α rotation angle since the polarization modulation is along the galvo mirror axis. The pattern of intensity modulation remained constant for the laser transmittance with α due to the absence of birefringence for z-cut quartz. In contrast, the SHG modulation shifted as a function of α as the tensor elements in the laboratory frame were rotated.

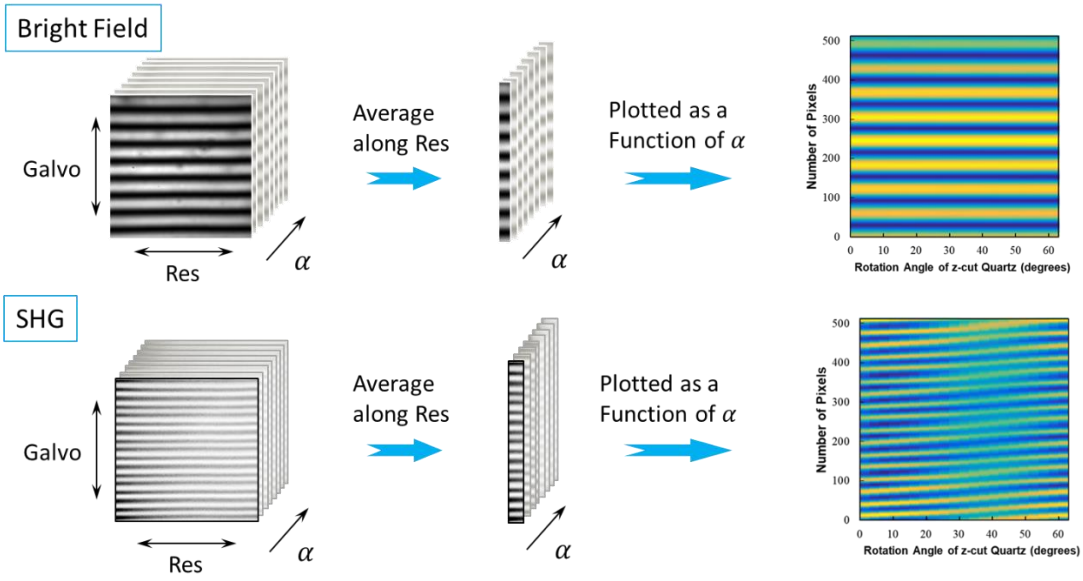

Figure 5-2 Polarization modulation for laser transmittance (top) and SHG (bottom) signal.

To recover the NLO properties from z-cut quartz, the intensity of the detected SHG signal was fitted to an analytical model described in Eq. (4.19). [3-4]

$$
\begin{aligned}
&I_{L,n}^{2\omega}(\gamma) = A\cdot\cos^4\gamma + B\cdot\cos^3\gamma\cdot\sin\gamma + C\cdot\cos^2\gamma\cdot\sin^2\gamma + D\cdot\cos\gamma\cdot\sin^3\gamma + E\cdot\sin^4\gamma \\
&A = \left|\chi_{nHH}^{(2)}\right|^2 \\
&B = 4\cdot\mathrm{Re}\left(\chi_{nHH}^{(2)*}\cdot\chi_{nHV}^{(2)}\right) \\
&C = 4\cdot\left|\chi_{nHV}^{(2)}\right|^2 + 2\cdot\mathrm{Re}\left(\chi_{nHH}^{(2)*}\cdot\chi_{nVV}^{(2)}\right) \\
&D = 4\cdot\mathrm{Re}\left(\chi_{nVV}^{(2)*}\cdot\chi_{nHV}^{(2)}\right) \\
&E = \left|\chi_{nVV}^{(2)}\right|^2
\end{aligned}
\tag{4.19}
$$

For z-cut quartz, the nonzero local-frame tensor elements are connected by symmetry through the following equalities: $\chi_{yyy} = -\chi_{yxx} = -\chi_{xyx} = -\chi_{xxy}$. By connecting the local frame to the laboratory frame through rotation matrices, a simplified analytical expression can be used to predict the polynomial coefficient in Eq. (4.19) as a function of quartz rotation.

$$
\begin{aligned}
&A = E = \cos^2(3\alpha) \\
&B = -D = 2\sin(6\alpha) \\
&C = 6\sin^2(3\alpha) - 2
\end{aligned}
\tag{4.20}
$$

To recover the quartz azimuthal angle and tensor element, an iterative nonlinear fit was performed. An initial guess value [1, 1, -1] ($\chi_{nhh}, \chi_{nvh,}, \chi_{nvv,}$ respectively) was first used to retrieve the azimuthal angle. Next, the new set of tensor elements value was calculated by the fitted α. The fitting process continued until the value of α and tensor elements converged. Figure 5-3 shows calculated polynomial coefficients based on the iterative fit (A) and the theoretical prediction (B) based on the known symmetry-dependent equalities.[1] The final recovered tensor elements was [0.9, 1, -1] with an initial $\alpha = 0.37 rad$.

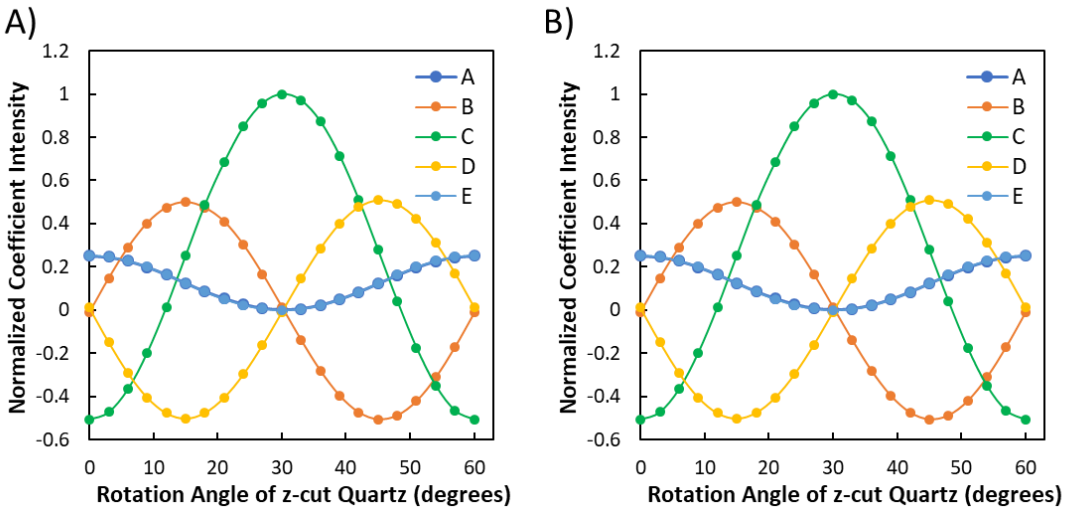

Figure 5-3 Calculated polynomial coefficients (A) with theoretical prediction (B).

A spatially heterogeneity collagenous tissue sample was then imaged with the spatiotemporal polarization modulation microscope. The laser transmittance and the SHG images detected for horizonal polarization state are shown in Figure 5-4 (A) and (B). To recover the $\rho\left(\chi_{z'z'z'} / \chi_{z'x'x'}\right)$, the orientation of the collagen fibers was first determined by *OrientationJ* based on the image analysis. The collective set of collagen tensor elements was then recovered with reference frame rotation between the local and laboratory frames as detailed in previous work.[3] Figure 5-4 (C) shows the calculated SHG intensity based on the fitted ρ and fiber rotation angle. Good agreement

was observed between Figure 5-4 (B) and (C). The recovered ρ for this particular FoV is 1.44 ± 0.08, which agrees reasonable well with previous report.[5-7]

It is worth noting that the pooled analysis for collagenous sample implicitly assumed identical local-frame tensor elements for collagen. Previous studies have showed the significant variation in the tensors for different regions or types of collagen. The true local tensor for each single pixel can be in principle recovered by taking multiple snapshot images while translating the sample stage.

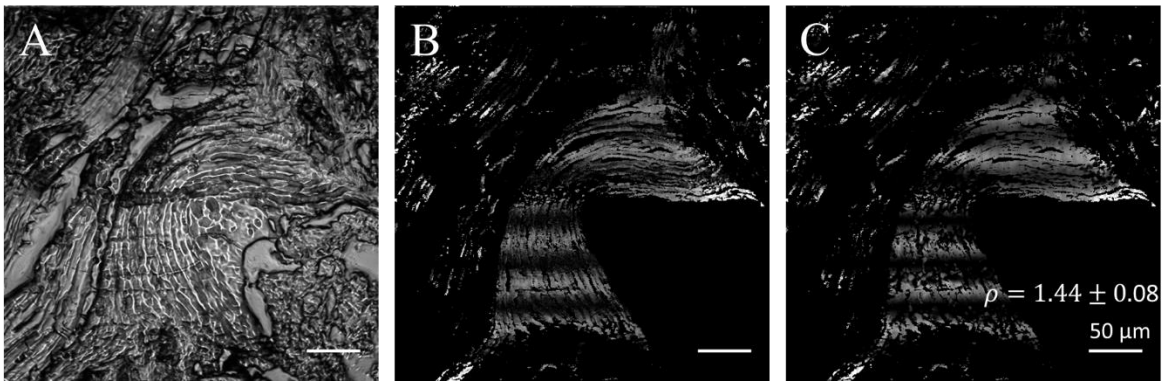

Figure 5-4 Polarization dependent measurements of collagenous tissue sample.

5.4 Conclusion

A novel polarization modulation NLO microscopy was demonstrated with a microretarder array. Excellent agreement between experimental measurements and theoretical predictions was observed for spatially uniform z-cut quartz. Pooled analysis of collagen fibers within the entire FoV was performed with a collagenous tissue sample. Compared to a EOM based PD-SHG microscope, the microretarder array can be easily install in an integrated NLO microscope such as an automated SHG and two-photon excited ultraviolet fluorescence (TPE-UVF) imaging of 96-well plates (Formulatrix) and SHG-guided XRD system described in Chapter 2, which enables fast polymorph discrimination for APIs and multi-domain crystals rejection prior to diffraction measurements.

5.5 References

1. DeWalt, E. L.; Sullivan, S. Z.; Schmitt, P. D.; Muir, R. D.; Simpson, G. J., Polarization-modulated second harmonic generation ellipsometric microscopy at video rate. *Anal Chem* **2014,** *86* (16), 8448-56.

2. Newman, J. A.; Zhang, S.; Sullivan, S. Z.; Dow, X. Y.; Becker, M.; Sheedlo, M. J.; Stepanov, S.; Carlsen, M. S.; Everly, R. M.; Das, C., Guiding synchrotron X-ray diffraction by multimodal video-rate protein crystal imaging. *Journal of synchrotron radiation* **2016,** *23* (4), 959-965.

3. Simpson, G. J., *Nonlinear Optical Polarization Analysis in Chemistry and Biology*. Camgridge Molecular Science: 2017.

4. Dow, X. Y.; DeWalt, E. L.; Newman, J. A.; Dettmar, C. M.; Simpson, G. J., Unified Theory for Polarization Analysis in Second Harmonic and Sum Frequency Microscopy. *Biophysical Journal* **2016,** *111* (7), 1553-1568.

5. Tuer, A. E.; Krouglov, S.; Prent, N.; Cisek, R.; Sandkuijl, D.; Yasufuku, K.; Wilson, B. C.; Barzda, V., Nonlinear optical properties of type I collagen fibers studied by polarization dependent second harmonic generation microscopy. *The Journal of Physical Chemistry B* **2011,** *115* (44), 12759-12769.

6. Hovhannisyan, V. A.; Su, P.-J.; Lin, S.-J.; Dong, C.-Y., Quantifying thermodynamics of collagen thermal denaturation by second harmonic generation imaging. *Applied Physics Letters* **2009,** *94* (23), 233902.

7. Tiaho, F.; Recher, G.; Rouede, D., Estimation of helical angles of myosin and collagen by second harmonic generation imaging microscopy. *Optics express* **2007,** *15* (19), 12286-12295.

CHAPTER 6. SPATIAL-SPECTRAL MULTIPLEXING FOR HYPERSPECTRAL MULTIPHOTON FLUORESCENCE IMAGING

6.1 Introduction

Fluorescence hyperspectral imaging is a powerful tool for biological studies as it provides an additional dimension of information compared to filter based multispectral fluorescence microscopes.[1-2] The expansion in the spectral domain enables accurate classification and quantitative analysis of multiple spectrally overlapping components in biological structures for studying complex biological processes [3-4] and clinical diagnoses.[5-6] In order to achieve hyperspectral imaging, a 3 dimensional (3D) data structure (x, y, λ) is typically populated. Traditional hyperspectral imaging techniques typically rely on spatial scanning[7-8] or spectral scanning.[9-10] Spatial scanning interrogates the emission profile (λ) of a single pixel or line scanned across the field of view (FoV) to construct the 3D data cube. Conversely, spectral scanning methods image the entire FoV (x, y) on a 2D area detector and probe a single wavelength (λ) at a time. The speed of acquisition is typically limited by the mechanical movement of the dispersive optics and integration time for the detector array, which also introduces 1/f noise into the measurement. Capturing inherent dynamics of living systems such as Ca^{2+} oscillations associated with neuron firing typically requires a frame rate at around 20 Hz.[11-12] Furthermore, significant motion blur from cardiovascular motion degrades resolution for *in vivo* imaging.[13] The bandwidth of current computer I/O interfaces also bottlenecks the achievable frame rate for uncompressed hyperspectral imaging. For a system with 2000 fluorescence channels, 16 bits per channel, 512 × 512 images at 20 frames per second (fps) speed, the overall data throughput is about 20.97 GB/s compared to the theoretical limit of a modern PCI-E 3.0 × 16 interface at 15.76 GB/s. The write speed of a commercially available storage device is typically less than a few gigabytes per second, representing a practical limit on data throughput.

Recently, several snapshot hyperspectral imaging systems were developed to improve the image acquisition speed while still maintaining reasonable data throughput rates.[14-17] Coded aperture snapshot spectral imager (CASSI) directly images the projection of a rotated data cube and reconstructs the hyperspectral images using sparse sampling algorithm.[16] Image mapping spectrometers (IMS) spatially offsets the data cube layer by layer and projects them onto a large area detector.[17-18] Both of these methods provide innovative strategies to overcome the scanning

mechanism and bandwidth limitation. However, most of the existing snapshot methods are not directly compatible with multi-photon excited fluorescence microscopy, which significantly increases the depth of penetration for *in vivo* imaging. Furthermore, images captured using focal plane array detectors generally introduce trade-offs between spatial and spectral resolution, as both sets of information must be encoded on the same fixed number of imaging channels.

In this work, we demonstrated an experimentally simple approach to achieve video-rate hyperspectral imaging for two-photon excited fluorescence (TPEF) through non-de-scanned spatial/spectral multiplexing (NDSSM) without degraded the spatial resolution. A 16-channel photomultiplier tube (PMT) array (Hamamatsu, H12311-40) was used as spatial-spectral multiplexing detector with fast single photon response time (ns), and paired with a 16-channel digital oscilloscope card (AlazarTech, ATS9416) for fast data digitization. Spatial-spectral multiplexing was achieved by performing non-de-scan detection, such that the spectra illuminated onto the PMT array varied as a function of beam's scan position. Demultiplexing allowed recovery of spectra with over 2000 fluorescence channels at video rate (17 fps for frame size of 512 × 512 pixels). The data throughput for the 16-channel digital oscilloscope was compressed at 2.24 GB/s with the multiplexing, as opposed to 336 GB/s without compression.

It is interesting to consider the potential change in spatial resolution resulting from the spatial/spectral multiplexing. In CASSI measurements, multiplexing to recover spectral information necessarily comes at the expense of spatial resolution, since the same fixed number of pixels now reports on combined spatial and spectral information. In contrast, all the spectral information in NDSSM is contained in the orthogonal spectral axis accessed by the excitation positions in the PMT array, such that hyperspectral images can be acquired without sacrifices in spatial resolution or image quality.

6.2 Methods

6.2.1 Instrumentation

The hyperspectral imaging system is depicted in (Figure 6-1 (A)). In brief, a tunable 80 MHz Ti:sapphire femtosecond laser (Spectra-Physics, Mai Tai) was used for excitation. The beam was scanned across the sample using a resonant scanning mirror at 8.8 kHz (EOPC) for the fast-scan axis and a galvanometer mirror (Cambridge-Tech) for the slow-scan. A square aperture was placed

in the rear conjugate plane to cut off the turning point of the resonant mirror to avoid sample damage. A 10× 0.3 NA objective (Nikon) was used to focus the beam down to the sample with the fluorescence signal collected in the epi direction back through the same objective. The laser was tuned in a range of 800 - 1000 nm for different excitations with powers at the sample around 40 - 100 mW. A dichroic mirror and a band pass filter (Chroma, 350 – 700 nm) were used to isolate the fluorescence signals. A 4f lens pair was used to direct the collimated fluorescence onto the center of a transmission diffraction grating (Wasatch Photonics, WP-600/600-25.4). The spectrally separated beam was then focused on to a 16 channel PMT array (Hamamatsu, H12311-40). The 16 channel PMT array electronics were custom built to improve the single photon response time by two orders of magnitude over the original design. The circuit for each channel consisted of a two-stage high-speed operational amplifier circuit connected directly to the output of each element on the PMT array. The output was AC-coupled into a 50 Ω impedance microstrip through a custom printed circuit board (PCB) trace in order to provide impedance matching to the output transmission line. Responses of the PMT array were digitized synchronously with the laser pulses by using a 16 channel PCI-E digital oscilloscope card and remapped into sixteen 512 × 512 images via custom software (MATLAB).

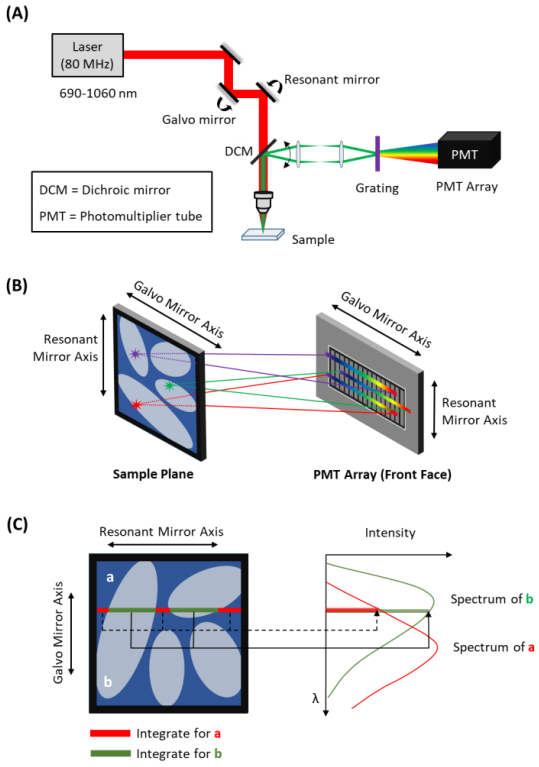

Figure 6-1 Overview of spatial-spectral multiplexing. (A) Instrument schematic. (B) Illustration of spectra projected on the PMT array from different pixels in one image plane. (C) Spectral reconstruction from a single channel image for two components with different spectra.

6.2.2 Sample Preparation

Fluorescein, coumarin 6, sodium dodecyl sulfate, and chloroform were purchased from Sigma-Aldrich, with eFluor™ 450 obtained from Thermo Fisher. All aqueous solutions were prepared with Milli-Q water (18.2 MΩ cm^{-1}). For emulsion mixture with two components, stock solutions of 5 μM fluorescein in water and 50 μM coumarin 6 in chloroform were prepared separately. The two stock solutions were mixed equally in amount with ~1mg of sodium dodecyl sulfate. Then the mixture was shaken by hand to produce a stable emulsion mixture for imaging. For emulsion mixture with three components, stock solutions of fluorescein in water, coumarin 6 in chloroform, and eFluorTM 450 in chloroform were made separately with a concentration of 50 μM for each. Then two two-component emulsion mixtures were prepared separately for eFluor™ 450 / fluorescein and coumarin 6 / fluorescein system based on the procedure above, and the two two-

component emulsion mixtures were mixed in equal parts to produce a three-component emulsion mixture.

For a living sample, genetically modified nematodes (C. elegans) strains were cultured on agar plates seeded with Escherichia coli at 20 °C. For imaging, C. elegans strains were sealed between two glass coverslips immersed in 0.9 % NaCl physiological saline.

6.2.3 Spectral Reconstruction and Component Classification

A spectral retrieval algorithm was developed to analyze the raw data. Since the incident angle of the beam onto the diffraction grating varied during the beam scanning, each set of the 16 images from different channels was correlated spatially and spectrally for the same FoV. For each frame, pixels with the same galvanometer mirror position shared the same spectral projection pattern on the PMT array; while pixels along the galvanometer mirror axis produced unique projections as a function of position (Figure 6-1 (B)). Therefore, spectrum can be generated by integrating all signals from the same fluorophore along the resonant mirror axis while the galvanometer axis contained wavelength information (Figure 6-1 (C)).

For an emission spectrum $s^0(\lambda)$ from one fluorophore (i.e., all locations of identical classification), the detected spectrum from a single PMT channel $s^{meas}(\lambda)$ can be described in Eq.(4.21), in which L is the spectral bandwidth of the PMT channel for a given galvanometer position. The measured spectral intensity $s_j^{meas}(\lambda)$ for a given measurement centered about the wavelength j is limited by L, which is equivalent to the entrance slit size of a spectrometer.

$$s_j^{meas} = \int s_j^0(\lambda) d\lambda \cong \sum_{l=-L/2}^{L/2} s_{j+l}^0 \delta\lambda \tag{4.21}$$

In Eq.(4.21), $\delta\lambda$ corresponds the bandwidth of a single pixel in the final recovered spectrum, which is generally significantly smaller than the bandwidth dictated by the physical dimensions of the PMT L, and s^0_j corresponds to the ground truth spectrum at the position j. Extending this analysis to each pixel in the image and the corresponding center position of the spectrum upon beam-scanning along the x-axis (galvo), the mathematical relationship described by summation in Eq. (4.21)corresponds to convolution of the ground truth spectrum with a rectangle function of width L.

$$\bar{s}^{meas} = \bar{s}^0 \otimes rect\left(L\right) \tag{4.22}$$

Significant signal to noise enhancement in the measured spectrum arises through integration of all the similarly classified locations along the orthogonal *y*-axis (resonant mirror). For a $\delta\lambda$ corresponding to each *x*-axis position in the image, a single detector can produce a spectrum with up to 512 elements for a 512×512 image.

While the single-detector approach described mathematically in Eq. (4.22) can in principle recover a complete spectrum at every position, the use of a PMT array has three critical practical benefits: i) measurements with an array produce detected intensity at each location to aid in spectral classification, ii) multiple array elements allow extension of the spectral dynamic range without requiring large displacements of the galvo-axis mirror, and iii) the higher collection efficiency of light and spectral overlap between channels results in signal to noise improvements. The spectral overlap between channels depended on the beam scanning path shown in Figure 6-2 (A) and the design of the 16-channel PMT array shown in Figure 6-2 (B). Each single PMT channel had a width of 0.8 mm with 0.2 mm gap between channels. For a FoV of 500 μm × 500 μm, 512 × 512 pixels with a 10× objective, a narrow band emission was scanned across three adjacent PMT channels with the size of 2.5 mm × 2.5 mm, inducing ~2/3 overlap between the spectral windows for each PMT channel. For a single PMT channel, the detected narrow band emission had a width around 170 pixels along the galvo axis. In the case of no spectral overlap between adjacent detectors, the combined set of 16 detector could in principle be used to generate a spectrum with 8,192 elements (16 × 512). To minimize edge effects, spectra with 460 spectral channels were used, correspond to a maximum of 7,360 channels. In practice, significant spectral overlap illustrated in Figure 6-2 (C) enables spectral stitching, in which minimization of the squared deviations in the overlapping regions serves to calibrate the relative sensitivity of adjacent detectors. As a result, ~2200 independent spectral channels were recovered after the stitching.

Second harmonic generation (SHG) from a doubling crystal (BBO) was used as the reference as it generated uniformly distributed fluorescence in the FoV with a well-defined narrow band spectrum. By tuning the laser to 800 nm, 900 nm and 1000 nm, three references SHG spectra (centered at 400 nm, 450 nm, and 500 nm) were generated for calibration purposes (*Fig. 2(C)*). As a planar detector was used in the setup, signal projected on the blue and red end on the PMT array had slightly larger spectral separations comparing to the center due to the longer projection length. It was consistent with the observation of 553 data points between 400 / 450 nm peaks and 549 data points between 450 / 500 nm peaks. The average channel density was used for the calibration.

With a 100 mm lens to focus spectral pattern down to the PMT array, the width of the whole spectral window was about 200 nm. In this case, the rectangular function in Eq. (4.22) had a width corresponding to 15 nm (170 pixels), which limited the operational spectral resolution. The full width half maximum of the reconstructed SHG peak was 10 nm, compared to 2.5 nm for the excitation source measured by a spectrometer (Thorlabs, CCS175).

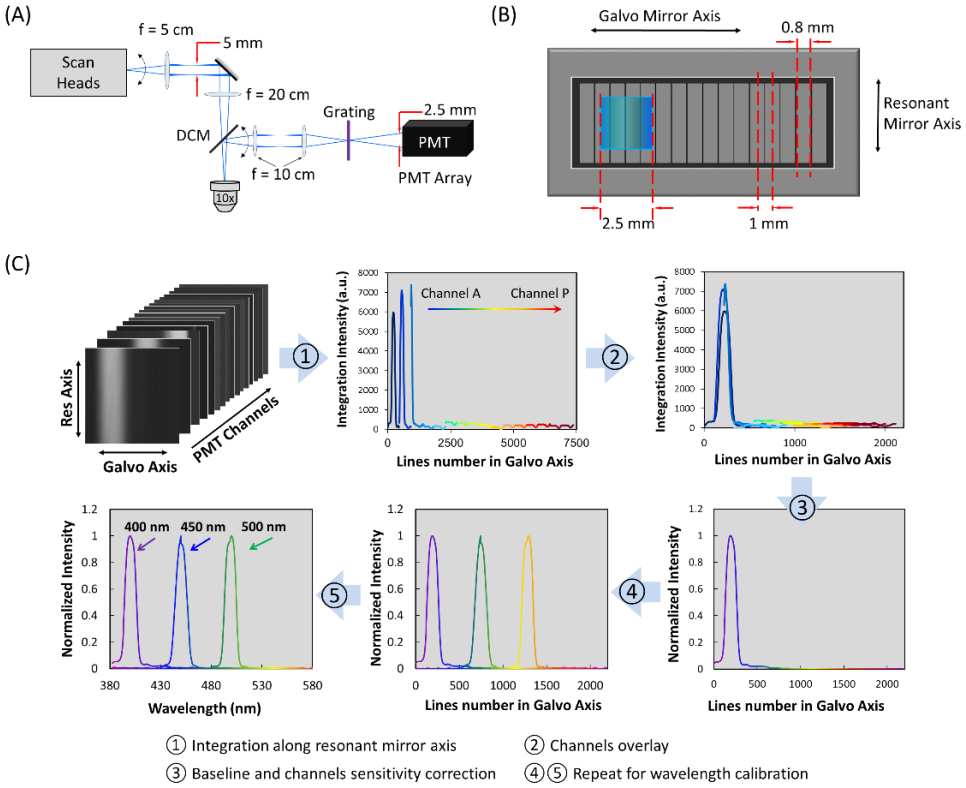

Figure 6-2 (A) Beam scanning path (not the beam path). (B) The projection of spectrum of a narrow band emission on the PMT array. (C) Spectral window calibration with doubling crystal.

The preceding analysis describes the approach taken to recover spectra from pooled measurements of locations with identical composition. A flow chart of the algorithm is shown in Figure 6-3. In brief, a threshold was first set to identify signal pixels from the background. Next, a simple Euclidean angle (Eq.(4.23)) method was used for fluorescence spectra classification.[19]

$$\cos(\theta) = \frac{\vec{s}_{ref} \cdot \vec{s}_{x,y}}{\left|\vec{s}_{ref}\right| \cdot \left|\vec{s}_{x,y}\right|} \tag{4.23}$$

Pixels ($\vec{s}_{x,y}$) with large Euclidean angles relative to the *n* known reference spectra ($\vec{s}_{ref}$) (i.e., $\cos(\theta) < 0.99$) were collectively classified as an "other" component. As a result, discrete masks for each of the $n+1$ components were generated. Spectra of all the components were then extracted based on the new discrete classification masks. To initiate this process, an initial guess spectrum was generated based on intensities from all signal pixels. This process was iterated until 99% of the pixels in the FoV were classified as the same component with the previous iteration. Following classification, spectral recovery for each class was performed as described in the preceding paragraph, with the process iteratively performed until convergence was achieved in both the spectra recovered and the spatial classifications. For data acquired at video-rate, the number of components and their spectra recovered from the first frame was used as the reference for the rest of the frames to reduce the spectral data analysis time. The computation time was dependent on the initial guess and the assumed number of components. For a two-component system, processing a single frame took about 20 to 50 seconds on a 4th generation hexa-core Intel® Core™ i7 processor running in MATLAB. In order to initiate the iterative process, an initial guess spectrum was produced from the ensemble average of all pixels containing signal in the entire FoV, which served as the initial reference spectrum for a preliminary binary classification.

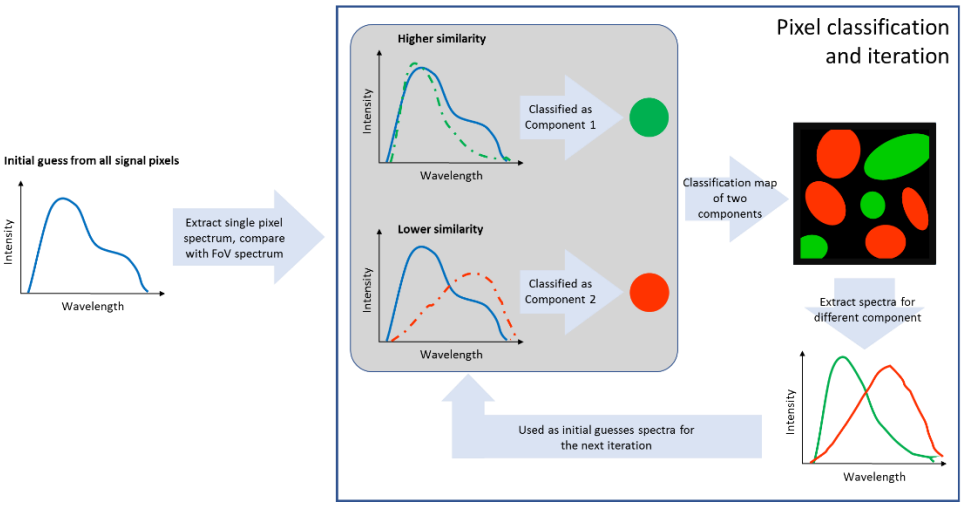

Figure 6-3 Flowchart for the iterative classification algorithm.

6.3 Results and Discussion

6.3.1 Heterogeneous Mixtures of Fluorescent Dye Droplets

A fluorescein/coumarin 6 fluorescent dye mixture was used to assess the spectral imaging of the system and the accuracy of the classification algorithm. Figure 6-4(A) showed a TPEF image from the integrated intensity of all 16 channels for this suspension under 800 nm excitation. A two-component classification image produced the images in Figure 6-4(B), with one component labeled in green (component *a*) and another in blue (component *b*). It is worth noting that the recovered spectra of the two components were highly overlapping (*Fig. 4(B)* insert), making them difficult to confidently discriminate using a filter-based fluorescence microscope. The recovered spectra of this hyperspectral imaging system were overlaid with independent measurements from a benchtop fluorimeter (FLS1000, Edinburgh Instruments) with 400 nm excitation (Figures 6-4(D) and 4(E)). All spectra were normalized to the maximum intensity. The good agreement between the recovered spectra and the fluorimeter measurements was consistent with component *a* composed primarily of fluorescein in water and component *b* primarily coumarin 6 in chloroform, which also agreed with their anticipated respective solubility in water and chloroform. While the fluorescence emission spectra acquired by statistical decomposition were in good qualitative agreement with those obtained from independent measurements with a fluorimeter using pristine solutions, statistically significant deviations were present for both coumarin and fluorescein. In

particular, the measurements obtained in the water/chloroform suspensions exhibited broader peaks than those interrogated in pure solutions. The increase in width for the suspensions is attributed to a combination of two effects; i) convolution of the emission spectrum with a rectangle function (vide supra) results in spectral broadening, and ii) the inhomogeneity of the environment in the water/chloroform suspension results in additional inhomogeneous broadening. From the measured SHG response, the contributions from convolution are insufficient to account for the observed differences in peak shapes. Therefore, the primary origin of the deviations observed between the emission spectra in Figures 6-4 (D) and (E) are attributed to spectral broadening associated with inhomogeneities from the greater diversity of environments available for partitioning (e.g., coumarin partitioning into the aqueous phase, fluorescence into chloroform, and both to the surfactant-stabilized interfaces). To study the fluorophores' distributions at the water-chloroform interface, analysis was repeated assuming a maximum number of three components. Under this case, the boundary of the chloroform droplets was identified as a third component (red in Figure 6-4 (C)). The recovered spectrum for the third components (component *c*) was shown in Figure 6-4 (F). The spectrum of component *c* (red dot line) was fitted as a linear combination of component *a* and component *b* as shown in solid line in Figure 6-4 (F) with $R^2 = 0.99$. Based on this fitting, component *a* (fluorescein in water) was weighted at 60.6% in the boundary between water and chloroform and component *b* (coumarin 6 in chloroform) was weighted at 39.1%. This method could provide new strategies for the study of surface interaction between different solvent.

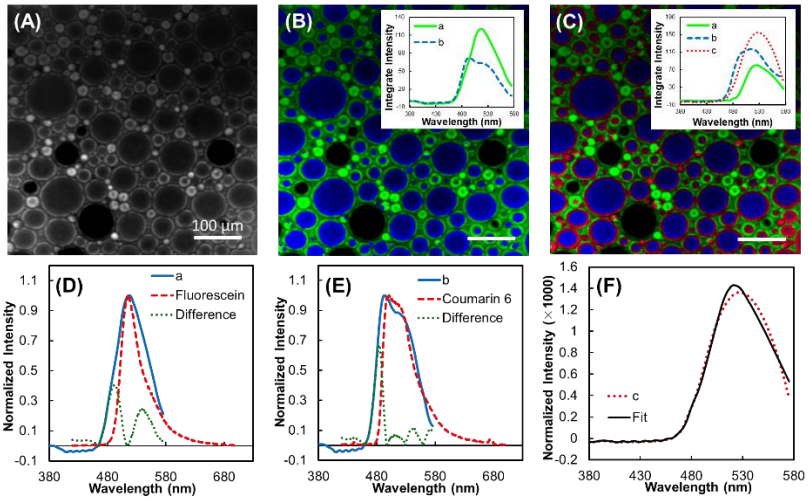

Figure 6-4 (A) Integrated total fluorescence of a dye mixture (5µM fluorescein in water and 50 µM coumarin 6 in chloroform). (B) Classification under the assumption of two components (a in green and b in blue). Insert: recovered spectra of component a and b. (C) Classification under the assumption of three components (a in green, b in blue and c in red). Insert: recovered spectra for component a, b and c. (D) Overlay of recovered spectrum of component a with the fluorescein emission spectrum from a benchtop fluorimeter, and the difference between them. (E) Overlay of recovered spectrum of component b with the coumarin 6 emission spectrum, and the difference between them. Both plotted spectra were averaged over all the spatial positions of the same classified component. (F) Spectrum of the third component (red dotted line) fitted as a linear combination (black solid line) of the first two components.

In Figure 6-5, hyperspectral TPEF is demonstrated for measurements of fluorescence photobleaching, highlighting the advantages of high speed hyperspectral microscopy in the analysis of dynamic multicomponent mixtures. The three-component emulsions system of eFluor™ 450 (chloroform)/coumarin 6 (chloroform)/fluorescein (water) was used for this purpose. A video with both classification images and spectra can be found in the Supplementary Materials (**Visualization 1**). Figure 6-5 (A) shows a single frame (frame number 55) from the video (green for fluorescein, blue for coumarin 6 and violet for eFluor™ 450). A target coumarin 6 droplet was circled in red for tracking the dynamic behavior. This frame was set as the start of the dynamic analysis (0 s), which corresponded to 3.2 s in the video. After 21.8 s, most of the coumarin 6 fluorescence was lost from photobleaching. Following the removal of the coumarin 6 signal, the classification of the target droplet was reclassified to 'eFluor™ 450' by the classification algorithm (circled in Figure 6-5 (B)). The total number of excitations driving photobleaching was plotted

Figure 6-5 (D). In brief, the single-photon peak height distribution of the PMT was measured through a histogram analysis of a time-trace. The mean voltage per photon provided a point of calibration to convert the voltages acquired during imaging to absolute mean numbers of photons. The total number of emitted fluorescence photons for an isotropic emission was calculated based on the solid angle of collection through the objective. Previously measured values for the quantum efficiency of fluorescence for coumarin 6[20] allowed conversion from the total number of emitted photons to the total number of excitations per unit time. The plot of total number of excitations was then fit to an exponential decay with a time constant of 5.16 ± 0.08 s, consistent with an exponential process routinely observed in photobleaching.[21]

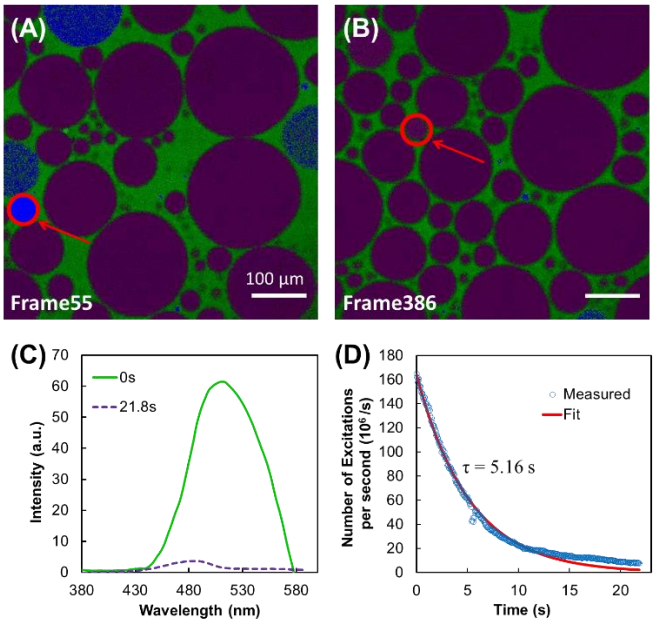

Figure 6-5 Dye mixture with three fluorophores: fluorescein (green) in water, coumarin 6 (blue) and eFluorTM 450 (violet) in chloroform separately. Target droplet with coumarin 6 in chloroform (circled in red) was tracked from its first appearance in frame 55, set as 0 s (A) and final misclassification in frame 386 with during time 21.8 s (B). (C) Spectra recovered from the target droplet at 0 s (green solid line) and 21.8 s (purple dash line). (D) Photobleaching curve of coumarin 6 in the target droplet (blue dot) with the exponential fit (red line).

6.3.2 *In vivo* Imaging of Genetically Modified *C. elegans*

Genetically modified nematodes (*C. elegans*) were used as a living biological sample for the demonstration of fast hyperspectral imaging. *C. elegans* strains were obtained from the Caenorhabditis Genetics Center. The main phenotypes of this *C. elegans* variant are: green fluorescence in the body wall muscle nuclei (*ccIs4251*, green fluorescence protein (GFP)), green fluorescence in the pharyngeal muscle (*mIs12*, GFP), dumpy (*dpy-17*), red fluorescence in the epidermis (*frIs7*, DsRed), and red fluorescence in pharyngeal muscle (*uIs69*, mCherry). A video was acquired for the *C. elegans* with 17 fps, 512 × 512 pixels and 800 nm excitation. Since only GFP and DsRed could be accessed by TPEF with 800 nm excitation, a two-component classification was shown in the video and Figures 6-6 (A) and (B). The two components were labeled in red and green separately with the recovered spectra shown in Figure 6-6 (C). In order to assure the accuracy of this microscopy and classification algorithm, a fluorescence image from a conventional fluorescence microscope (Olympus BX-51) was acquired for the same type of *C. elegans* with an excitation filter at 460 - 490 nm, as shown in Figure 6-6 (D). A similar distribution of the two structures with different fluorescence properties was observed, in which the outside epidermis of the *C. elegans* was red and the pharyngeal muscle in the head was green. In addition, the green fluorescence from the body wall muscle nuclei (*ccIs4251*) could also be seen in images acquired from our instrument. Compared to one photon excited fluorescence in Figure 6-6 (D), significantly less out of plane fluorescence was observed with the TPEF. Detailed biological structures could be seen along with the spectra for each component. Component 1 and component 2 were identified to be predominantly GFP and DsRed, respectively. An injury was induced in the mitotic region of the *C. elegans*. Consistent with surface infection, injury, or osmotic stress, [22-23] green fluorescence due to *frIs7* mutation was preferentially enhanced at the site of injury.

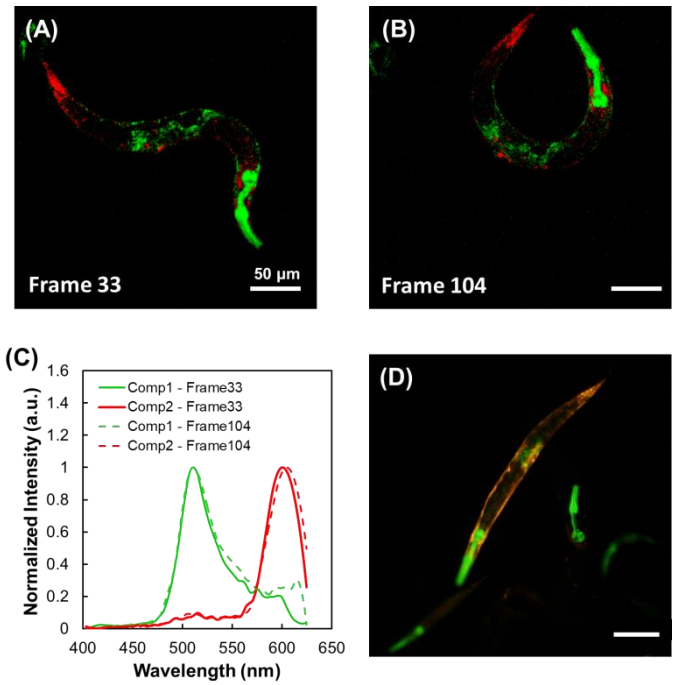

Figure 6-6 Two-photon fluorescence image of gene coded C. elegans analyzed without knowing the emission spectra of the fluorophores as a priori at (A) frame 33 and (B) frame 104. Pseudo-color based on different components recovered from custom classification algorithm with green for component 1 and red for component 2. (C) Recovered spectra for component 1 (green) and 2 (red) for both frame 33 (solid lines) and frame 104 (dash lines). Both plotted spectra were averaged over all the spatial positions of the same classified component. (D) Fluorescence image of gene coded C. elegans with conventional fluorescence microscope under 460 - 490 nm excitation.

6.4 Conclusion

A spatial-spectral multiplexing hyperspectral two-photon fluorescence microscope was developed with over 2000 effective spectral channels in a 200 nm wavelength window and an imaging acquisition rate up to 17 fps. Iterative demultiplexing enabled classification and full recovery of emission spectra with no prior knowledge of the sample. Good agreement was observed between the recovered spectra and those obtained independently using a commercial fluorimeter. The large number of spectral channels of this system made it possible to distinguish fluorophores with similar emission spectra. The high imaging speed made it possible to study highly dynamic multicomponent systems and live biological samples. This instrument is directly compatible with numerous conventional beam-scanning microscope platforms upon addition of a diffraction grating and a multi-channel detector array.

6.5 References

1. Gao, L.; Smith, R. T., Optical hyperspectral imaging in microscopy and spectroscopy - a review of data acquisition. *J Biophotonics* **2015,** *8* (6), 441-56.

2. Cutrale, F.; Trivedi, V.; Trinh, L. A.; Chiu, C. L.; Choi, J. M.; Artiga, M. S.; Fraser, S. E., Hyperspectral phasor analysis enables multi-plexed 5D in vivo imaging. *Nature Methods* **2017,** *14* (2), 149-152.

3. Lansford, R.; Bearman, G.; Fraser, S. E., Resolution of multiple green fluorescent protein color variants and dyes using two-photon microscopy and imaging spectroscopy. *J Biomed Opt* **2001,** *6* (3), 311-8.

4. Bertani, F. R.; Botti, E.; Ferrari, L.; Mussi, V.; Costanzo, A.; D'Alessandro, M.; Cilloco, F.; Selci, S., Label-free and non-invasive discrimination of HaCaT and melanoma cells in a co-culture model by hyperspectral confocal reflectance microscopy. *J Biophotonics* **2016,** *9* (6), 619-25.

5. Arrigoni, S.; Turra, G.; Signoroni, A., Hyperspectral image analysis for rapid and accurate discrimination of bacterial infections: A benchmark study. *Comput Biol Med* **2017,** *88*, 60-71.

6. Rink, C. L.; Wernke, M. M.; Powell, H. M.; Tornero, M.; Gnyawali, S. C.; Schroeder, R. M.; Kim, J. Y.; Denune, J. A.; Albury, A. W.; Gordillo, G. M.; Colvin, J. M.; Sen, C. K., Standardized Approach to Quantitatively Measure Residual Limb Skin Health in Individuals with Lower Limb Amputation. *Adv Wound Care (New Rochelle)* **2017,** *6* (7), 225-232.

7. Sinclair, M. B.; Haaland, D. M.; Timlin, J. A.; Jones, H. D., Hyperspectral confocal microscope. *Appl Opt* **2006,** *45* (24), 6283-91.

8. Luthman, A. S.; Dumitru, S.; Quiros-Gonzalez, I.; Joseph, J.; Bohndiek, S. E., Fluorescence hyperspectral imaging (fHSI) using a spectrally resolved detector array. *Journal of Biophotonics* **2017,** *10* (6-7), 840-853.

9. Morris, H. R.; Hoyt, C. C.; Treado, P. J., Imaging Spectrometers for Fluorescence and Raman Microscopy - Acoustooptic and Liquid-Crystal Tunable Filters. *Appl Spectrosc* **1994,** *48* (7), 857-866.

10. Kasili, P. M.; Vo-Dinh, T., Hyperspectral imaging system using acousto-optic tunable filter for flow cytometry applications. *Cytom Part A* **2006,** *69a* (8), 835-841.

11. Nobauer, T.; Skocek, O.; Pernia-Andrade, A. J.; Weilguny, L.; Traub, F. M.; Molodtsov, M. I.; Vaziri, A., Video rate volumetric Ca2+ imaging across cortex using seeded iterative demixing (SID) microscopy. *Nat Methods* **2017,** *14* (8), 811-818.

12. Prevedel, R.; Yoon, Y. G.; Hoffmann, M.; Pak, N.; Wetzstein, G.; Kato, S.; Schrodel, T.; Raskar, R.; Zimmer, M.; Boyden, E. S.; Vaziri, A., Simultaneous whole-animal 3D imaging of neuronal activity using light-field microscopy. *Nat Methods* **2014,** *11* (7), 727-730.

13. Sullivan, S. Z.; Muir, R. D.; Newman, J. A.; Carlsen, M. S.; Sreehari, S.; Doerge, C.; Begue, N. J.; Everly, R. M.; Bouman, C. A.; Simpson, G. J., High frame-rate multichannel beam-scanning microscopy based on Lissajous trajectories. *Opt Express* **2014,** *22* (20), 24224-34.

14. Dwight, J. G.; Tkaczyk, T. S., Lenslet array tunable snapshot imaging spectrometer (LATIS) for hyperspectral fluorescence microscopy. *Biomed Opt Express* **2017,** *8* (3), 1950-1964.

15. Elliott, A. D.; Gao, L.; Ustione, A.; Bedard, N.; Kester, R.; Piston, D. W.; Tkaczyk, T. S., Real-time hyperspectral fluorescence imaging of pancreatic beta-cell dynamics with the image mapping spectrometer. *J Cell Sci* **2012,** *125* (Pt 20), 4833-40.

16. Cull, C. F.; Choi, K.; Brady, D. J.; Oliver, T., Identification of fluorescent beads using a coded aperture snapshot spectral imager. *Appl Opt* **2010,** *49* (10), B59-70.

17. Gao, L.; Kester, R. T.; Hagen, N.; Tkaczyk, T. S., Snapshot Image Mapping Spectrometer (IMS) with high sampling density for hyperspectral microscopy. *Opt Express* **2010,** *18* (14), 14330-44.

18. Gao, L.; Wang, L. H. V., A review of snapshot multidimensional optical imaging: Measuring photon tags in parallel. *Phys Rep* **2016,** *616*, 1-37.

19. Garini, Y.; Gil, A.; Bar-Am, I.; Cabib, D.; Katzir, N., Signal to noise analysis of multiple color fluorescence imaging microscopy. *Cytom Part A* **1999,** *35* (3), 214-226.

20. Reynolds, G.; Drexhage, K., New coumarin dyes with rigidized structure for flashlamp-pumped dye lasers. *Optics Communications* **1975,** *13* (3), 222-225.

21. Patterson, G. H.; Piston, D. W., Photobleaching in two-photon excitation microscopy. *Biophys J* **2000,** *78* (4), 2159-62.

22. Pujol, N.; Cypowyj, S.; Ziegler, K.; Millet, A.; Astrain, A.; Goncharov, A.; Jin, Y.; Chisholm, A. D.; Ewbank, J. J., Distinct innate immune responses to infection and wounding in the C. elegans epidermis. *Curr Biol* **2008,** *18* (7), 481-9.

23. Pujol, N.; Zugasti, O.; Wong, D.; Couillault, C.; Kurz, C. L.; Schulenburg, H.; Ewbank, J. J., Anti-fungal innate immunity in C. elegans is enhanced by evolutionary diversification of antimicrobial peptides. *PLoS Pathog* **2008,** *4* (7), e1000105.

VITA

Fengyuan is the son of Hongfeng Deng and Yuan Wang. He was born in Qingdao, Shandong, China on August 8th, 1990. He graduated from University of South Carolina – Columbia with B.S. in 2013 with major in chemistry and minor in statistics. Fengyuan started his graduate study at Purdue University in 2014 and joined Professor Garth Simpson's lab focusing on instrumentation and method development of nonlinear optical spectroscopy and microscopy.

PUBLICATIONS

1. Newman, J. A.; Schmitt, P. D.; Toth, S. J.; Deng, F.; Zhang, S.; Simpson, G. J., Parts per million powder X-ray diffraction. *Analytical Chemistry* **2015**, 87 (21), 10950-10955.

2. Deng, F.; Ulcickas, J. R.; Simpson, G. J., Theoretical Foundation for Electric-Dipole-Allowed Chiral-Specific Fluorescence Optical Rotary Dispersion (F-ORD) from Interfacial Assemblies. *J Phys Chem Lett* **2016**, 7 (21), 4248-4252.

3. Ding, C.; Ulcickas, J. R.; Deng, F.; Simpson, G. J., Second Harmonic Generation of Unpolarized Light. *Physical review letters* **2017**, 119 (19), 193901.

4. Deng, F.; Ding, C.; Martin, J. C.; Scarborough, N. M.; Song, Z.; Eakins, G. S.; Simpson, G. J., Spatial-spectral multiplexing for hyperspectral multiphoton fluorescence imaging. *Optics Express* **2017**, 25 (26), 32243-32253.

5. Ulcickas, J. R.; Deng, F.; Ding, C.; Simpson, G. J. In Mueller tensor approach for nonlinear optics in turbid media, *Multiphoton Microscopy in the Biomedical Sciences XVIII, International Society for Optics and Photonics:* **2018**; p 1049834.

6. Deng, F.; Ding, C.; Martin, J. C.; Scarborough, N. M.; Song, Z.; Eakins, G. S.; Simpson, G. J. In Video-rate hyperspectral two-photon fluorescence microscopy for in vivo imaging, *High-Speed Biomedical Imaging and Spectroscopy III: Toward Big Data Instrumentation and Management, International Society for Optics and Photonics:* **2018**; p 105050W.

THE JOURNAL OF PHYSICAL CHEMISTRY Letters

Letter

pubs.acs.org/JPCL

Theoretical Foundation for Electric-Dipole-Allowed Chiral-Specific Fluorescence Optical Rotary Dispersion (F-ORD) from Interfacial Assemblies

Fengyuan Deng,[†] James R. W. Ulcickas,[†] and Garth J. Simpson*

Department of Chemistry, Purdue University, 560 Oval Drive, West Lafayette, Indiana 47907, United States

ABSTRACT: Fluorescence optical rotary dispersion (F-ORD) is proposed as a novel chiral-specific and interface-specific spectroscopic method. F-ORD measurements of uniaxial assemblies are predicted to be fully electric-dipole-allowed, with corresponding increases in sensitivity to chirality relative to chiral-specific measurements in isotropic assemblies that are commonly interpreted through coupling between electric and magnetic dynamic dipoles. Observations of strong chiral sensitivity in prior single-molecule fluorescence measurements of chiral interfacial molecules are in excellent qualitative agreement with the predictions of the F-ORD mechanism and challenging to otherwise explain. F-ORD may provide methods to suppress background fluorescence in studies of biological interfaces, as the detected signal requires both polar local order and interfacial chirality. In addition, the molecular-level descriptions of the mechanisms underpinning F-ORD may also potentially apply to aid in interpreting chiral-specific Raman and surface-enhanced Raman spectroscopy measurements of uniaxially oriented assemblies, opening up opportunities for chiral-specific and interface-specific vibrational spectroscopy.

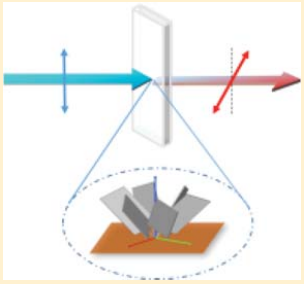

Absolute chirality plays a critical role in biological interactions, governing enzyme−substrate interactions.[1−3] To design a functioning pharmaceutical therapeutic agent, target chirality is typically a prerequisite. However, few probes are available to definitively characterize chirality. Vibrational circular dichroism (VCD) and Raman optical activity (ROA) are selective techniques commonly utilized for chiral sensing but are limited by low sensitivity.[4,5] Electronic circular dichroism (ECD) offers higher sensitivity, but the broad-band nature of electronic transitions reduces specificity.[6] Fully electric-dipole-allowed chiral-specific effects including circular extinction are reasonably well-established in measurements of crystalline materials. In studies of achiral dyes incorporated during crystal growth, Kahr and coworkers have nicely demonstrated the observation of chiral specificity for achiral dyes incorporated into chiral lattices.[7] In this instance, the circular dichroism observed arose from an interplay between birefringence in the crystal and linear dichroism from preferred crystal orientation and is thus limited to dye-doped crystalline and polycrystalline materials.[8] Alternative methods employing second-order nonlinear optical (NLO) spectroscopy have been shown to be highly sensitive to chirality, also through an electric-dipole-allowed mechanism.[9−11] Near 100% dichroic ratios have been observed for oriented binapthol monolayer films using second harmonic generation (SHG) circular dichroism (CD).[12] In addition, Fourier transform microwave spectroscopy has been employed for electric-dipole-allowed enantiomer-specific detection methods via triply resonant microwave nonlinear wave mixing.[13,14] However, the accessibility of NLO approaches is reduced by the requirement of a pulsed laser source at optical frequencies and the complexity of the experiments in general. One-photon fluorescence (1PF), in contrast, does not require a coherent or pulsed light source and can be easily implemented into existing fluorescence microscopes. Here we propose a new spectroscopic method based on 1PF that is selective to chirality at interfaces.

A simple physical model explaining the prediction of electric-dipole-allowed chiral-specific fluorescence in uniaxial assemblies is shown in Figure 1 in the limiting case of orthogonally polarized absorption (blue arrow) and fluorescence (red arrow) transition moments. A nonzero net rotation in the primary axis of polarization can be observed between the projections of $\vec{\mu}^a$ and $\vec{\mu}^f$ on the $X-Y$ plane. Excitation with linearly polarized light will result in fluorescence that, on average, yields a maximum in the polarized emission intensity that is rotated relative to the excitation axis. This rotation is the origin of the chiral-specific signal. From inspection of the graphic, the F-ORD process is nonreciprocal such that flipping the surface through a 180° rotation about the X axis will result in the opposite sense of rotation.

The mathematical framework for chiral-specific fluorescence builds most directly on the electric-dipole-allowed orientational mechanism underpinning chiral-specific four-wave mixing described by Davis et al.[15] In this mechanism, a chiral-specific nonlinear optical field can be produced even in the absence of intrinsic chirality within the chromophore through chiral orientational arrangement in an ensemble. The macroscopic chirality arises purely through packing effects and does not

Received: August 11, 2016
Accepted: September 30, 2016
Published: September 30, 2016

DOI: 10.1021/acs.jpclett.6b01814
J. Phys. Chem. Lett. 2016, 7, 4248−4252

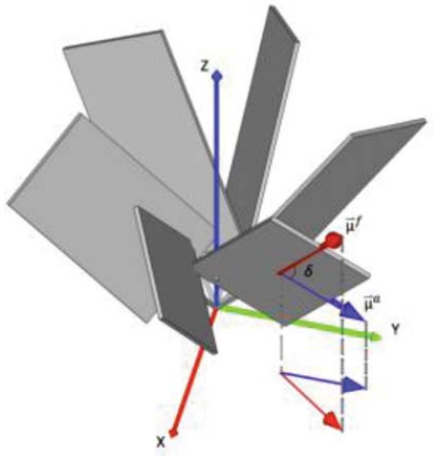

Figure 1. Graphic illustration of planar fluorophores (represented by gray plates) with uniaxial symmetry in the laboratory $X-Y-Z$ frame. The Euler angle φ is uniformly sampled for the assembly. Detected signal is defined in the projection onto the laboratory $X-Y$ plane. Y-polarized excitation results in fluorescence detected at an angle rotated clockwise, as shown in the projection.

require any coupling between chromophores or chiral distortion. Furthermore, because both the chiral and achiral responses are fully electric-dipole-allowed, they are often comparable in magnitude, yielding dichroic ratios approaching unity under favorable conditions. A qualitatively similar mechanism is well-established for describing the high sensitivity of chirality in surface second harmonic and sum frequency generation.

The connection between the experimental observables and the molecular properties can be constructed by starting with fundamental light matter interactions at the molecular level. The process of absorption can be described either by a transition dipole moment μ^i or more formally by the imaginary component of the polarizability matrix α^{ij}, where i, j represents the polarization of the emission and excitation light, respectively. The two formalisms are connected by the following equation describing the excitation from state I to state n. The damping term Γ describes the half width at half-maximum of the line shape function.

$$\alpha^{ij}(-\omega;\,\omega) = \frac{1}{\hbar}\sum_n \frac{\mu_{In}^i \mu_{nI}^j}{\omega_n - \omega - i\Gamma_n} + \frac{\mu_{In}^j \mu_{nI}^i}{\omega_n + \omega + i\Gamma_n} \tag{1}$$

For a molecule initially in the ground state such that $I = 0$, the first term in the summation will dominate because the excited state lies at an energy higher than the initial state. In the case of fluorescence emission, the second term dominates, as the initial state is higher in energy than the state contributing to the resonance enhancement.[16] Only the imaginary contributions to the polarizability impact the overall attenuation or amplification of the optical field, corresponding to absorption or emission, respectively. The polarization dependence of absorption and emission is dictated by the terms in the numerator. In a molecular coordinate system in which the z' axis parallels the fluorescence emission transition moment and the absorption transition moment lies in the $x'-z'$ plane, the fluorescence transition moment has only one nonzero term $\mu_{z'}^f = |\vec{\mu}^f|$, and the absorption transition moment has two components: $(\mu_{nI}^{x'})^a = |(\vec{\mu}_{nI})^a| \sin\delta$ and $(\mu_{nI}^{z'})^a = |(\vec{\mu}_{nI})^a| \cos\delta$, where δ defines the angle between the fluorescence and absorption transition moments consistent with Figure 1.

Using the relation $\vec{\mu}_{nm} = \vec{\mu}_{mn}^*$, the expression for the linear polarizability describing absorption in eq 1 can be rewritten as follows for a molecule initially in the ground state $I = 0$.

$$\begin{aligned}
\alpha^{x'x'} &\cong S(\omega)|\vec{\mu}_{n0}|^2 \sin^2\delta \\
\alpha^{z'z'} &\cong S(\omega)|\vec{\mu}_{n0}|^2 \cos^2\delta \\
\alpha^{x'z'} &= \alpha^{z'x'} \cong S(\omega)|\vec{\mu}_{n0}|^2 \sin\delta\cos\delta
\end{aligned} \tag{2}$$

where the $S(\omega)$ describes the resonance line-shape function. If it is assumed that molecular rotation is slow relative to the fluorescence lifetime, the orientational averages connecting the molecular frame to the laboratory frame are performed over the combined coordinates describing absorption and emission.

In a general sense, the intensity of pure linearly polarized fluorescence as a function of the polarization rotation angle γ for linearly polarized excitation light depends on the following three trigonometric polynomial coefficients $A-C$.

$$I_n(\gamma) = A_n \cos^2\gamma + B_n \sin\gamma\cos\gamma + C_n \sin^2\gamma \tag{3}$$

In the above equation, n may refer to the Stokes frame horizontal polarization (H) or vertical polarization (V). These three coefficients are in turn related back to the molecular orientation distribution and the transition moments within the molecular frame. Furthermore, if the angle between the absorption and emission angles is defined to be δ described above, the expressions for the polynomial coefficients can be rewritten in terms of δ, as shown below for H polarized detection.

$$A_H = K(|\vec{\mu}^f|^2|\vec{\mu}^a|^2)\left\{\begin{array}{l}\cos^2\delta\langle(R_{Xz'}R_{Xz'})^f(R_{Xz'}R_{Xz'})^a\rangle \\ +\,2\sin\delta\cos\delta\langle(R_{Xz'}R_{Xz'})^f(R_{Xx'}R_{Xz'})^a\rangle \\ +\sin^2\delta\langle(R_{Xz'}R_{Xz'})^f(R_{Xx'}R_{Xx'})^a\rangle\end{array}\right\} \tag{4}$$

$$B_H = K(|\vec{\mu}^f|^2|\vec{\mu}^a|^2)\left\{\begin{array}{l}\cos^2\delta\langle(R_{Xz'}R_{Xz'})^f(R_{Xz'}R_{Yz'})^a\rangle \\ +\sin^2\delta\langle(R_{Xz'}R_{Xz'})^f(R_{Xx'}R_{Yx'})^a\rangle\end{array}\right\} \tag{5}$$

$$C_H = K(|\vec{\mu}^f|^2|\vec{\mu}^a|^2)\left\{\begin{array}{l}\cos^2\delta\langle(R_{Xz'}R_{Xz'})^f(R_{Yz'}R_{Yz'})^a\rangle \\ +\,2\sin\delta\cos\delta\langle(R_{Xz'}R_{Xz'})^f(R_{Yx'}R_{Yz'})^a\rangle \\ +\sin^2\delta\langle(R_{Xz'}R_{Xz'})^f(R_{Yx'}R_{Yx'})^a\rangle\end{array}\right\} \tag{6}$$

The degeneracy of the input photon polarizations ($\alpha^{x'y'} = \alpha^{y'x'}$) produces two orientational averages equal in magnitude but opposite in sign, yielding a net zero $\sin(\delta)\cos(\delta)$ term for the B coefficient. Expressions for each of the eight orientational averages in eqs 4–6 for a uniform distribution in φ have been explicitly evaluated previously.[15] The orientational averages for the contribution in B_H are given by the following expressions.

$$\langle(R_{Xz'}R_{Xz'})^f(R_{Xz'}R_{Yz'})^a\rangle = 0 \tag{7}$$

DOI: 10.1021/acs.jpclett.6b01814
J. Phys. Chem. Lett. 2016, 7, 4248–4252

$$\langle (R_{Xz'}R_{Xz'})^f (R_{Xx'}R_{Yx'})^a \rangle = \frac{1}{4}\langle \sin^2\theta \cos\theta \sin\psi \cos\psi \rangle \quad (8)$$

In the presence of a mirror plane containing the unique axis, the B term goes to zero due to the corresponding even symmetry in the distributions in ψ. Thus only ensembles exhibiting chiral order will display this response; the B coefficient contribution to detected signal is hereby referred to as the chiral-specific signal. The origin of the chiral-specific signal can be understood from the nonzero orientational average in eq 8. Note that a chiral uniaxial assembly alone is thus insufficient to observe F-ORD experimentally; a nonzero orientational average $\langle \sin^2(\theta)\cos(\theta) \rangle$ is required and implied by the term polar order. Using a lipid monolayer on an air/water interface as an example, the aliphatic moiety for the ensemble is virtually always oriented away from the bulk liquid, giving the whole interface a polar orientation. In contrast, a bilayer of those same lipids can exhibit alignment about a unique axis but no preferred orientation (i.e., polar order) and no corresponding F-ORD response. The B_H coefficient is given by the following equation as a function of orientational parameters and the transition moments of the fluorophore.

$$B_H \propto \langle \sin^2\theta \cos\theta \sin\psi \cos\psi \rangle (|\mu_z^f|^2 |\mu_x^a|^2)$$
$$= |\vec{\mu}^f|^2 |\vec{\mu}^a|^2 \langle \sin^2\delta \langle \sin^2\theta \cos\theta \sin\psi \cos\psi \rangle \quad (9)$$

From eq 9, three requirements must be met to exhibit chiral specificity in the fluorescence produced from uniaxial assemblies: (i) the assembly exhibits polar order, such that the expectation values over the polar tilt angle θ are nonzero, (ii) the arrangement of the plane containing the absorption and fluorescence transition dipoles must exhibit a chiral twist such that the expectation values over ψ are nonzero, and (iii) the transition moments for absorption and fluorescence are nonparallel such that δ is nonzero. In the limit of a uniform distribution in ψ, both orientational averages in eq 8 approach zero.

The magnitude of the F-ORD signal can be interpreted in the context of a linear intensity difference (LID) measurement most analogous to circular intensity difference measurements with circularly polarized excitation. In LID measurements, the polarized fluorescence intensity is measured for +45 and −45° linear polarizations, with the difference in the detected intensity directly connected to the F-ORD rotation angle.

$$\mathrm{LID} \equiv \frac{I_H(+45) - I_H(-45)}{I_H(+45) + I_H(-45)} = \frac{B_H}{A_H + C_H} \quad (10)$$

There are an infinite set of angles which generate a maximal dissymmetry parameter due to the interplay between the functions of θ and δ. For $\delta = 90°$, explicit evaluation for the theoretical maximum using eqs 10 and 4−6 yields an LID maximum of 25% with $\theta = 65.8°$ and $\psi = 22.3°$. The azimuthal distribution in molecular orientation results in a reduction in the LID values relative to the theoretical maximum of 1 for an infinitely sharp azimuthal orientation distribution or for single molecules. Note, however, that typically reported electronic CD g values are on the order of 10^{-3}. It is posited that because the F-ORD mechanism arises purely from electric dipole contributions the generated signal may be much greater.

Evidence supporting the potential relevance of this proposed mechanism can be found in single-molecule fluorescence studies of chiral molecules first reported by Barnes and coworkers, reproduced with permission in Figure 2. In that study, Barnes and coworkers observed dissymmetry parameter

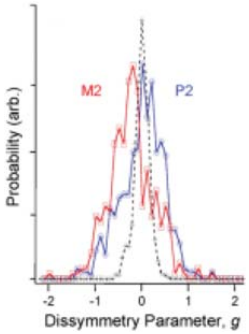

Figure 2. Normalized fluorescence-detected circular dichroism (FDCD) histogram published by Barnes and coworkers.[17] The blue and red traces represent the signal from right (*P2*) and left (*M2*) handed helical structures, respectively. Mean g values reported were 0.52 and −0.63, respectively, two orders of magnitude greater than the bulk response. Reproduced with permission from ref 17. © 2006 AAAS.

g related to differences in fluorescence intensity for right versus left circularly polarized excitation.[17] Clear statistically significant differences were observed in the histograms of g values produced for the two senses of helicity for the chiral fluorophores used.

In follow-up work by Cohen and coworkers,[18,19] it was suggested that the dichroic mirrors altered polarization incident to the sample. It was demonstrated that the dichroic mirror induced phase shifts and had different reflectivity efficiencies. Furthermore, corrections to ensure pure circular polarizations at the sample resulted in significant decreases in the spread and magnitude of g values obtained. Cohen and coworkers concluded that the observation of nonzero dissymmetry could be attributed to the presence of linear dichroism rather than circular dichroism. In subsequent studies by Barnes and coworkers, a reduction in dissymmetry was confirmed when particular attention was taken to remove potential artifacts from linear dichroism, although the underlying sensitivity to absolute chirality remained.[20]

Interestingly, no subsequent work has to our knowledge appeared to address what are arguably the most exciting observations in the original study, namely, the observed chiral specificity in the single-molecule linear dichroism contributions to the Barnes and coworkers' measurements. The results shown in Figure 2 demonstrate clear differences in the mean values of the dissymmetry factors for the two diastereomers at the interface. These observations can potentially be explained through the F-ORD mechanism proposed herein.

The presence of unanticipated F-ORD contributions in the prior experimental design can be understood by considering the influence of the Jones matrices for the optical path in the original study, as subsequently detailed by Cohen and coworkers. In brief, the Jones matrix describing the polarization state of the incident circularly polarized light upon reflection from a dichroic mirror can be broken up into a complex component describing elliptically polarized light along the eigenpolarizations of the mirror and a purely real component corresponding to ±45° linear polarization.

DOI: 10.1021/acs.jpclett.6b01814
J. Phys. Chem. Lett. 2016, 7, 4248−4252

$$\vec{e}^{\,a} = \begin{bmatrix} r_H^a & 0 \\ 0 & r_V^a \end{bmatrix} \frac{1}{\sqrt{2}} \begin{bmatrix} 1 \\ \pm i \end{bmatrix} = \begin{bmatrix} |r_H| & 0 \\ 0 & |r_V| e^{i\Delta} \end{bmatrix} \frac{1}{\sqrt{2}} \begin{bmatrix} 1 \\ \pm i \end{bmatrix}$$
$$= \frac{1}{\sqrt{2}} \begin{bmatrix} |r_H^a / r_V^a| - \sin \Delta \\ \pm i \cos \Delta \end{bmatrix} + \frac{\sin \Delta}{\sqrt{2}} \begin{bmatrix} 1 \\ \pm 1 \end{bmatrix} \quad (11)$$

In eq 11, r_H^a and r_V^a refer to the complex-valued amplitude reflection coefficients for the dichroic mirror (assuming the p and s eigenpolarizations coincide with the H and V reference frames of the image), and Δ is the phase shift in the polarization state induced by the mirror, given by $\Delta = \arg(r_H^a / r_V^a)$. From eq 10, the difference in detected intensity for $\pm 45^\circ$ is directly connected to the chiral-specific coefficients B_H and B_V. For detection of horizontally polarized light, the following equality emerges.

$$I_H(+45^0) - I_H(-45^0) = 2\left(\frac{1}{2} B_H\right) |t_H^f|^2 \quad (12)$$

Taking advantage of the identity $B_H = -B_V$, the integrated fluorescence intensity difference arising from residual linear dichroism can be connected to the transmission coefficients of the dichroic mirror along the return path at the fluorescence wavelength through the following relationship.

$$I_{tot}(+45^0) - I_{tot}(-45^0)$$
$$= B_H |t_H^f|^2 + B_V |t_V^f|^2$$
$$= B_H (|t_H^f|^2 - |t_V^f|^2) \quad (13)$$

From previous measurements of dichroic mirrors performed by the Cohen group,[18] reasonable values of $\Delta = 0.79$ were recorded for one dichroic mirror, corresponding to as much as ~1/2 the incident light potentially contributing to linear dichroism. From eq 13, the presence of a significant difference in transmissivity for the eigenpolarizations of the dichroic mirror prior to detection could provide one possible explanation for the observations of large dissymmetry factors directly tied to the sense of chirality. Conversely, unpolarized detection of the total fluorescence should yield no selectivity for chirality, consistent with the two transmissivity terms in eq 13 being equal. It would also explain the reductions in this sensitivity when using pure circular polarizations, corresponding to the case of $\Delta \cong 0$. Note that the reduction in signal observed with circularly polarized light is entirely consistent with the Cohen response in 2009, where it was noted that careful treatment of polarization purity to ensure pure CPL at the sample resulted in sharp collapse of the distribution of g about zero. Finally, it suggests that the overall sensitivity to chirality could be significantly improved yet further through optimization of the experiment to explicitly target F-ORD measurements.

It is interesting to compare and contrast the proposed mechanism with previous work by Cohen and coworkers, describing "superchiral" light arising in the vicinity of nodes present at highly reflective interfaces.[18,21,22] In brief, the electric dipole contributions approach zero at a node, while the same effect does not arise for magnetic dipole contributions. As such, suppression of the electric-dipole-induced fluorescence results in a relative enhancement in the chiral-specific magnetic dipole contributions and a correspondingly large dissymmetry factor. This mechanism produces a greater g value with a maximum signal detected for pure circularly polarized light and zero signal for linearly polarized light. In contrast, the F-ORD mechanism, as detailed above, yields a minimum g value for circularly polarized light, as evidenced by the 2009 response to the original Barnes manuscript.[18] In a followup manuscript by Barnes and coworkers in 2012, it was shown that careful treatment to reduce linear polarization contamination resulted in a reduction in dissymmetry parameters g, consistent with the predictions of F-ORD and contrary to those of the "superchiral" light mechanism.[23]

It is worthwhile to compare and contrast the chiral-specific response predicted for fluorescence with the fully electric-dipole-allowed chiral-specific Raman from oriented assemblies first considered several years ago by Efrima and subsequently refined by Hecht and Barron.[24,25] In brief, symmetry arguments indicated the possibility of electric-dipole-allowed chiral-specific Raman optical activity (ROA) in chiral assemblies exhibiting polar order. In that work, electric-dipole-allowed ROA was predicted to be possible from macroscopic symmetry arguments, with the ROA scaling with the antisymmetric component of the Raman tensor. Because antisymmetry is enhanced near electronic resonance, ROA was predicted to be enhanced in resonance Raman measurements. These predictions were subsequently confirmed experimentally and put to great advantage in surface-enhanced Raman measurements.[26] This confirmation has led to a recent growth in SEROA arising from molecules assembled at the surfaces of metal nanoparticles. Despite the successes of SEROA, few detailed molecular level interpretations have emerged for the origins of the chiral specificity in terms of the molecular orientation distribution at the interface, such that ab initio interpretations of SEROA measurements for absolute chirality determination remain challenging.

More recent independent studies of coherent four-wave mixing of uniaxial assemblies[15] may potentially help clarify the origin of the chiral specificity of spontaneous Raman in SEROA measurements and their possible connection to chiral-specific fluorescence. In that work, explicit expressions were derived for the orientational averages connecting the molecular frame to the interfacial frame for all coherent four-wave mixing measurements. Fortunately, both fluorescence and the spontaneous Raman processes can be treated mathematically with the same framework as four-wave mixing, although with two of the four fields produced by the sample rather than one as in CARS. These general expressions are equally valid for spontaneous Raman and fluorescence, providing a route for clarifying the molecular-level requirements for both electric-dipole-allowed chiral-specific Raman and F-ORD.

In summary, a framework for the theoretical description of chiral-specific fluorescence was described. The proposed model imposes the following molecular constraints: (i) the presence of a significant difference between the absorption and emission transition moment orientations within the molecular frame, (ii) polar order of a uniaxial interface, and (iii) ensemble chirality. The F-ORD chiral-specific signal was mathematically connected to the B polynomial coefficient in polarization rotation measurements and to linear intensity difference measurements of chiral assemblies. The model provides a novel electric-dipole-allowed mechanism for chiral-specific fluorescence, which may explain the remarkable linear dissymmetry parameters previously reported by Barnes and Cohen. Furthermore, the described framework lends itself to future extension into the theoretical treatment of SEROA measurements, providing increased generality over previous treatments.

DOI: 10.1021/acs.jpclett.6b01814
J. Phys. Chem. Lett. 2016, 7, 4248−4252

AUTHOR INFORMATION

Corresponding Author

*E-mail: gsimpson@purdue.edu.

Author Contributions

†F.D. and J.R.W.U. contributed equally.

Notes

The authors declare no competing financial interest.

ACKNOWLEDGMENTS

We gratefully acknowledge support from the NIH Grant Numbers R01GM-103401 and R01GM-103910 from the NIGMS. Support in the form of a Ross Assistantship from Purdue University is also graciously acknowledged.

REFERENCES

(1) Kohls, H.; Steffen-Munsberg, F.; Höhne, M. Recent Achievements in Developing the Biocatalytic Toolbox for Chiral Amine Synthesis. *Curr. Opin. Chem. Biol.* **2014**, *19*, 180−192.

(2) Yasukawa, K.; Asano, Y. Enzymatic Synthesis of Chiral Phenylalanine Derivatives by a Dynamic Kinetic Resolution of Corresponding Amide and Nitrile Substrates with a Multi-Enzyme System. *Adv. Synth. Catal.* **2012**, *354*, 3327−3332.

(3) Gupta, A. K.; Kazlauskas, R. J. Substrate Modification to Increase the Enantioselectivity of Hydrolases. A Route to Optically-Active Cyclic Allylic Alcohols. *Tetrahedron: Asymmetry* **1993**, *4*, 879−888.

(4) Syme, C. D.; Blanch, E. W.; Holt, C.; Jakes, R.; Goedert, M.; Hecht, L.; Barron, L. D. A Raman Optical Activity Study of Rheomorphism in Caseins, Synucleins and Tau. New Insight into the Structure and Behaviour of Natively Unfolded Proteins. *Eur. J. Biochem.* **2002**, *269*, 148−156.

(5) Barron, L. D.; Hecht, L.; McColl, I. H.; Blanch, E. W. Raman Optical Activity Comes of Age. *Mol. Phys.* **2004**, *102*, 731−744.

(6) Sreerama, N.; Woody, R. W. Estimation of Protein Secondary Structure from Circular Dichroism Spectra: Comparison of CONTIN, SELCON, and CDSSTR Methods with an Expanded Reference Set. *Anal. Biochem.* **2000**, *287*, 252−260.

(7) Kahr, B.; Freudenthal, J.; Gunn, E. Crystals in Light. *Acc. Chem. Res.* **2010**, *43*, 684−692.

(8) Claborn, K.; Chu, A. S.; Jang, S. H.; Su, F. Y.; Kaminsky, W.; Kahr, B. Circular extinction imaging: Determination of the absolute orientation of embedded chromophores in enantiomorphously twinned LiKSO4 crystals. *Cryst. Growth Des.* **2005**, *5*, 2117−2123.

(9) Rodrigues, S. P.; Lan, S.; Kang, L.; Cui, Y.; Cai, W. Nonlinear Imaging and Spectroscopy of Chiral Metamaterials. *Adv. Mater.* **2014**, *26*, 6157−6162.

(10) Lee, H.; Huttunen, M. J.; Hsu, K. J.; Partanen, M.; Zhuo, G. Y.; Kauranen, M.; Chu, S. W. Chiral Imaging of Collagen by Second-Harmonic Generation Circular Dichroism. *Biomed. Opt. Express* **2013**, *4*, 909.

(11) Haupert, L. M.; Simpson, G. J. Chirality in Nonlinear Optics. In *Annu. Rev. Phys. Chem.*; Annual Reviews: Palo Alto, 2009; pp 345−365.

(12) Petralli-Mallow, T.; Wong, T. M.; Byers, J. D.; Yee, H. I.; Hicks, J. M. Circular Dichroism Spectroscopy at Interfaces: a Surface Second Harmonic Generation Study. *J. Phys. Chem.* **1993**, *97*, 1383−1388.

(13) Patterson, D.; Schnell, M.; Doyle, J. M. Enantiomer-Specific Detection of Chiral Molecules via Microwave Spectroscopy. *Nature* **2013**, *497*, 475.

(14) Lobsiger, S.; Perez, C.; Evangelisti, L.; Lehmann, K. K.; Pate, B. H. Molecular Structure and Chirality Detection by Fourier Transform Microwave Spectroscopy. *J. Phys. Chem. Lett.* **2015**, *6*, 196−200.

(15) Davis, R. P.; Moad, A. J.; Goeken, G. S.; Wampler, R. D.; Simpson, G. J. Selection Rules and Symmetry Relations for Four-Wave Mixing measurements of Uniaxial Assemblies. *J. Phys. Chem. B* **2008**, *112*, 5834−5848.

(16) Moad, A. J.; Simpson, G. J. Self-Consistent Approach for Simplifying the Interpretation of Nonlinear Optical and Multiphoton Phenomena. *J. Phys. Chem. A* **2005**, *109*, 1316−1323.

(17) Hassey, R.; Swain, E. J.; Hammer, N. I.; Venkataraman, D.; Barnes, M. D. Probing the Chiroptical Response of a Single Molecule. *Science* **2006**, *314*, 1437−1439.

(18) Tang, Y. Q.; Cook, T. A.; Cohen, A. E. Limits on Fluorescence Detected Circular Dichroism of Single Helicene Molecules. *J. Phys. Chem. A* **2009**, *113*, 6213−6216.

(19) Cohen, A.; Tang, Y. Q. Reply to "Comment on 'Limits on Fluorescence Detected Circular Dichroism of Single Helicene Molecules'". *J. Phys. Chem. A* **2009**, *113*, 9759−9759.

(20) Hassey-Paradise, R.; Cyphersmith, A.; Tilley, A. M.; Mortsolf, T.; Basak, D.; Venkataraman, D.; Barnes, M. D. Dissymmetries in Fluorescence Excitation and Emission from Single Chiral Molecules. *Chirality* **2009**, *21*, E265−E276.

(21) Tang, Y. Q.; Cohen, A. E. Optical Chirality and Its Interaction with Matter. *Phys. Rev. Lett.* **2010**, *104*, 163901.

(22) Tang, Y. Q.; Cohen, A. E. Enhanced Enantioselectivity in Excitation of Chiral Molecules by Superchiral Light. *Science* **2011**, *332*, 333−336.

(23) Cyphersmith, A.; Surampudi, S.; Casey, M. J.; Jankowski, K.; Venkataraman, D.; Barnes, M. D. Chiroptical Dissymmetries in Fluorescence Excitation from Single Molecules of (M-2) Helicene Dimers. *J. Phys. Chem. A* **2012**, *116*, 5349−5352.

(24) Hecht, L.; Barron, L. D. Rayleigh and Raman Optical-Activity from Chiral Surfaces. *Chem. Phys. Lett.* **1994**, *225*, 525−530.

(25) Efrima, S. Raman Optical-Activity of Molecules Adsorbed on Metal Surfaces - Theory. *J. Chem. Phys.* **1985**, *83*, 1356−1362.

(26) Vargek, M.; Freedman, T. B.; Lee, E.; Nafie, L. A. Experimental observation of resonance Raman optical activity. *Chem. Phys. Lett.* **1998**, *287*, 359−364.

DOI: 10.1021/acs.jpclett.6b01814
J. Phys. Chem. Lett. 2016, 7, 4248−4252

Research Article Vol. 25, No. 26 | 25 Dec 2017 | OPTICS EXPRESS 32243
Optics EXPRESS

Spatial-spectral multiplexing for hyperspectral multiphoton fluorescence imaging

FENGYUAN DENG,[1,2] CHANGQIN DING,[1,2] JERALD C. MARTIN,[1] NICOLE M. SCARBOROUGH,[1] ZHENGTIAN SONG,[1] GREGORY S. EAKINS,[1] AND GARTH J. SIMPSON[1,*]

[1]*Department of Chemistry, Purdue University, 560 Oval Drive, West Lafayette, Indiana 47907, USA*
[2]*These authors contributed equally to this work*
[*]*gsimpson@purdue.edu*

Abstract: A spatial-spectral multiplexing two-photon excited fluorescence (TPEF) hyperspectral imaging system was demonstrated at 17 frames per second (fps) with over 2,000 effective spectral channels. The system exploited the hardware used in beam-scanning microscopy to perform multiplexing of spatial and spectral information, leading to two orders of magnitude reduction in data throughput. An iterative demultiplexing algorithm enabled robust classification and full spectral recovery without requiring prior knowledge of the emission spectra of the fluorophores. Proof-of-concept demonstrations were performed using spatially heterogeneous multicomponent laser dyes and live genetically encoded fluorescent *C. elegans*. This instrument requires minimal hardware modifications for most existing multiphoton microscope and provides the ability to acquire hyperspectral TPEF images at video rate. It has the potential for dynamic studies in deep tissue with multiple spectrally overlapping fluorescence tags.

OCIS codes: (110.0180) Microscopy; (110.3010) Image reconstruction techniques.

References and links

1. L. Gao and R. T. Smith, "Optical hyperspectral imaging in microscopy and spectroscopy - a review of data acquisition," J. Biophotonics **8**(6), 441–456 (2015).
2. F. Cutrale, V. Trivedi, L. A. Trinh, C. L. Chiu, J. M. Choi, M. S. Artiga, and S. E. Fraser, "Hyperspectral phasor analysis enables multiplexed 5D in vivo imaging," Nat. Methods **14**(2), 149–152 (2017).
3. R. Lansford, G. Bearman, and S. E. Fraser, "Resolution of multiple green fluorescent protein color variants and dyes using two-photon microscopy and imaging spectroscopy," J. Biomed. Opt. **6**(3), 311–318 (2001).
4. F. R. Bertani, E. Botti, L. Ferrari, V. Mussi, A. Costanzo, M. D'Alessandro, F. Cilloco, and S. Selci, "Label-free and non-invasive discrimination of HaCaT and melanoma cells in a co-culture model by hyperspectral confocal reflectance microscopy," J. Biophotonics **9**(6), 619–625 (2016).
5. S. Arrigoni, G. Turra, and A. Signoroni, "Hyperspectral image analysis for rapid and accurate discrimination of bacterial infections: A benchmark study," Comput. Biol. Med. **88**, 60–71 (2017).
6. C. L. Rink, M. M. Wernke, H. M. Powell, M. Tornero, S. C. Gnyawali, R. M. Schroeder, J. Y. Kim, J. A. Denune, A. W. Albury, G. M. Gordillo, J. M. Colvin, and C. K. Sen, "Standardized Approach to Quantitatively Measure Residual Limb Skin Health in Individuals with Lower Limb Amputation," Adv. Wound Care (New Rochelle) **6**(7), 225–232 (2017).
7. M. B. Sinclair, D. M. Haaland, J. A. Timlin, and H. D. Jones, "Hyperspectral confocal microscope," Appl. Opt. **45**(24), 6283–6291 (2006).
8. A. S. Luthman, S. Dumitru, I. Quiros-Gonzalez, J. Joseph, and S. E. Bohndiek, "Fluorescence hyperspectral imaging (fHSI) using a spectrally resolved detector array," J. Biophotonics **10**(6-7), 840–853 (2017).
9. H. R. Morris, C. C. Hoyt, and P. J. Treado, "Imaging Spectrometers for Fluorescence and Raman Microscopy - Acoustooptic and Liquid-Crystal Tunable Filters," Appl. Spectrosc. **48**, 857–866 (1994).
10. P. M. Kasili and T. Vo-Dinh, "Hyperspectral imaging system using acousto-optic tunable filter for flow cytometry applications," Cytometry A **69**(8), 835–841 (2006).
11. T. Nöbauer, O. Skocek, A. J. Pernía-Andrade, L. Weilguny, F. M. Traub, M. I. Molodtsov, and A. Vaziri, "Video rate volumetric Ca2+ imaging across cortex using seeded iterative demixing (SID) microscopy," Nat. Methods **14**(8), 811–818 (2017).
12. R. Prevedel, Y. G. Yoon, M. Hoffmann, N. Pak, G. Wetzstein, S. Kato, T. Schrödel, R. Raskar, M. Zimmer, E. S. Boyden, and A. Vaziri, "Simultaneous whole-animal 3D imaging of neuronal activity using light-field microscopy," Nat. Methods **11**(7), 727–730 (2014).

#307637 https://doi.org/10.1364/OE.25.032243
Journal © 2017 Received 28 Sep 2017; revised 20 Nov 2017; accepted 30 Nov 2017; published 11 Dec 2017

Research Article Vol. 25, No. 26 | 25 Dec 2017 | OPTICS EXPRESS 32244
Optics EXPRESS

13. S. Z. Sullivan, R. D. Muir, J. A. Newman, M. S. Carlsen, S. Sreehari, C. Doerge, N. J. Begue, R. M. Everly, C. A. Bouman, and G. J. Simpson, "High frame-rate multichannel beam-scanning microscopy based on Lissajous trajectories," Opt. Express **22**(20), 24224–24234 (2014).
14. J. G. Dwight and T. S. Tkaczyk, "Lenslet array tunable snapshot imaging spectrometer (LATIS) for hyperspectral fluorescence microscopy," Biomed. Opt. Express **8**(3), 1950–1964 (2017).
15. A. D. Elliott, L. Gao, A. Ustione, N. Bedard, R. Kester, D. W. Piston, and T. S. Tkaczyk, "Real-time hyperspectral fluorescence imaging of pancreatic β-cell dynamics with the image mapping spectrometer," J. Cell Sci. **125**(Pt 20), 4833–4840 (2012).
16. C. F. Cull, K. Choi, D. J. Brady, and T. Oliver, "Identification of fluorescent beads using a coded aperture snapshot spectral imager," Appl. Opt. **49**(10), B59–B70 (2010).
17. L. Gao, R. T. Kester, N. Hagen, and T. S. Tkaczyk, "Snapshot Image Mapping Spectrometer (IMS) with high sampling density for hyperspectral microscopy," Opt. Express **18**(14), 14330–14344 (2010).
18. L. Gao and L. V. Wang, "A review of snapshot multidimensional optical imaging: Measuring photon tags in parallel," Phys. Rep. **616**, 1–37 (2016).
19. Y. Garini, A. Gil, I. Bar-Am, D. Cabib, and N. Katzir, "Signal to noise analysis of multiple color fluorescence imaging microscopy," Cytometry **35**(3), 214–226 (1999).
20. G. A. Reynolds and K. H. Drexhage, "New coumarin dyes with rigidized structure for flashlamp-pumped dye lasers," Opt. Commun. **13**, 222–225 (1975).
21. G. H. Patterson and D. W. Piston, "Photobleaching in two-photon excitation microscopy," Biophys. J. **78**(4), 2159–2162 (2000).
22. N. Pujol, S. Cypowyj, K. Ziegler, A. Millet, A. Astrain, A. Goncharov, Y. Jin, A. D. Chisholm, and J. J. Ewbank, "Distinct innate immune responses to infection and wounding in the C. elegans epidermis," Curr. Biol. **18**(7), 481–489 (2008).
23. N. Pujol, O. Zugasti, D. Wong, C. Couillault, C. L. Kurz, H. Schulenburg, and J. J. Ewbank, "Anti-fungal innate immunity in C. elegans is enhanced by evolutionary diversification of antimicrobial peptides," PLoS Pathog. **4**(7), e1000105 (2008).

1. Introduction

Fluorescence hyperspectral imaging is a powerful tool for biological studies as it provides an additional dimension of information compared to filter based multispectral fluorescence microscopes [1, 2]. The expansion in the spectral domain enables accurate classification and quantitative analysis of multiple spectrally overlapping components in biological structures for studying complex biological processes [3, 4] and clinical diagnoses [5, 6]. In order to achieve hyperspectral imaging, a 3 dimensional (3D) data structure (x, y, λ) is typically populated. Traditional hyperspectral imaging techniques typically rely on spatial scanning [7, 8] or spectral scanning [9, 10]. Spatial scanning interrogates the emission profile (λ) of a single pixel or line scanned across the field of view (FoV) to construct the 3D data cube. Conversely, spectral scanning methods image the entire FoV (x, y) on a 2D area detector and probe a single wavelength (λ) at a time. The speed of acquisition is typically limited by the mechanical movement of the dispersive optics and integration time for the detector array, which also introduces 1/f noise into the measurement. Capturing inherent dynamics of living systems such as Ca^{2+} oscillations associated with neuron firing typically requires a frame rate at around 20 Hz [11, 12]. Furthermore, significant blur from cardiovascular motion degrades resolution for *in vivo* imaging [13]. The bandwidth of current computer I/O interfaces also bottlenecks the achievable frame rate for uncompressed hyperspectral imaging. For a system with 2000 fluorescence channels, 16 bits per channel, 512 × 512 images at 20 frames per second (fps) speed, the overall data throughput is about 20.97 GB/s compared to the theoretical limit of a modern PCI-E 3.0 × 16 interface at 15.76 GB/s. The write speed of a commercially available storage device is typically less than a few gigabytes per second, representing a practical limit on data throughput.

Recently, several snapshot hyperspectral imaging systems were developed to improve the image acquisition speed while still maintaining reasonable data throughput rates [14–17]. Coded aperture snapshot spectral imager (CASSI) directly acquires the projection of a rotated data cube and reconstructs the hyperspectral images using a sparse sampling algorithm [16]. Alternatively, an image mapping spectrometer (IMS) spatially offsets the data cube layer by layer and projects each layer onto an isolated region of a large area detector [17, 18]. Both of these methods provide innovative strategies to overcome the scanning mechanism and

Research Article Vol. 25, No. 26 | 25 Dec 2017 | OPTICS EXPRESS 32245
Optics EXPRESS

bandwidth limitation. However, most of the existing snapshot methods are not directly compatible with multi-photon excited fluorescence microscopy, which significantly increases the depth of penetration for *in vivo* imaging. Furthermore, images captured using focal plane array detectors generally introduce trade-offs between spatial and spectral resolution, as both sets of information must be encoded on the same fixed number of imaging channels.

In this work, we demonstrated an experimentally simple approach to achieve video-rate hyperspectral imaging for two-photon excited fluorescence (TPEF) through non-descanned spatial/spectral multiplexing (NDSSM) without degraded the spatial resolution. A 16-channel photomultiplier tube (PMT) array (Hamamatsu, H12311-40) was used as spatial-spectral multiplexing detector with fast single photon response time (ns), and paired with a 16-channel digital oscilloscope card (AlazarTech, ATS9416) for fast data digitization. Spatial-spectral multiplexing was achieved by performing non-descanned detection, such that the projections of the spectra illuminated onto the PMT array varied as a function of beam's scan position. Demultiplexing allowed recovery of spectra with over 2000 fluorescence channels at video rate (17 fps for frame size of 512 × 512 pixels). The data throughput for the 16-channel digital oscilloscope was compressed at 2.24 GB/s with the multiplexing, as opposed to 336 GB/s without compression.

It is interesting to consider the potential change in spatial resolution resulting from the spatial/spectral multiplexing. In CASSI measurements, multiplexing to recover spectral information necessarily comes at the expense of spatial resolution, since the same fixed number of pixels now report on combined spatial and spectral information. In contrast, all the spectral information in NDSSM is contained in the orthogonal spectral axis accessed by the excitation positions in the PMT array, such that hyperspectral images can potentially be acquired without sacrifices in spatial resolution or image quality.

2. Methods

2.1 Experimental Instrumentation

The hyperspectral imaging system is depicted in Fig. 1(A). In brief, a tunable 80 MHz Ti:sapphire femtosecond laser (Spectra-Physics, Mai Tai) was used for excitation. The beam was scanned across the sample using a resonant scanning mirror at 8.8 kHz (EOPC) for the fast-scan axis and a galvanometer mirror (Cambridge-Tech) for the slow-scan. A square aperture was placed in the rear conjugate plane to cut off the turning point of the resonant mirror to avoid sample damage. A 10 × 0.3 NA objective (Nikon) was used to focus the beam down to the sample with the fluorescence signal collected in the epi direction back through the same objective. The laser was tuned in a range of 800 - 1000 nm for different excitations with powers at the sample around 40 - 100 mW. A dichroic mirror and a band pass filter (Chroma, 350 – 700 nm) were used to isolate the fluorescence signals. A 4f lens pair directed the collimated fluorescence onto the center of a transmission diffraction grating (Wasatch Photonics, WP-600/600-25.4). The spectrally separated beam was then focused on to a 16 channel PMT array (Hamamatsu, H12311-40). The 16 channel PMT array electronics were custom built to improve the single photon response time by two orders of magnitude over the original design. The circuit for each channel consisted of a two-stage high-speed operational amplifier circuit connected directly to the output of each element on the PMT array. The output was AC-coupled into a 50 Ω impedance microstrip through a custom printed circuit board (PCB) trace in order to provide impedance matching to the output transmission line. Responses of the PMT array were digitized synchronously with the laser pulses by using a 16 channel PCI-E digital oscilloscope card and remapped into sixteen 512 × 512 images via custom software (MATLAB).

Research Article Vol. 25, No. 26 | 25 Dec 2017 | OPTICS EXPRESS 32246
Optics EXPRESS

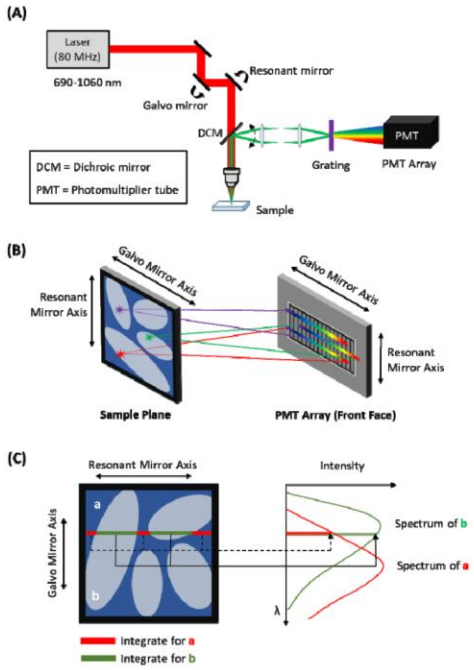

Fig. 1. Overview of spatial-spectral multiplexing. (A) Instrument schematic. (B) Illustration of spectra projected on the PMT array from different pixels in one image plane. (C) Spectral reconstruction from a single channel image for two components with different spectra.

2.2 Sample preparation

Fluorescein, coumarin 6, sodium dodecyl sulfate, and chloroform were purchased from Sigma-Aldrich, with eFluor 450 obtained from Thermo Fisher. All aqueous solutions were prepared with Milli-Q water (18.2 MΩ cm^{-1}). For emulsion mixtures with two components, stock solutions of 5 μM fluorescein in water and 50 μM coumarin 6 in chloroform were prepared separately. The two stock solutions were mixed equally in amount with ~1mg of sodium dodecyl sulfate. Then the mixture was shaken by hand to produce a stable emulsion mixture for imaging. For emulsion mixtures with three components, stock solutions of fluorescein in water, coumarin 6 in chloroform, and eFluorTM 450 in chloroform were made separately with a concentration of 50 μM for each. Then two two-component emulsion mixtures were prepared separately for eFluor 450 / fluorescein and coumarin 6 / fluorescein system based on the procedure above, and the two two-component emulsion mixtures were mixed in equal parts to produce a three-component emulsion mixture.

For high speed live animal imaging, genetically modified nematode (C. elegans) strains were cultured on agar plates seeded with Escherichia coli at 20 °C. While imaging, C. elegans strains were sealed between two glass coverslips immersed in 0.9 % NaCl physiological saline.

Research Article Vol. 25, No. 26 | 25 Dec 2017 | OPTICS EXPRESS 32247
Optics EXPRESS

2.3 Spectral reconstruction and component classification

A spectral retrieval algorithm was developed to analyze the raw data. Since the incident angle of the beam onto the diffraction grating varied during the beam scanning, each set of the 16 images from different channels was correlated spatially and spectrally for the same FoV. For each frame, pixels with the same galvanometer mirror position shared the same spectral projection pattern on the PMT array; while pixels along the galvanometer mirror axis produced unique projections as a function of position [Fig. 1(B)]. Therefore, spectrum can be generated by integrating all signals from the same fluorophore along the resonant mirror axis while the galvanometer axis contained wavelength information [Fig. 1(C)].

For an emission spectrum $s^0(\lambda)$ from one fluorophore (i.e., all locations of identical classification), the detected spectrum from a single PMT channel $s^{meas}(\lambda)$ can be described in Eq. (1), in which L is the spectral bandwidth of the PMT channel for a given galvanometer position. The measured spectral intensity $s_j^{meas}(\lambda)$ for a given measurement centered about the wavelength j is limited by L, which is equivalent to the entrance slit size of a spectrometer.

$$s_j^{meas} = \int s_j^0(\lambda) d\lambda \equiv \sum_{l=-L/2}^{L/2} s_{j+l}^0 \delta\lambda \tag{1}$$

In Eq. (1), $\delta\lambda$ corresponds the bandwidth of a single pixel in the final recovered spectrum, which is generally significantly smaller than the bandwidth dictated by the physical dimensions of the PMT L, and s_j^0 corresponds to the ground truth spectrum at the position j. Extending this analysis to each pixel in the image and the corresponding center position of the spectrum upon beam-scanning along the x-axis (galvo), the mathematical relationship described by summation in Eq. (1) corresponds to convolution of the ground truth spectrum with a rectangle function of width L.

$$\vec{s}^{meas} = \vec{s}^0 \otimes rect(L) \tag{2}$$

Significant signal to noise enhancement in the measured spectrum arises through integration of all the similarly classified locations along the orthogonal y-axis (resonant mirror). For a $\delta\lambda$ corresponding to each x-axis position in the image, a single detector can produce a spectrum with up to 512 elements in a 512×512 image.

While the single-detector approach described mathematically in Eq. (2) can in principle recover a complete spectrum at every position, the use of a PMT array has three critical practical benefits: i) measurements with an array produce detected intensity at each location to aid in spectral classification, ii) multiple array elements allow extension of the spectral dynamic range without requiring large displacements of the galvo-axis mirror, and iii) the higher collection efficiency of light and spectral overlap between channels results in signal to noise improvements. The spectral overlap between channels depended on the beam scanning path shown in Fig. 2(A) and the design of the 16-channel PMT array shown in Fig. 2(B). Each single PMT channel had a width of 0.8 mm with 0.2 mm gap between channels. For a FoV of 500 μm × 500 μm, 512 × 512 pixels with a 10 × objective, a narrow band emission was scanned across three adjacent PMT channels with the size of 2.5 mm × 2.5 mm, inducing ~2/3 overlap between the spectral windows for each PMT channel. For a single PMT channel, the detected narrow band emission had a width around 170 pixels along the galvo axis. In the case of no spectral overlap between adjacent detectors, the combined set of 16 detectors could in principle be used to generate a spectrum with 8,192 elements (16 × 512). To minimize edge effects, spectra with 460 spectral channels were used, correspond to a maximum of 7,360 channels. In practice, significant spectral overlap illustrated in Fig. 2(C) enabled spectral stitching and calibration, in which minimization of the squared deviations in the overlapping

Research Article Vol. 25, No. 26 | 25 Dec 2017 | OPTICS EXPRESS 32248
Optics EXPRESS

regions served to calibrate the relative sensitivities of adjacent detectors. As a result, ~2200 independent spectral channels were recovered after the stitching.

Second harmonic generation (SHG) from a doubling crystal (BBO) in the object plane was used as the reference as it generated uniformly distributed light across the FoV with a well-defined narrow band spectrum. By tuning the laser to 800 nm, 900 nm and 1000 nm, three references SHG spectra (centered at 400 nm, 450 nm, and 500 nm) were generated for calibration purposes (Fig. 2(C)). As a planar detector was used in the setup, signal projected on the blue and red end on the PMT array had slightly larger spectral separations compared to the center due to the longer projection length. It was consistent with the observation of 553 data points between 400 / 450 nm peaks and 549 data points between 450 / 500 nm peaks. The average channel density was used for the calibration. With a 100 mm lens to focus spectral pattern down to the PMT array, the width of the whole spectral window was about 200 nm. In this case, the rectangular function in Eq. (2) had a width corresponding to 15 nm (170 pixels), which limited the operational spectral resolution. The full width half maximum of the reconstructed SHG peak was 10 nm, compared to 2.5 nm for the excitation source measured by a spectrometer (Thorlabs, CCS175).

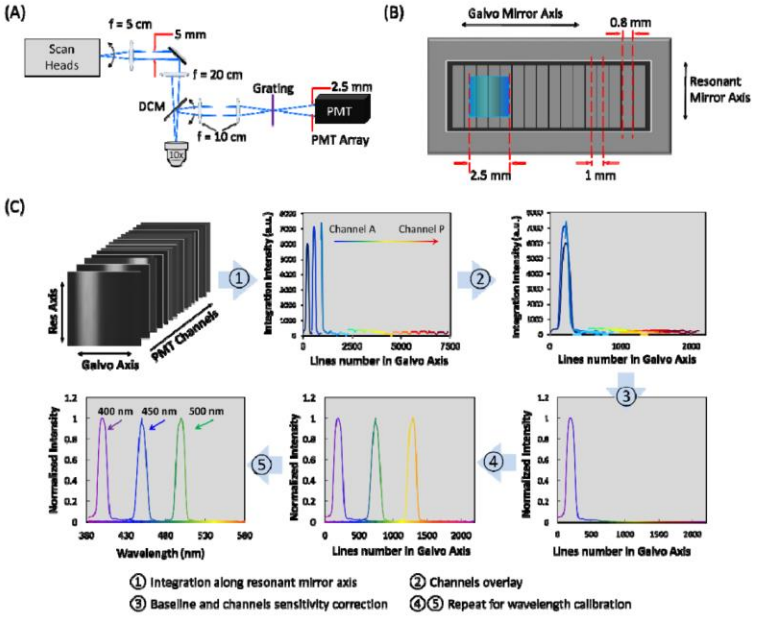

Fig. 2. (A) Beam scanning path (not the beam path). (B) The projection of spectrum of a narrow band emission on the PMT array. (C) Spectral window calibration with doubling crystal.

The preceding analysis describes the approach taken to recover spectra from pooled measurements of locations with identical composition. Obviously, this analysis first requires prior classification of *n* composition, which is described herein. A flow chart of the algorithm is shown in Fig. 3. In brief, a threshold was first set to identify signal pixels from the background. Next, a simple Euclidean angle (Eq. (3)) method was used for fluorescence

Research Article | Vol. 25, No. 26 | 25 Dec 2017 | OPTICS EXPRESS 32249
Optics EXPRESS

spectra classification. This method is consistent with previous classification approaches [19], selected primarily to minimize the analysis time.

$$\cos(\theta) = \frac{\vec{s}_{ref} \cdot \vec{s}_{x,y}}{\left|\vec{s}_{ref}\right| \cdot \left|\vec{s}_{x,y}\right|} \tag{3}$$

Pixels ($\vec{s}_{x,y}$) with large Euclidean angles relative to the n known reference spectra ($\vec{s}_{ref}$) (i.e., $\cos(\theta) < 0.99$) were collectively classified as an "other" component. As a result, discrete masks for each of the n + 1 components were generated. Spectra of all the components were then extracted based on the new discrete classification masks. This process was iterated until 99% of the pixels in the FoV were classified as the same component with the previous iteration. Following classification, spectral recovery for each class was performed as described in the preceding paragraph, with the process iteratively performed until convergence was achieved in both the spectra recovered and the spatial classifications. For data acquired at video-rate, the number of components and their spectra recovered from the first frame was used as the reference for the rest of the frames to reduce the spectral data analysis time. The computation time was dependent on the initial guess and the assumed number of components. For a two-component system, processing a single frame took about 20 to 50 seconds on a 4th generation hexa-core Intel Core i7 processor running in MATLAB. In order to initiate the iterative process, an initial guess spectrum was produced from the ensemble average of all pixels containing signal in the entire FoV, which served as the initial reference spectrum for a preliminary binary classification.

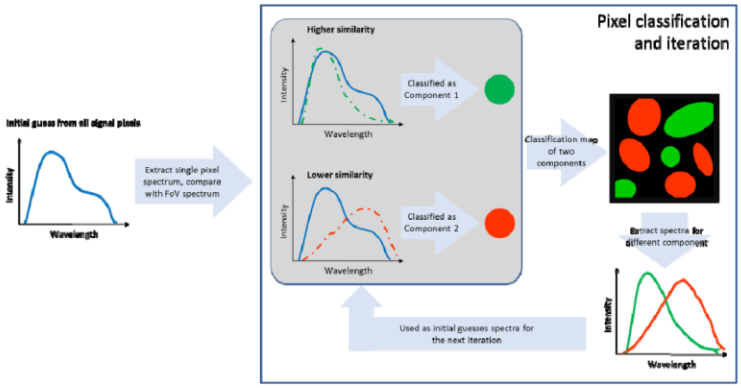

Fig. 3. Flowchart for the iterative classification algorithm.

3. Results and discussion

3.1 Heterogeneous mixtures of fluorescent dye droplets

A fluorescein/coumarin 6 fluorescent dye mixture was used to assess the spectral imaging of the system and the accuracy of the classification algorithm. Figure 4(A) showed a TPEF image from the integrated intensity of all 16 channels for this suspension under 800 nm excitation. A two-component classification image produced the images in Fig. 4(B), with one component labeled in green (component *a*) and another in blue (component *b*). It is worth noting that the recovered spectra of the two components were highly overlapping (Fig. 4(B) insert), making them difficult to confidently discriminate using a filter-based fluorescence microscope. The recovered spectra of this hyperspectral imaging system were overlaid with

Research Article | Vol. 25, No. 26 | 25 Dec 2017 | OPTICS EXPRESS 32250
Optics EXPRESS

independent measurements from a benchtop fluorimeter (FLS1000, Edinburgh Instruments) with 400 nm excitation (Figs. 4(D) and 4(E)). All spectra were normalized to the maximum intensity. The good agreement between the recovered spectra and the fluorimeter measurements was consistent with component *a* composed primarily of fluorescein in water and component *b* primarily coumarin 6 in chloroform, which also agreed with their anticipated respective solubility in water and chloroform. While the fluorescence emission spectra acquired by statistical decomposition were in good qualitative agreement with those obtained from independent measurements with a fluorimeter using pristine solutions, statistically significant deviations were present for both coumarin and fluorescein. In particular, the measurements obtained in the water/chloroform suspensions exhibited broader peaks than those interrogated in pure solutions. The increase in width for the suspensions is attributed to a combination of two effects; i) convolution of the emission spectrum with a rectangle function (vide supra) results in spectral broadening, and ii) the inhomogeneity of the environment in the water/chloroform suspension results in additional inhomogeneous broadening. From the measured SHG response, the contributions from convolution are insufficient to account for the observed differences in peak shapes. Therefore, the primary origin of the deviations observed between the emission spectra in Figs. 4(D) and 4(E) are attributed to spectral broadening associated with inhomogeneities from the greater diversity of environments available for partitioning (e.g., coumarin partitioning into the aqueous phase, fluorescence into chloroform, and both to the surfactant-stabilized interfaces). To study the fluorophores' distributions at the water-chloroform interface, analysis was repeated assuming a maximum number of three components. Under this case, the boundary of the chloroform droplets was identified as a third component (red in Fig. 4(C)). The recovered spectrum for the third components (component *c*) was shown in Fig. 4(F). The spectrum of component *c* (red dot line) was fitted as a linear combination of component *a* and component *b* as shown in solid line in Fig. 4(F) with R^2 = 0.99. Based on this fitting, component *a* (fluorescein in water) was weighted at 60.6% in the boundary between water and chloroform and component *b* (coumarin 6 in chloroform) was weighted at 39.1%. This method could provide new strategies for the study of surface interactions between different solvents.

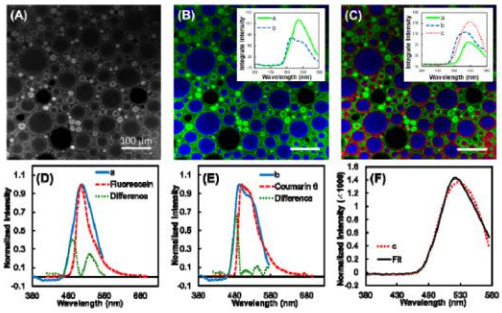

Fig. 4. (A) Integrated total fluorescence of a dye mixture (5μM fluorescein in water and 50 μM coumarin 6 in chloroform). (B) Classification under the assumption of two components (*a* in green and *b* in blue). Insert: recovered spectra of component *a* and *b*. (C) Classification under the assumption of three components (*a* in green, *b* in blue and *c* in red). Insert: recovered spectra for component *a*, *b* and *c*. (D) Overlay of recovered spectrum of component *a* with the fluorescein emission spectrum from a benchtop fluorimeter, and the difference between them. (E) Overlay of recovered spectrum of component *b* with the coumarin 6 emission spectrum, and the difference between them. Both plotted spectra were averaged over all the spatial positions of the same classified component. (F) Spectrum of the third component (red dotted line) fitted as a linear combination (black solid line) of the first two components.

Research Article Vol. 25, No. 26 | 25 Dec 2017 | OPTICS EXPRESS 32251
Optics EXPRESS

In Fig. 5, hyperspectral TPEF is demonstrated for measurements of fluorescence photobleaching, highlighting the advantages of high speed hyperspectral microscopy in the analysis of dynamic multicomponent mixtures. The three-component emulsions system of eFluor 450 (chloroform)/coumarin 6 (chloroform)/fluorescein (water) was used for this purpose. A video with both classification images and spectra can be found in the Supplementary Materials (Visualization 1). Figure 5(A) shows a single frame (frame number 55) from the video (green for fluorescein, blue for coumarin 6 and violet for eFluor 450). A target coumarin 6 droplet was circled in red for tracking the dynamic behavior. This frame was set as the start of the dynamic analysis (0 s), which corresponded to 3.2 s in the video. After 21.8 s, most of the coumarin 6 fluorescence was lost from photobleaching. Following the removal of the coumarin 6 signal, the classification of the target droplet was reclassified to 'eFluor 450' by the classification algorithm (circled in Fig. 5(B)). The total number of excitations driving photobleaching was plotted Fig. 5(D). In brief, the single-photon peak height distribution of the PMT was measured through a histogram analysis of a time-trace. The mean voltage per photon provided a point of calibration to convert the voltages acquired during imaging to absolute mean numbers of photons. The total number of emitted fluorescence photons for an isotropic emission was calculated based on the solid angle of collection through the objective. Previously measured values for the quantum efficiency of fluorescence for coumarin 6 [20] allowed conversion from the total number of emitted photons to the total number of excitations per unit time. The plot of total number of excitations was then fit to an exponential decay with a time constant of 5.16 ± 0.08 s, consistent with an exponential process routinely observed in photobleaching [21].

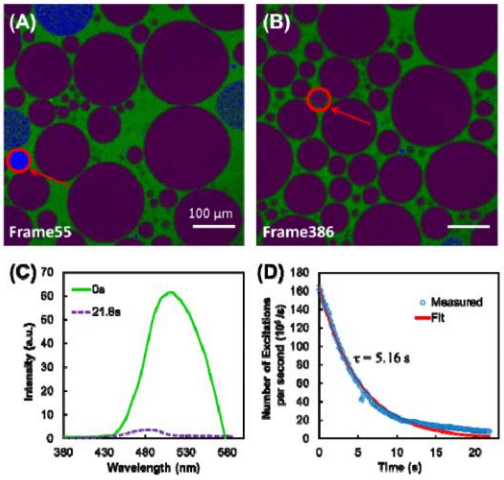

Fig. 5. Dye mixture with three fluorophores: fluorescein (green) in water, coumarin 6 (blue) and eFluor 450 (violet) in chloroform separately (also see Visualization 1). Target droplet with coumarin 6 in chloroform (circled in red) was tracked from its first appearance in frame 55, set as 0 s (A) and final misclassification in frame 386 with during time 21.8 s (B). (C) Spectra recovered from the target droplet at 0 s (green solid line) and 21.8 s (purple dash line). (D) Photobleaching curve of coumarin 6 in the target droplet (blue dot) with the exponential fit (red line).

Research Article | Vol. 25, No. 26 | 25 Dec 2017 | OPTICS EXPRESS 32252
Optics EXPRESS

3.2 In vivo imaging of genetically modified C. elegans

Genetically modified nematodes (*C. elegans*) were used as a living biological sample for the demonstration of fast hyperspectral imaging. *C. elegans* strains were obtained from the Caenorhabditis Genetics Center. The main phenotypes of this *C. elegans* variant are: green fluorescence in the body wall muscle nuclei [*ccIs4251*, green fluorescence protein (GFP)], green fluorescence in the pharyngeal muscle (*mIs12*, GFP), dumpy (*dpy-17*), red fluorescence in the epidermis (*frIs7*, DsRed), and red fluorescence in pharyngeal muscle (*uIs69*, mCherry). A video was acquired for the *C. elegans* with 17 fps, 512 × 512 pixels (Visualization 2, Supplementary Materials) and 800 nm excitation. Since only GFP and DsRed could be accessed by TPEF with 800 nm excitation, a two-component classification was shown in the video and Figs. 6(A) and 6(B). The two components were labeled in red and green separately with the recovered spectra shown in Fig. 6(C). In order to assure the accuracy of this microscopy and classification algorithm, a fluorescence image from a conventional fluorescence microscope (Olympus BX-51) was acquired for the same type of *C. elegans* with an excitation filter at 460 - 490 nm, as shown in Fig. 6(D). A similar distribution of the two structures with different fluorescence properties was observed, in which the outside epidermis of the *C. elegans* was red and the pharyngeal muscle in the head was green. In addition, the green fluorescence from the body wall muscle nuclei (*ccIs4251*) could also be seen in images acquired from our instrument. Compared to one photon excited fluorescence in Fig. 6(D), significantly less out of plane fluorescence was observed with the TPEF. Detailed biological structures could be seen along with the spectra for each component. Component 1 and component 2 were identified to be predominantly GFP and DsRed, respectively. In Visualization 2, an injury was induced in the mitotic region of the *C. elegans*. Consistent with surface infection, injury, or osmotic stress [22, 23], green fluorescence due to *frIs7* mutation was preferentially enhanced at the site of injury.

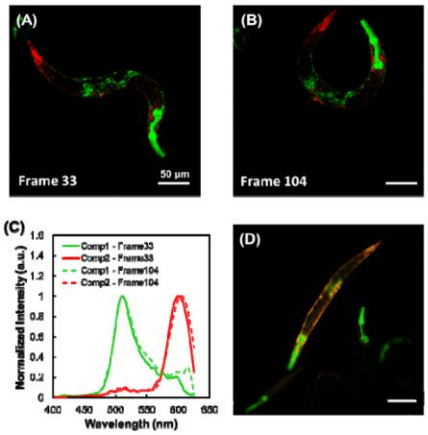

Fig. 6. Two-photon fluorescence image of gene coded *C. elegans* analyzed without knowing the emission spectra of the fluorophores as a priori at (A) frame 33 and (B) frame 104. Pseudo-color based on different components recovered from custom classification algorithm with green for component 1 and red for component 2 (also see Visualization 2). (C) Recovered spectra for component 1 (green) and 2 (red) for both frame 33 (solid lines) and frame 104 (dash lines). Both plotted spectra were averaged over all the spatial positions of the same classified component. (D) Fluorescence image of gene coded *C. elegans* with conventional fluorescence microscope under 460 - 490 nm excitation.

Research Article Vol. 25, No. 26 | 25 Dec 2017 | OPTICS EXPRESS 32253
Optics EXPRESS

4. Conclusion

A spatial-spectral multiplexing hyperspectral two-photon fluorescence microscope was developed with over 2000 effective spectral channels in a 200 nm wavelength window and an imaging acquisition rate up to 17 fps. Iterative demultiplexing enabled classification and full recovery of emission spectra with no prior knowledge of the sample. Good agreement was observed between the recovered spectra and those obtained independently using a commercial fluorimeter. The large number of spectral channels of this system made it possible to distinguish fluorophores with similar emission spectra. The high imaging speed made it possible to study highly dynamic multicomponent systems and live biological samples. This instrument is directly compatible with numerous conventional beam-scanning microscope platforms upon addition of a diffraction grating and a multi-channel detector array.

Funding

National Institutes of Health (NIH) (R01GM-103401, R01GM-103910).

Acknowledgments

The authors would like to acknowledge AlazarTech for use of the prototype 16-channel digital oscilloscope card. The authors would also like to acknowledge PERSEE for loan of the T6U UV-Vis spectrometer for characterization of optics. F.D. gratefully acknowledges support from the Dr. Ching Siang Yeh Fellowship.